












A REVIEW OF VACUUM-ARC MULTILAYER COATINGS WITH HIGH-STRENGTH CHARACTERISTICS AND ADHESIVE PROPERTIES

 O.V. Maksakova^{a,b},  S.V. Lytovchenko^{a*},  V.M. Beresnev^a,  S.A. Klymenko^c,  D.V. Horokh^a,
 B.O. Mazilin^a,  M.Y. Kopeykina^c,  S.An. Klymenko^c,  V.V. Grudnitskii^d,
 O.V. Gluhov^c,  R.S. Galushkov^a

^aV.N. Karazin Kharkiv National University, 4, Svobody Sq., 61000 Kharkiv, Ukraine

^bInstitute of Materials Science, Slovak University of Technology in Bratislava, 25, Jána Bottu Str., 917 24 Trnava, Slovakia

^cBakul Institute for Superhard Materials, National Academy of Sciences of Ukraine, 2, Avtozavodskaya Str, Kyiv, 04074, Ukraine

^dNational Science Center "Kharkov Institute of Physics and Technology", 1, Akademicheskaya St, Kharkiv, 61108, Ukraine

^eKharkiv National University of Radio Electronics, Nauky Ave. 14, Kharkiv, 61166, Ukraine

*Corresponding Author e-mail: s.lytovchenko@karazin.ua

Received August 22, revised October 21, 2024; accepted November 12, 2024

Using the TiSiN/MeN (Me = Cr, Nb, W, Mo, TiZr) coatings system as an example, the analyzed results of multilayer coatings with nanolayers of various functional purposes require a systematic approach to understanding the role of selected materials, growth conditions, microstructure, and required properties. Nanoscale grain boundaries, coherent interlayer boundaries, and changes in columnar morphology at the micro level significantly change the physical and mechanical properties of coatings. For all coatings, an increase in mechanical parameters (hardness, modulus of elasticity) is observed due to the formation of a nanoscale phase (which additionally prevents the movement of dislocations together with nanocomposite TiSiN). In addition, there is a mismatch of crystal lattices between layers. Effectively contributes to strengthening due to variable fields of stresses and strains caused by deformations of elastic coherence. Research has determined optimal conditions for the formation of coatings in a wide range of gas (nitrogen) pressure and shear potential, which also allowed for establishing the factors of structural changes and operational characteristics that will be optimal for their industrial use.

Key words: Cathodic vacuum arc physical vapor deposition; Multilayer coatings; TiSiN; Bias potential; Hardness; Phase state; Annealing

PACS: 68.55.Jk, 68.65.Ac

INTRODUCTION

A complex of structural materials with enhanced physical and mechanical properties is used to improve the reliability and durability of modern technology in operation. However, to increase the performance of products, in particular cutting tools, it is relevant to create and use protective coatings, whose principle is based on a complex of tribological and mechanochemical effects that determine the ability of coatings to maintain their integrity and high wear resistance under the influence of high temperatures and contact loads [1-3]. One of the key trends in developing these coatings is to ensure the nanoscale of both structural elements and individual layers in multilayer compositions [4-8]. The formation of the nanoscale structure of the coating materials is related to the choice of graininess, which is optimal according to the strength criterion, the balance between the Hall-Patch dependence, and the expression that determines the rate of grain boundary creep with decreasing grain size. The efficiency of applying such coatings is attributed to the combination of their high physical and mechanical properties, resistance to oxidation, and dissociation of the chemical compounds included in their composition due to the peculiarities of the structure of nanocomposite film systems. Immersing nanocrystalline grains in the amorphous matrix of the second phase of the material, for example, Si₃N₄ can boost the physical and mechanical properties of TiN coatings, increasing their oxidation resistance and thermal stability [9, 10].

In work [11], it was found that the process of destruction of TiSiN nanocomposite coatings changed from brittle to ductile when the residual compressive stress decreased to the level at which the microcracks were activated. The residual stress of deposited coatings consists of three parts: the epitaxial or structural mismatch between the seed film and the substrate, the internal stress, and the thermal stress during the post-coating cooling process. Annealing is a common method of reducing residual stress as a result of reducing defects, dislocations, and vacancies [12]. However, this treatment also reduces the hardness of coatings obtained by ion bombardment [13].

For this reason, developing TiSiN coatings with a multilayer architecture is considered a more effective method to improve viscosity and wear resistance, reduce residual stress, and maintaining high hardness [4].

First and foremost, the lattice mismatch and the interface between the different layers can cause the lattice to distort to accommodate the applied stress and create an alternating stress field to reduce the stress concentration. Additionally, different stress properties in each coating can reduce overall stress [14].

Cite as: O.V. Maksakova, S.V. Lytovchenko, V.M. Beresnev, S.A. Klymenko, D.V. Horokh, B.O. Mazilin, M.Y. Kopeykina, S.An. Klymenko, V.V. Grudnitskii, O.V. Gluhov, R.S. Galushkov, East Eur. J. Phys. 4, 11 (2024), <https://doi.org/10.26565/2312-4334-2024-4-01>

© O.V. Maksakova, S.V. Lytovchenko, V.M. Beresnev, S.A. Klymenko, D.V. Horokh, B.O. Mazilin, M.Y. Kopeykina, S.An. Klymenko, V.V. Grudnitskii, O.V. Gluhov, R.S. Galushkov, 2024; CC BY 4.0 license

In work [15], the wear behavior and adhesive properties of multilayer MeN/TiSiN (Me = Ti, Cr, Zr, Mo, Nb_xAl_{1-x}) coatings with variable second layers were studied. Multilayer coatings based on TiSiN alternated with TiN, ZrN, NbAlN, CrN, and MoN with a fixed number of layers were synthesized by cathodic arc ion sputtering. Multilayer coatings based on TiSiN exhibit a precise nanocomposite multilayer structure. Columnar grains are not observed because the growth of crystalline nitride grains is blocked by amorphous Si_3N_4 or interfaces. High adhesion (with a critical load of more than 70 N) and a lower coefficient of friction (between 0.3 and 0.58) are achieved for all multilayer coatings.

In work [16], the investigation of multilayer coatings of the TiSiN/CrN system by cathodic arc evaporation with different multilayer periods (Λ) of 8.3 nm, 6.2 nm, and 4.2 nm was reported. It revealed the formation of a typical columnar structure and B1-NaCl crystalline with a maximum hardness of 37 ± 2 GPa and the lowest wear rate of 0.323 GPa for the coating with $\Lambda = 8.3$ nm. This suggests that the mechanical and tribological properties of TiSiN-based coatings can be enhanced through the design of multilayer coatings.

To enhance the oxidation and/or mechanical properties of TiSiN-based coatings, intensive efforts have been made to explore multilayer structures. In work [17], nano-multilayer TiSiN/TiAlN films were reported by a dual cathodic arc plasma evaporation system with a hardness ranging from 32 to 38 GPa. The potentiodynamic polarization measurements showed that for all the multilayered coatings the corrosion potential shifted to higher values, and the corrosion current density decreased, indicating better corrosion resistance than that of single-layer coatings like TiAlN or TiSiN [18-20].

According to this principle, TiSiN-based multilayer coatings have attracted a great deal of interest. The existing literature shows that most scientific researchers focus on the influence of the bilayer period on the microstructure and mechanical properties of TiSiN-based multilayer coatings. However, there are relatively few studies devoted to the investigation of the properties, which is the most important factor for the application.

To summarise data on TiSiN-based multilayers for specific applications, we decided to write this review paper, which concludes the results of newly published experiments on multilayer coatings TiSiN/MeN (Me = Cr, Nb, W, Mo, and TiZr).

MATERIAL AND METHODS

The architectural solution of composite multilayer coatings based on TiSiN is presented in Figure 1.

Multilayer coating systems TiSiN/MeN (Me = Cr, Nb, W, Mo, and TiZr) were synthesized by cathodic vacuum arc physical vapor deposition (CVA-PVD). The scheme of the cathodic-arc deposition machine is depicted in Figure 2.

Two evaporators were used to obtain TiSiN/MeN coatings. The cathodes were sintered from the TiSi target (chemical specification in at. % is $Ti_{94}Si_6$) and Me targets such as Cr, Nb, W, Mo (purity specification is 99.8 %) and sintered TiZr (chemical specification in at. % is $Ti_{75}Zr_{25}$). Nitrogen was supplied by injecting N_2 gas (a purity of 99.6 %) into the deposition chamber.

The coating systems were deposited on stainless steel (grade 12X18H9T or an analogue of SUS321 and 321S51) with dimensions of 20 mm×20 mm×2 mm.

The specific technological parameters during the deposition of multilayer coatings are summarized in Table 1.

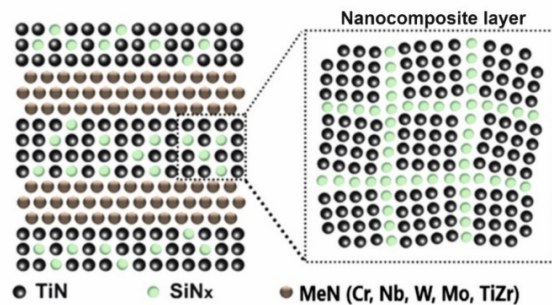


Figure 1. The architecture scheme of composite multilayer coating systems TiSiN/MeN (Me = Cr, Nb, W, Mo, and TiZr).

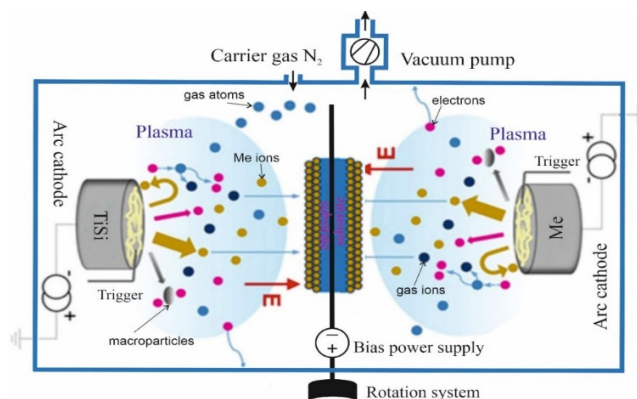


Figure 2. Scheme of the CAE-PVD machine used for the deposition of the multilayer coating systems TiSiN/MeN (Me = Cr, Nb, W, Mo, and TiZr). Adapted from [21].

Table 1. Deposition parameters of multilayer coating systems TiSiN/MeN (Cr, Nb, W, Mo, and TiZr).

Coating	Sample no.	Arc current, A	Negative bias, V	Gas pressure, Pa	Coating thickness, μm	Multilayer period, nm
TiSiN/ CrN	1	110/90	-100	0.08	7-10	6.7-12.5
	2			0.3		
	3			0.06		
	4	110/80	-200	0.08		
	5			0.3		
	6			0.6		
TiSiN/NbN	1	110/80	-110	0.53	5.1	56
	2		-200		4.5	50
	3		-110	0.13	6.8	75
	4		-200		6.3	70
TiSiN/WN	1	100	-200	0.6	4.2	10.5
TiSiN/TiZrN	1	80-85	-200	0.6	3.61	40.1
	2			0.13	3.72	40.9
	3			0,6	3.67	20.4
	4				3.96	85.9
TiSiN/MoN	1	140/100	-100	0.05	9-11	7-8
	2		-200			
	3	140/100	-100	0.13		
	4		-200			
	5	140/100	-100	0.67		
	6		-200			

DISCUSSIONS

Coatings of TiSiN/NbN system

Experimental results for multilayer TiSiN/NbN coatings are shown in Figure 3 and Figure 4 and adopted from [21-23]. The TiSi target was obtained by the vacuum-arc remelting method. The composition of targets was $\text{Ti}_{94}\text{Si}_6$ and $\text{Nb}_{99.8}$. As can be seen, the surface morphology of the coatings has a well-defined cellular structure (Figure 3, left panel). There are many shallow craters with a diameter of 0.3 to 5 μm . Solid inclusions in the form of drops are unevenly distributed over the surface and occupy approximately 15 % of the surface area. The diameter of the droplets varies between 2 to 10 nm.

In the cross-section, the coatings are evenly deposited on the substrate and have a dense structure. A clear periodic arrangement of nanoscale layers in the laminar architecture is observed (Figure 3, right panel). The thickness of the NbN layers is 20 % greater than the thickness of the TiSiN layers. This difference in thickness can be attributed to a lower rate of evaporation of the TiSi cathode, which mainly consists of the refractory intermetallic compound TiSi_2 , compared to pure niobium. Additionally, the smaller thickness and higher density of TiSiN can also be explained by the lower formation energy of TiSiN compared to NbN. The structure of the NbN layers is more difficult to densify by ion bombardment, which is generated by the -110 V and -200 V bias voltages applied to the substrate during coating production. Thus, both phenomena lead to the formation of thinner but denser TiSiN layers. According to elemental analysis data, it was established that the coatings obtained at a higher bias potential of -200 V have a lower concentration of Si ranging between 0.8 to 1.0 at. % than the coatings obtained at a lower bias potential of -110 V.

According to XRD patterns (see Figure 4a), it was established that in the coatings obtained at low values of the bias potential of -110 V (samples nos. 1 and 3), two phases are formed: face-centered cubic (fcc) titanium nitride TiN (space group No. 225) and hexagonal close-packed (hcp) niobium nitride NbN- δ' (space group No. 194). Analysis of the intensity and position of the peaks indicates the presence of a (111) texture in fcc-TiN and a strong (00.2) texture in hcp-NbN- δ' for the coating obtained at a pressure of 0.13 Pa (sample no. 1). An increase in the gas pressure to 0.53 Pa leads to a redistribution of the peak intensity and a shift in their position, which indicates the practically non-textured state of the sample no. 3.

An increase in the negative bias potential leads to the appearance of clear high-intensity peaks in the diffraction patterns, which indicate the formation of a nanocrystalline state in the coatings (see Figure 4b). For the sample obtained at a low pressure of 0.13 Pa (sample no. 2), two phases are formed: fcc-TiN and hcp-bN- δ' . However, with an increase in pressure to 0.53 Pa, structural and phase transformations occur in the coatings, leading to the appearance of the third phase - face-centered cubic (fcc) niobium nitride NbN (space group No. 225) (sample no. 4). Due to the complex structure of the samples, the diffractogram has many diffraction planes for different phases, and some peaks overlap.

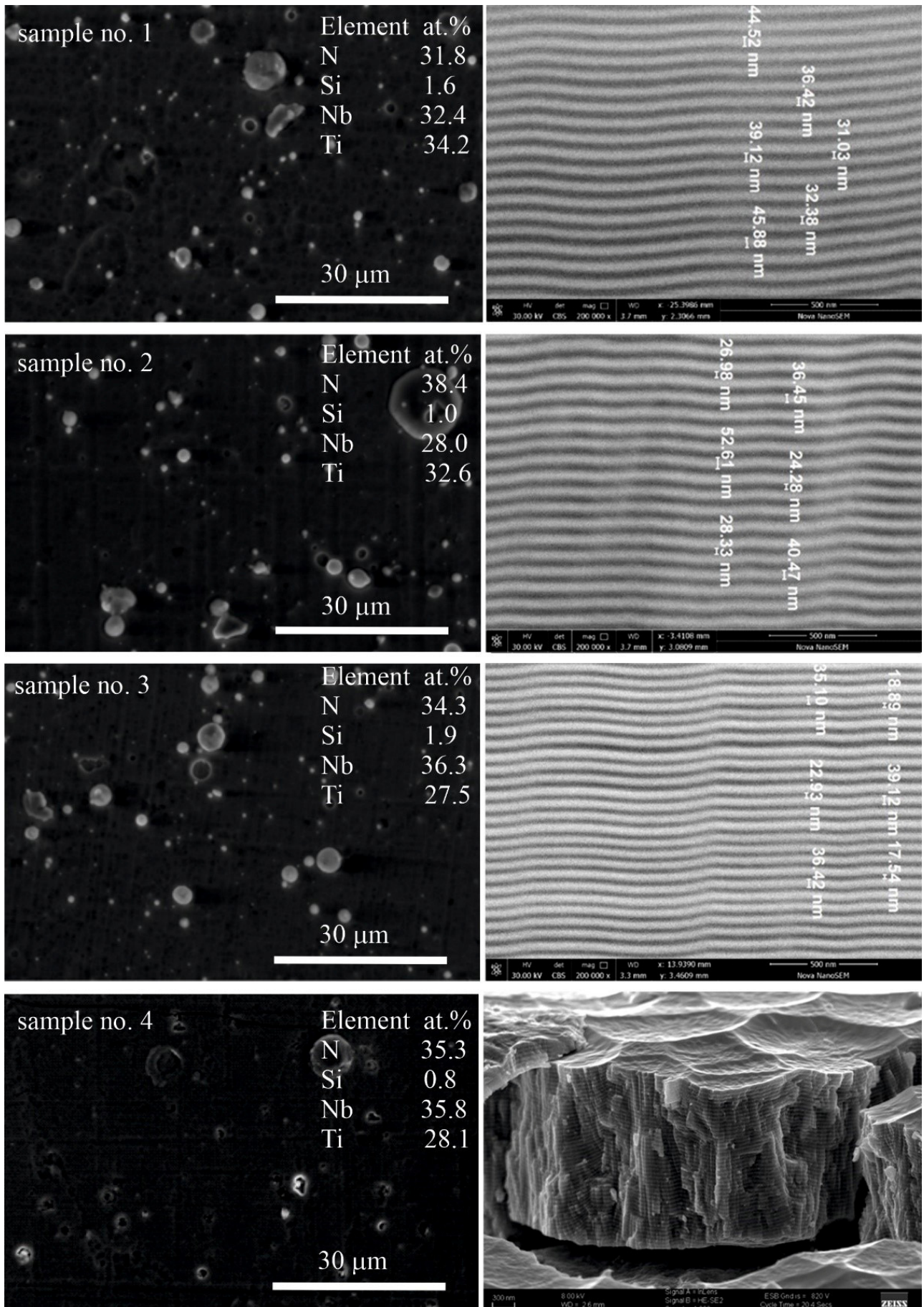


Figure 3. Scanning electron microscopy images of the surface and cross-section of multilayer coatings TiSiN/NbN.

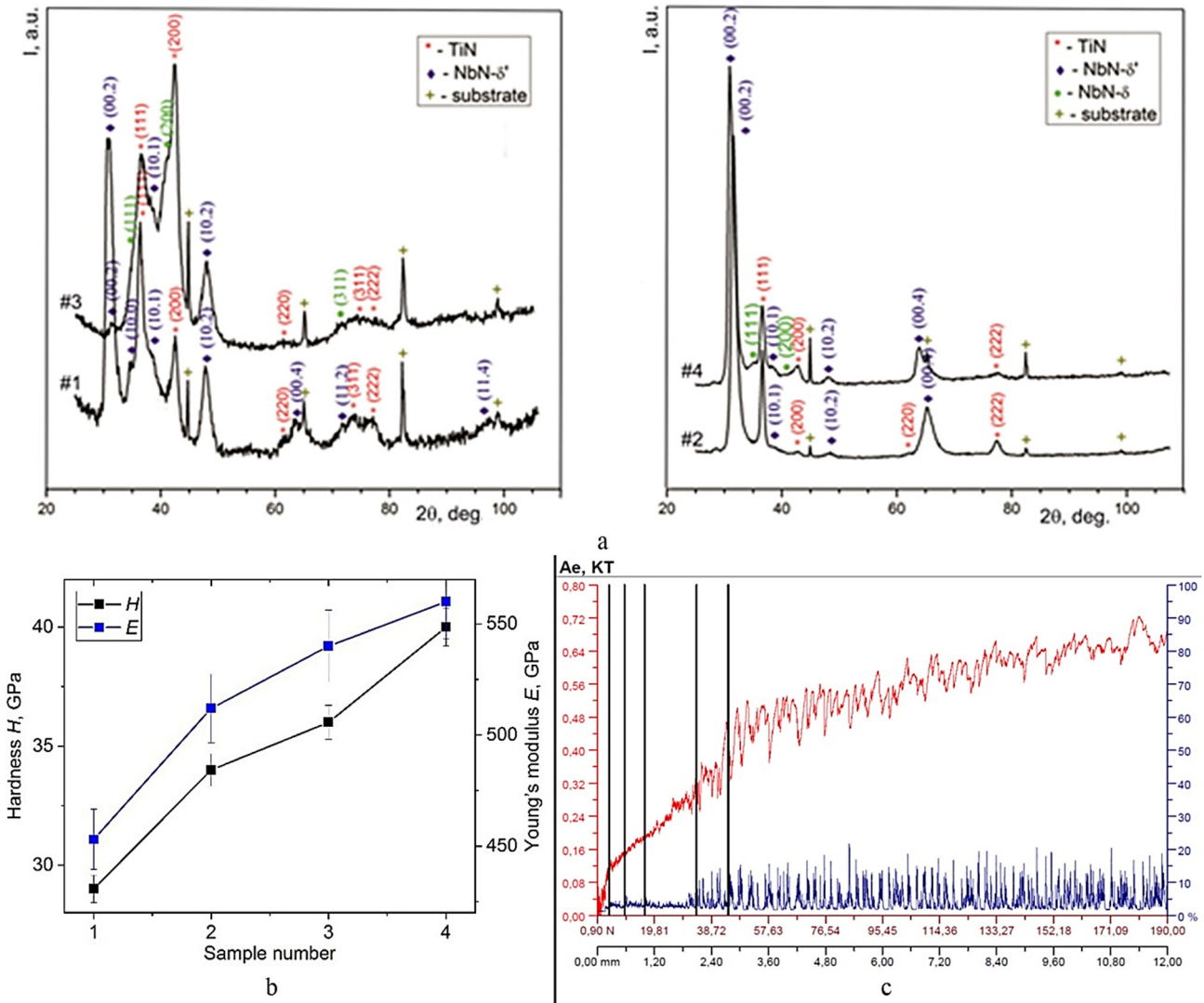


Figure 4. General research results of multilayer coatings TiSiN/NbN: XRD patterns (a), Hardness and Young’s modulus (b), results of sclerometric studies of the sample no. 2 (the red line corresponds to the friction coefficient (COF) and the blue line corresponds to the acoustic emission (AE)) (c).

The average grain size ranges from 8 to 14 nm. The lattice parameter for TiN ranges from 0.4250 to 0.4256 nm and is slightly increased compared to the reference fcc-TiN ($a = 0.4240$ nm according to JCPDS). This indicates the formation of residual compressive stresses in the coatings.

For TiSiN/NbN coatings, an increase in mechanical parameters is observed (see Figure 4b). The hardness grows up to 34.4 GPa, and the modulus of elasticity rises up to 412 GPa. This is due to the formation of a nano-sized NbN phase (which additionally prevents the movement of dislocations together with nanocomposite TiSiN). In addition, the crystal lattice mismatch between the TiSiN and NbN layers effectively contributes to strengthening due to variable stress and strain fields caused by elastic coherence deformations. The multilayer architecture contributes to the reduction of grain sizes and the increase of the volume fraction of atoms located at the interfaces of layers, thereby preventing the propagation of dislocations.

Adhesive strength tests (see Figure 4c) indicate a cohesive failure mechanism of TiSiN/NbN coatings, which is associated with plastic deformation and the formation of fatigue cracks in the material. The maximum load resulting in plastic abrasion of sample no. 2 is greater than 49.76 N, which indicates a high degree of strength of the coating and high adhesive properties of the contact between the coating and the substrate.

Coatings of TiSiN/CrN system

Figure 5 shows experimental results for multilayer TiSiN/CrN coatings adopted from [24, 25]. The vacuum-arc remelting method was applied to sinter the TiSi target. The composition of targets were $Ti_{94}Si_6$ and $Cr_{99.9}$. Since the TiSiN and CrN films have a face-centered cubic structure, in the multilayer architecture, which is depicted in Figure 5a, the TiSiN and CrN nanolayers tend to grow epitaxially, which will reduce the interfacial energy in the coatings. As the thickness of the CrN nanolayer increases, the increase in strain energy due to the different lattice parameters of TiSiN and

CrN disrupts the coherent interface. Thus, the structure of the epitaxial growth between TiSiN and CrN can be disturbed, which leads to a deterioration of crystallinity.

The elemental analysis results established that all TiSiN/CrN coatings have a slightly higher stoichiometric composition, confirmed by the ratio of metal elements to nitrogen (Ti + Si + Cr)/N (see Figure 5a, insert). The coating of sample no.3 obtained at the bias potential of -100 V and nitrogen pressure of 0.6 Pa has the maximum silicon concentration. As the bias potential increases to -200 V, the silicon concentration drops several times. Apparently, this is due to the preferential atomization of light silicon atoms from the surface of the growing coating due to ion bombardment. The higher the shear potential and the lower the gas pressure in the chamber, the stronger this effect.

The analysis of the secondary mass spectrometry is presented in Figure 5b. It confirms the presence of positive ions in the spectra, in particular Ti, Cr, Si (at 28–30 min with low intensity), TiN, CrN, Ti₂, TiCr, Ti₂N, Ti₂N₂ (probably TiSi in the case of the presence of a layer of TiSiN), as well as Ti₃N, Ti₃(N₂)(Si), Ti₃(N₃)(SiN). The spectrum of negative ions revealed the presence of SiN, TiN, and CNI(Cr, Cr₂), which shows a maximum at the beginning of the sputtering and decreases and reaches a plateau after 45–60 min. The intensity of the secondary ion current for TiN and Ti_x bonds is relatively small in the first five minutes of sputtering, then increases sharply, reaches a maximum, and soon (after 45-60 minutes) reaches a plateau.

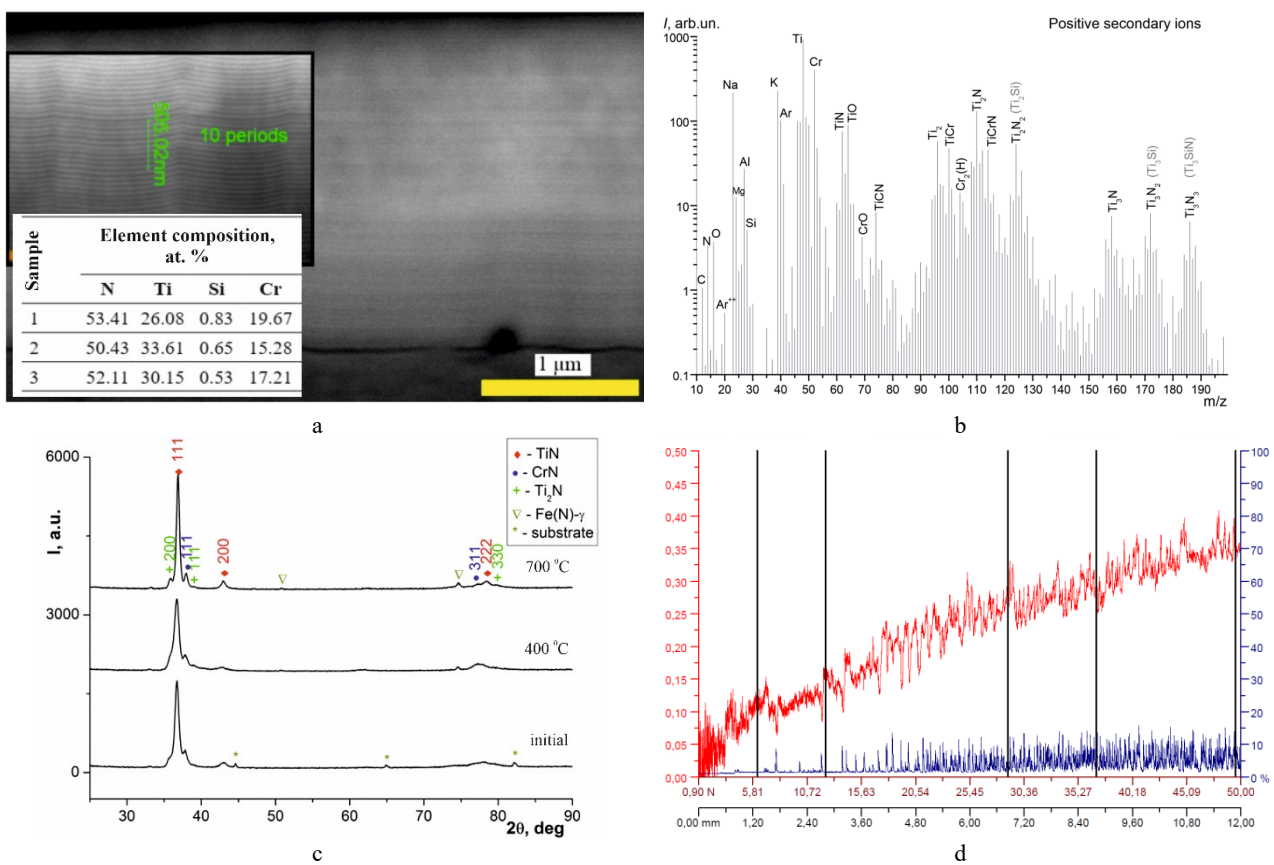


Figure 5. General research results of multilayer coatings TiSiN/CrN: typical SEM image of cross-section with chemical analysis for sample nos. 1-3 (a), spectrum of positive secondary ions for sample no. 3 (b), typical XRD patterns (c), results of sclerometric studies of the sample no. 3 (the red line corresponds to the friction coefficient (COF) and the blue line corresponds to the acoustic emission (AE)) (d)

X-ray patterns of multilayer TiSiN/CrN coatings in the initial state show the formation of three main nitride phases, in particular, face-centered cubic (fcc) TiN (JCPDS 38-1420) and Ti₂N phase (JCPDS 23-1455) with tetragonal (anti-) rutile type structure (space group P42/mnm) for TiSiN layers, and face-centered cubic (fcc) CrN (JCPDS 65-2899) for CrN layers (see Figure 5c). For these coatings, the Ti₂N phase leads to a high level of microdeformations with a value of 7.5×10^{-3} . The main crystalline phase is TiN with a cubic B1 (NaCl-type) structure. Applying a negative bias potential to the substrate during deposition leads to a highly textured state with a predominant orientation along the (111) axis. In addition, it increases the number of defects in the crystal structure and the level of residual compressive stresses.

After annealing the coatings at 400 °C (see Figure 5c), the phase composition TiSiN/CrN of sample no. 1 does not change. Still, crystallization occurs in the CrN layers, as indicated by separating the CrN(111) peak from the highly intensive TiN(111) peak. Increasing the annealing temperature to 700 °C also does not lead to a change in the phase composition of the coatings or the texture. Still, the separation of the CrN(111) peak becomes much more noticeable. At the same time, low-intensity peaks of Ti₂N(200), Ti₂N(111), Ti₂N(330), and CrN(311) appear. Annealing leads to a greater decrease in the lattice parameters of all phases by 2-3 % and a decrease in the level of microdeformations from

7.5×10^{-3} to 7.2×10^{-3} . After annealing at 700 °C (see Fig. 5c), the content of Si in the upper layers of the coatings increased due to intensive diffusion of silicon from the depth of the coating to the surface. At the same time, at 700 °C, a change in the stoichiometry of the coatings accompanies the annealing process. All coatings acquire a pre-stoichiometric composition as the concentration of N decreases from (50.43 ÷ 53.41) to (48.18 ÷ 49.16) at. %.

According to the mechanical tests, all TiSiN/CrN coatings are pretty hard (hardness values varied between 27.8 and 31.1 GPa) in the initial state. Annealing the coatings at 400 °C increases the hardness to (29.1 ÷ 32.8) GPa. A further increase in the annealing temperature to 700 °C slightly reduces the hardness of the coatings to the range of (28.8 ÷ 30.9) GPa. The coating sample no. 3, obtained at a bias potential of -200 V and a working gas pressure of 0.6 Pa, has the best mechanical properties both in the initial and after annealing. The coating hardness and elastic modulus have maximum values of 31.1 GPa and 298 GPa (32.8 GPa and 311 GPa at 400 °C and 30.9 GPa and 301 GPa at 700 °C), respectively. The higher hardness of this sample is due to the higher level of crystallinity of the TiSiN layers in the multilayer structure (according to the Pathscheider model). The H^3/E^2 values of the coatings are also exceptionally high both in the initial state (0.20 ÷ 0.33) and after annealing at 400 °C (0.23 ÷ 0.36) and at 700 °C (0.23 ÷ 0.32), which indicates their reasonably high resistance to mechanical loads without and under the influence of temperature.

The results of the adhesive tests, presented in Figure 5d, show that the coatings wear out under load, but do not peel off. Coating destruction occurs through a cohesive mechanism associated with plastic deformation and the formation of fatigue cracks in the coating material. It was found that the adhesive strength of TiSiN/CrN coatings obtained at a nitrogen pressure of 0.6 Pa and a bias potential of -100 B is higher by 10 % compared to coatings obtained at a bias potential of -200 B. For sample no. 3, which has the best hardness indicators, we identified the highest adhesive strength of 49.54 N.

Coatings of TiSiN/WN system

The results of experimental studies of the structure and properties of multilayer TiSiN/WN coatings before and after annealing are given in [26, 27] and depicted in Figure 6.

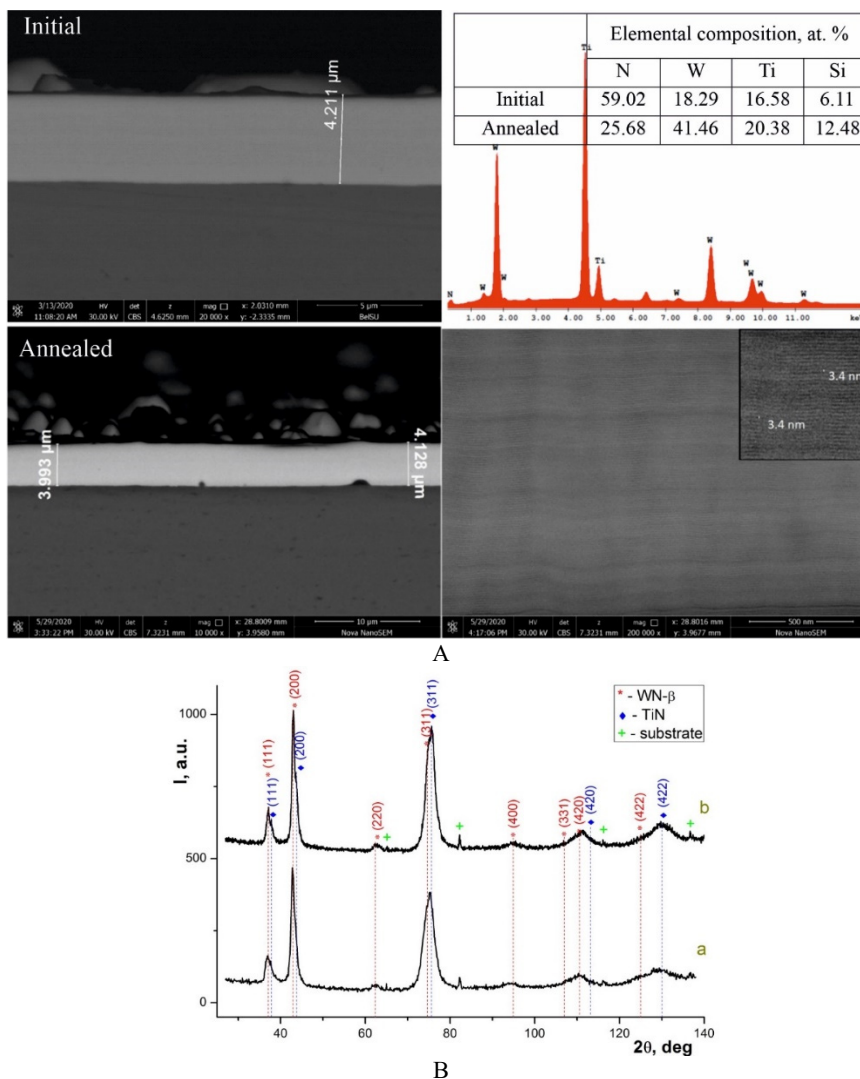


Figure 6. General research results of multilayer coatings TiSiN/WN: SEM images of the cross-sections with chemical analyses before and after annealing (a) XRD patterns before and after annealing (b)

It was established that all coatings have a relatively dense homogeneous structure (see Figure 6a). There are no cracks, pores, or other structural defects at the "substrate-coating" interface. According to the results of the quantitative analysis of the droplet phase, the average size of droplet formations in the coatings is approximately the same. Still, their number in the TiSiN/WN coating is reduced by two times compared to the WN/TiN coating due to the higher melting temperature of the TiSi system. After annealing, the surface of the coating's changes, while the main part, in the direction from the surface to the substrate, remains visually unchanged. Noticeable dimensional changes, in particular, the thickness of coatings decreases by 5 %.

It is seen that the heating intensified the diffusion processes that contributed to the changes in the atomic composition of the components (see Figure 6a). The titanium concentration increases from 16.58 to 20.38 at. % and tungsten concentration rise from 18.29 to 41.46 at. %. This may be due to the additional formation of solid solutions from TiSi and W atoms in the near-boundary region due to the diffusion processes and mixing. The silicon concentration increased approximately two times, from 6.11 to 12.48 at. %.

Experimental data show that nanosize multilayer TiSiN/WN coatings have a two-phase structure: cubic tungsten nitride WN- β and cubic titanium nitride TiN (see Figure 6b). The lattice parameter of WN- β is 0.4232 nm, the grain size is 8.2 nm, and the level of microdeformations is 6.3×10^{-3} . The intensity of the diffraction lines from WN- β and TiN indicates the predominant orientation (200) in the WN layers and (311) in the TiSiN layers. The titanium nitride lattice parameter is 0.4155 nm, the grain size is 9.0 nm, and the level of microdeformations is 1.35×10^{-2} . After annealing at 700 °C, the two-phase structure remained in the WN/TiSiN multilayer coatings. The lattice parameter of WN- β decreases the value of 0.4192 nm, the grain size increases to 12.6 nm, and the level of microdeformations decreases to 3.6×10^{-3} . The lattice parameter of TiN also reduces to 0.4124 nm, the grain size increases to 10.9 nm, and the level of microstrains decreases to 1.16×10^{-2} . The preferential orientation (200) remains unchanged.

It is obvious that annealing intensifies diffusion processes that cause changes in the atomic composition of elements. The Ti concentration increases from 18.29 to 20.08 at. %, and the W concentration rises from 18.29 to 41.46 at. Furthermore, the concentration of N decreases from 59 to 26 at. %, and Si increases almost two times (from 6.11 at. % to 12.48 at. %).

Diffraction lines containing silicon are absent in XRD patterns, which indicates the XRD amorphousness. The only change for the TiSiN/WN coating is that the reflections from WN- β are shifted to higher 2-theta values, which may be due to the annihilation of point defects (interstitial or substituted) often observed in vacuum-arc coatings obtained at high pressure of the working gas [28]. Annihilation should also affect the TiN lattice parameters. However, the diffusion effect of W in TiN can counteract the expected decrease in the lattice parameter, which is observed in this coating. During annealing, the phase state of the coatings did not change in principle, but it led to an increase in grain size and relaxation of internal stresses.

The indicators of the mechanical properties show that the hardness of the annealed coatings increased by 6-7 % (hardness values rise up to 33 GPa, elastic modulus grows up to 422 GPa, fracture deformation, and plastic deformation increases up to 0.078 and 0.202, respectively). In summary, annealing multilayer TiSiN/WN coatings at a moderate temperature partially eliminated structural and technological defects, improving mechanical characteristics.

Coatings of TiSiN/TiZrN system

Increasing the wear resistance of TiSiN-based coatings can be achieved by applying a multicomponent alternating layer, for instance, TiAlN or TiVN [10, 17]. Figure 7 shows the experimental results of the study of multilayer TiSiN/TiZrN coatings adopted from [29-31]. We used the targets made of alloys TiZr (element ratio is 75:25 at. %) and TiSi (elements ratio is 94:6 at. %). The technology used in target production is vacuum-arc remelting. As can be seen in Figure 7a, the surface of the coatings is not smooth, and the droplet fraction on the samples of all samples is present in a rather noticeable amount. In addition to drops, crater-pores are visible on the surface. The cross-sectional images clearly show the layered architecture and the diffusion zone formed at the "coating-substrate" interface. The multilayer combination has good planarity and the boundaries of layers of different compositions are well distinguished. According to chemical analysis, the content of silicon varied between 0.56 to 0.86 at. %, which is significantly lower than its content in the target (5 at. %). The likely reason for these decreases is backscattering.

According to XRD analysis (see Figure 7b), the two-phase structure with fcc crystal structure is formed. The TiZrN and TiN phases have reflections of the (111), (200), and (311) planes. The signal from the (111) planes is the most intense, which is the preferential orientation and can be considered a confirmation of the highest level of crystallinity. An increase in the multilayer period while maintaining the total thickness of the coating is accompanied by a similar decrease in the degree of crystallinity. As the multilayer period increases, splitting the (111) peak into components from the TiZrN and TiN phases becomes more noticeable. A similar pattern is also visible for the (311) peak. The average grain size ranges from 9.2 to 11.6 nm. In coatings deposited under different nitrogen pressures with the same other parameters, the grain size difference was only 0.2 nm, that is, only 2% on average. The architecture and structure of the coating are more significant influences on the grain size. Thus, an increase in the number of bilayers (in other words, a decrease in the multilayer period) from 90 to 180 and 360 leads to a consistent corresponding change in grain sizes along the chain: 11.6 nm (sample no. 4) - ≈ 10 nm (sample no. 1 and sample no. 2) - 9.2 nm (sample no. 3) and to increasing crystallinity (level of texture). During coatings deposition, compressive residual stresses are formed, increasing from -3.5 to -5.3 GPa

with grain size. The calculated dimensions of the lattice parameters differ little (the change range is between 0.4323 and 0.4354 nm); that is, the discrepancy does not exceed 1 %.

According to the data of photoelectron spectroscopy (see Figure 7c), the N 1s spectrum can be separated into two components, of which the main (high-intensity) peak at 395.3 eV can correspond to the energy of Si-N_x type bonds, probably in the Si₃N₄ compound. The low-energy peak at 395.5 eV may correspond to the Ti-N bond energy. The Ti 2p spectrum also splits into two components: the high binding energy at 397.2 eV corresponds to Ti-N type bonds, and the low binding energy at 396.3 eV corresponds to Zr-N bonds.

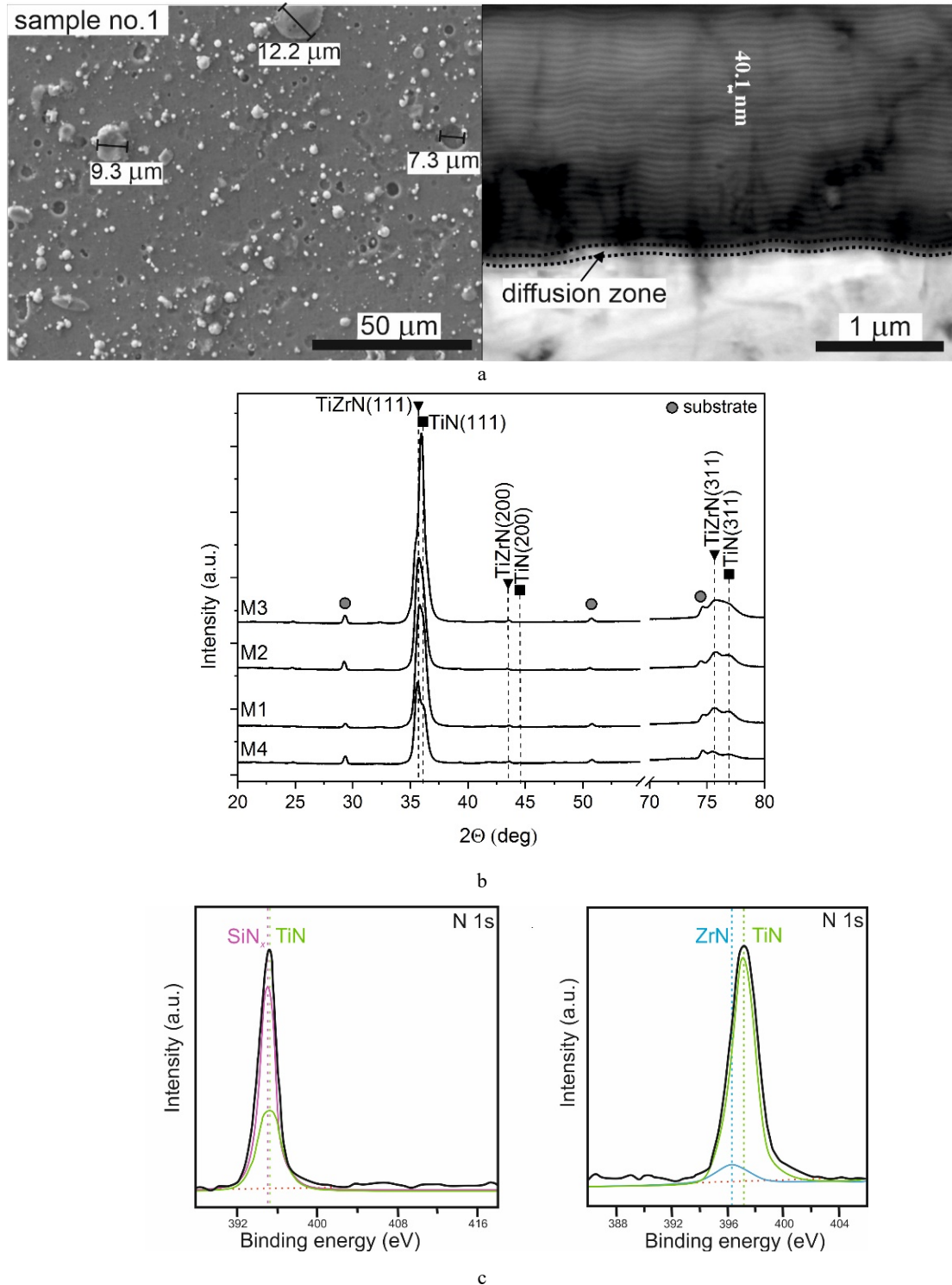


Figure 7. General research results of multilayer coatings TiSiN/TiZrN: typical SEM images of the surface and cross-section (a), XRD patterns (b), photoelectron spectroscopy spectra (c), results of sclerometric studies of the sample nos. 2 та 4 (the red line corresponds to the friction coefficient (COF) and the blue line corresponds to the acoustic emission (AE)) (d, e), SEM image of the scratch on the surface of sample no. 4 at different critical loads $L_{c1} - L_{c5}$ (f).

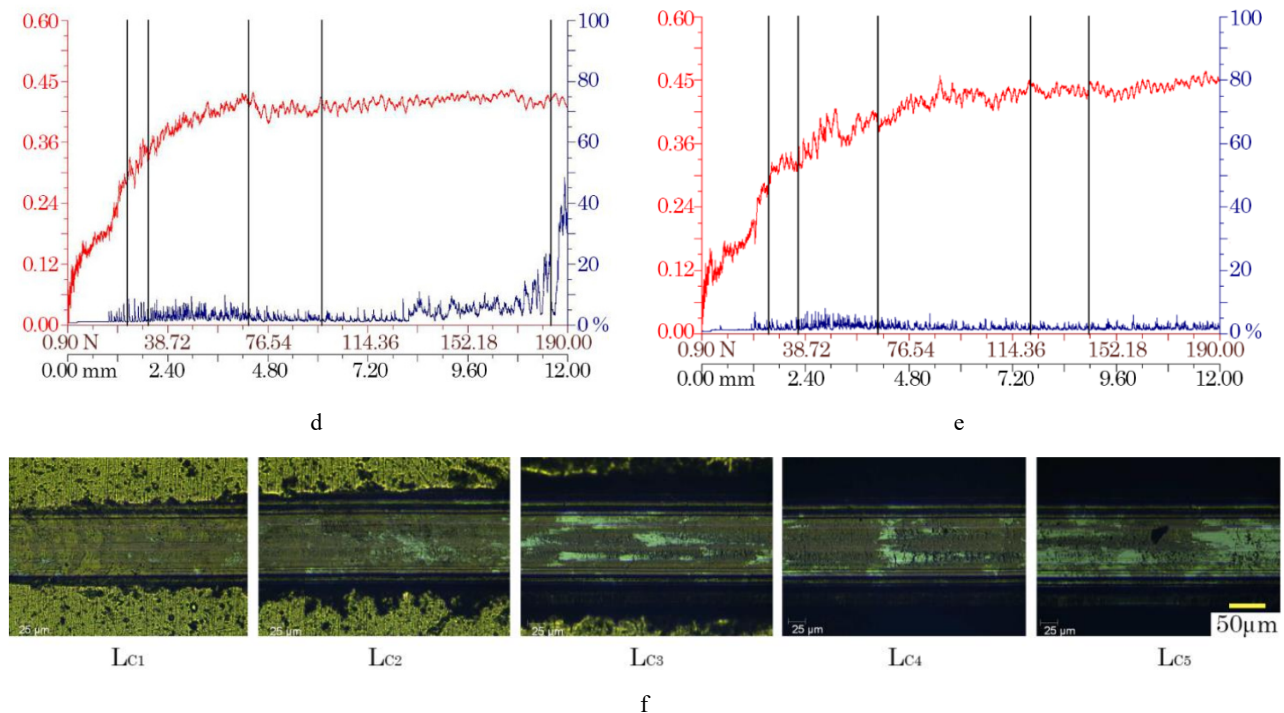


Figure 7. (continued) General research results of multilayer coatings TiSiN/TiZrN: typical SEM images of the surface and cross-section (a), XRD patterns (b), photoelectron spectroscopy spectra (c), results of sclerometric studies of the sample nos. 2 та 4 (the red line corresponds to the friction coefficient (COF) and the blue line corresponds to the acoustic emission (AE)) (d, e), SEM image of the scratch on the surface of sample no. 4 at different critical loads $L_{c1} - L_{c5}$ (f).

Compared to TiSiN or TiZrN films, multilayer TiZrN/TiSiN coatings have increased hardness, ranging from 24.5 GPa to 38.2 GPa. The trend of hardness increases with decreasing bilayer thickness, and the trend of hardness increases with decreasing bilayer thickness is evident. The coating with the thinnest multilayer period of 20 nm has the highest hardness of 38.2 GPa and modulus of elasticity of 430 GPa. Similar changes in friction coefficients and acoustic emission parameters were recorded for coatings obtained at different nitrogen pressures (see Figures 7d and 7e). When the load increases to ~ 55 N, the friction coefficients increase quite quickly and steadily to the level of $\sim 0.5 - 0.52$, after which it decreases slightly to the values of 0.46 - 0.47 and remains practically unchanged after that (not more than 0.48) to a maximum load of 190 N. During the entire period of loading and movement of the indenter on the coating surface, the level of acoustic emission (AE) is relatively low. The first pulses are recorded starting with a load of 15 N; the maximum level of AE is observed at loads of 25-45 N, although it does not exceed 5%. Extreme AE peaks are not recorded, a characteristic feature of wear without brittle fracture. No peeling of the coating was recorded during scratching, indicating cohesive wear associated with plastic deformation and fatigue failure of the coating material. Scratches at different stages of loading indicate a smooth wear characteristic of plastic abrasion without clearly visible cracks (see Fig. 7f). Such wear is observed until the coating is completely worn to the substrate.

According to the wear testing results, multilayer TiSiN/TiZrN coatings wear by an abrasive mechanism. The intensity of wear of sample no. 3 (multilayer period is 20.4 nm) is twice as low as in sample no. 4 (the multilayer period is 85.9 nm). The coefficient of friction during the tests range from 0.79 to 0.82. The improvement of wear resistance of TiZrN/TiSiN nanocomposites is affected by their structural and phase features, in particular, multilayer period, concentration of Si atoms, the level of crystallinity (texture), and stress state.

Coatings of TiSiN/MoN system

Figure 8 shows experimental results for multilayer TiSiN/MoN coatings adopted from [32-35]. The vacuum-arc remelting method was applied to sinter the TiSi target. The compositions of the targets were $Ti_{94}Si_6$ and $Mo_{99.8}$. Microscopic analysis of the cross-section images of the coatings showed a reasonably high uniformity and low defectivity (see Figure 8a) of the obtained coatings by thickness. An increase in the bias potential causes more intense surface sputtering, while the thickness of the coating also decreases. It is shown that in the nitrogen pressure between 0.05 and 0.67 Pa, when the pressure increases, changes occur at the elemental level: The Si content decreases and the N and Mo/Ti ratios increase. At the phase level, changes mainly occur in molybdenum-based layers, where the transition $Mo \rightarrow \gamma-Mo_2N \rightarrow MoN$ occurs with increasing pressure. The highest hardness of 37.5 GPa is achieved in this case by forming TiN/ $\gamma-Mo_2N$ layers with an isostructural crystal lattice. The use of high-temperature annealing (at a temperature of 1023 K) makes it possible to increase the hardness of the coatings obtained at a relatively low nitrogen pressure of 0.09 Pa when the formation of an additional solid Ti_5Si_3 phase is likely due to the low nitrogen content.

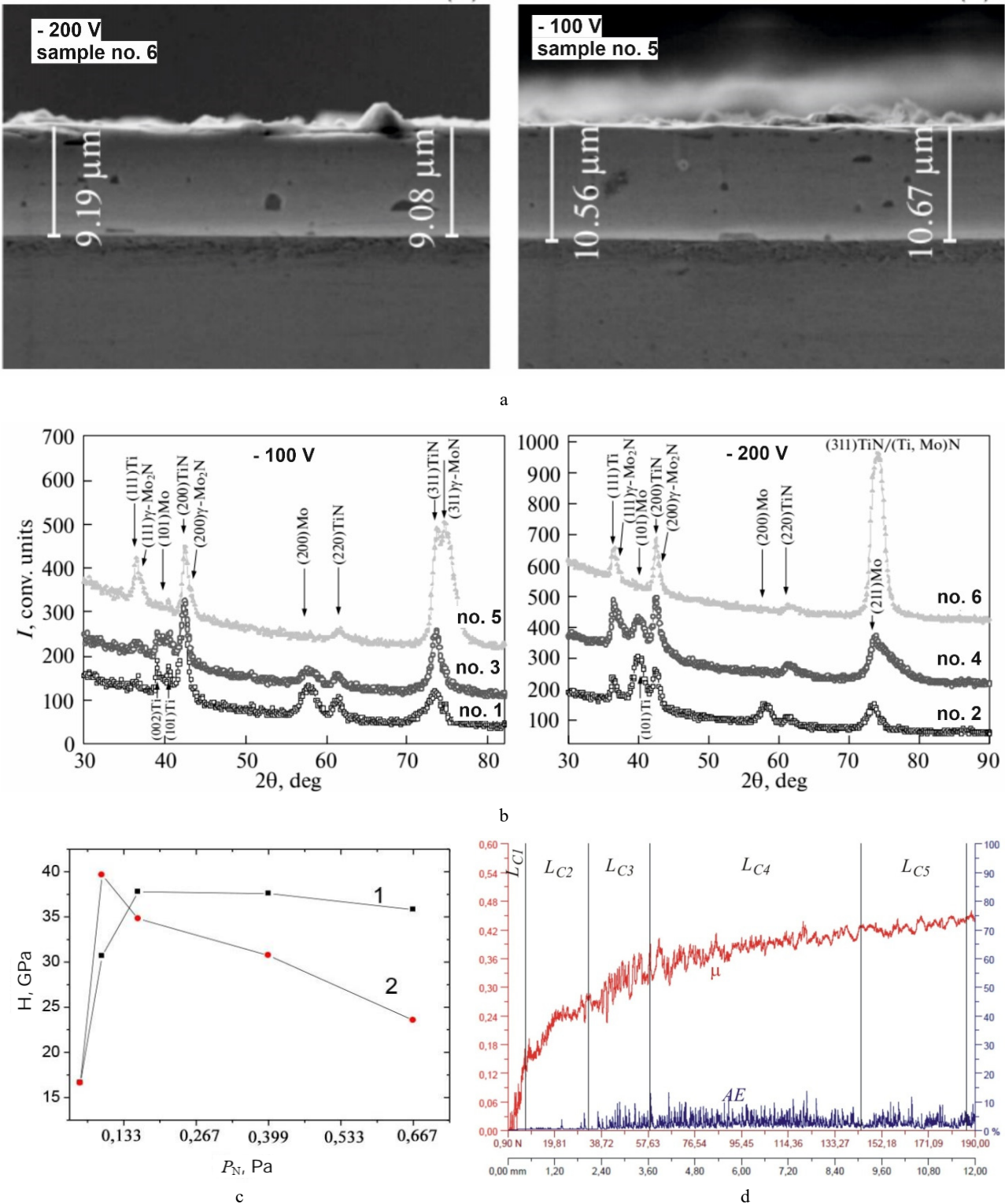


Figure 8. General research results of multilayer coatings TiSiN/MoN: cross-section SEM images (a), XRD patterns (b), dependence of hardness on the nitrogen partial pressure before (curve 1) and after annealing (curve 2) (c), results of sclerometric studies of the sample no. 4 (the red line corresponds to the friction coefficient (COF) and the blue line corresponds to the acoustic emission (AE)) (d).

The results of adhesion strength of multilayer TiSiN/MoN coatings are significantly higher compared to coatings based on TiAlSiN systems, TiZrSiN, and TiHfSiN which were obtained by vacuum-arc deposition [36, 37]. Thus, the destruction of these coatings begins at an average load of 55-65 N, and in multilayer TiSiN/MoN coatings - at a load of 160-180 N. The measurement of hardness shows that the partial pressure of nitrogen, which affects the formation of the phase composition, also has a decisive effect on hardness. The dependence of hardness on pressure reaches maximum values of about 37.5 GPa in the pressure range between 0.16 to 0.4 Pa (see Figure 8c). From the point of view of structural engineering, this state corresponds to the presence of nitride phases TiN and γ-Mo₂N with an isostructural crystalline

lattice of the NaCl type in both layers. Annealing is accompanied by a decrease in the hardness of the coatings obtained in the pressure range of 0.15 to 0.7 Pa, which is associated with the characteristic growth of crystallites in the constituent phases. This is especially noticeable in the coatings obtained at a pressure of 0.7 Pa, when, according to phase analysis, the MoN phase with a hexagonal crystal lattice is formed in molybdenum-based layers. At the same time, annealing of the coatings obtained at a pressure of 0.7 Pa leads to a significant increase in hardness by more than 30 % (up to 40 GPa).

CONCLUSIONS

Based on the obtained research results, the main regularities of the formation of the composition and properties of multilayer coatings were analyzed. This allows for further development of more complex combined multilayer systems with improved physicomechanical and tribological properties, as well as improved biocompatibility.

Studies of multilayer coatings, which consist of a combination of nitride or carbide multielement layers and layers of binary nitrides of refractory or transition metals or layers of pure metals, allow combining within one coating the best properties of multielement and multilayer nitride or carbide coatings. Patterns of structure formation in multilayer and multielement coatings under certain deposition conditions, such as nitrogen atmosphere pressure, bias potential, and substrate temperature, can be used to conduct further fundamental scientific research to elucidate the mechanisms of structure formation of more complex coatings for which these mechanisms are unknown at the moment, or to create approaches to the formation of new types of coatings by varying deposition parameters, architecture, and elemental composition.

The main practical advantages of the proposed vacuum-arc coating deposition method are simplified control over the technological process, reduction of cost and energy consumption, good repeatability of results, and the possibility of relatively easy and fast industrial scaling of deposition technologies.











Modeling the structure and properties of multielement and multilayer coatings based on first-principle molecular dynamics can additionally explain and confirm assumptions about specific features of the formation of the structure and properties of multilayer and multicomponent coatings, which allows us to predict good prospects for its application in further fundamental and applied research more complex from the point of view of architecture coatings.

The results of the study of the properties presented in the review, in particular the structure, hardness, adhesive strength, and the effect of annealing, are the main characteristics that affect the formation of composite nano-sized multilayer coatings as highly efficient materials for multifunctional purpose. This opens new perspectives for the development of new combinations of structural materials and the optimization of their production technologies.

Acknowledgment

This research was carried out with the financial support of the National Research Foundation of Ukraine within the framework of the project "Creation of composites based on cubic boron nitride with protective nanostructured coatings, study of their physical, mechanical and operational properties in the conditions of formation of aircraft products" (project registration number 2022.01/0046) (the winning project of the competition "Science for the Reconstruction of Ukraine in the War and Post-War Periods"). The O.V.M. is honored to be supported by the EU NextGenerationEU through the Recovery and Resilience Plan for Slovakia (project no. 09I03-03-V01-00028).

ORCID

-  Olga V. Maksakova, <https://orcid.org/0000-0002-0646-6704>;
  Serhiy V. Lytovchenko, <https://orcid.org/0000-0002-3292-5468>
 Vyacheslav M. Beresnev, <https://orcid.org/0000-0002-4623-3243>;
  Serhiy A. Klymenko, <https://orcid.org/0000-0003-1464-3771>
 Denis V. Horokh, <https://orcid.org/0000-0002-6222-4574>;
  Bohdan O. Mazilin, <https://orcid.org/0000-0003-1576-0590>
 Maryna Yu. Kopeikina, <https://orcid.org/0000-0002-5956-5503>;
  Klymenko S. An., <https://orcid.org/0000-0002-7913-5519>
 Vadim V. Grudnitskii, <https://orcid.org/0000-0003-3366-6776>;
  Oleg V. Glukhov, <https://orcid.org/0000-0003-2453-5504>
 Ruslan S. Galushkov, <https://orcid.org/0000-0002-9105-9774>

REFERENCES

- [1] A.S. Manokhin, S.A. Klymenko, V.M. Beresnev, S.An. Klymenko, M.Yu. Kopeikina, V.O. Stolbovoy, and S.V. Litovchenko, *Cutting tools made of composites based on cubic boron nitride with a coating*, (Naukova dumka, Publishing House of the National Academy of Sciences of Ukraine, Kyiv, NVP, 2023).
- [2] A.S. Manokhin, S.A. Klimenko, S.An. Klimenko, and V.M. Beresnev, "Promising Types of Coatings for PCBN Tools, *J. Superhard Mater.* **40**, 424–431 (2018). <https://doi.org/10.3103/S1063457618060084>
- [3] A.S. Manokhin, S.A. Klimenko, V.M. Beresnev, et al., "Wear Rate of PcBN Cutting Tools Equipped with Nanolayered Protective Coatings," *J. Superhard Mater.* **42**, 423–431 (2020). <https://doi.org/10.3103/S1063457620060076>
- [4] A. Cavaleiro, *Nanostructured Coatings*, (Springer-Verlag, 2006).
- [5] A.D. Pogrebnjak, O.M. Ivasishin, and V.M. Beresnev, "Arc-evaporated nanoscale multilayer nitride-based coatings for protection against wear, corrosion, and oxidation," *Uspehi Fiziki Metallov*, **17**(1), 1–28 (2016). <http://dx.doi.org/10.15407/ufm.17.01.001>
- [6] O.V. Maksakova, O.D. Pogrebnjak, and V.M. Beresnev, "Features of Investigations of Multilayer Nitride Coatings Based on Cr and Zr," *Usp. Fiz. Met.* **19**(1), 25-48 (2018). <https://doi.org/10.15407/ufm.19.01.025>
- [7] W. Cheng, J. Wang, X. Ma, P. Liu, P.K. Liaw, and W. Li, "A review on microstructures and mechanical properties of protective nano-multilayered films or coatings," *Journal of Materials Research and Technology*, **27**, 2413-2442 (2023). <https://doi.org/10.1016/j.jmrt.2023.10.012>
- [8] J.W. Du, L. Chen, J. Chen, and Y. Du, "Mechanical properties, thermal stability and oxidation resistance of TiN/CrN multilayer coatings," *Vacuum*, **179**, 109468 (2020). <https://doi.org/10.1016/j.vacuum.2020.109468>

- [9] S. Veprek, M.G.J. Veprek-Hejman, P. Kavrankova, and J. Prohazka, "Different approaches to superhard coatings and nanocomposites," *Thin Solid Films*, **476**(1), 1–29 (2005). <https://doi.org/10.1016/j.tsf.2004.10.053>
- [10] Y.Y. Chang, H. Chang, L.J. Jhao, and C.C. Chuang, "Tribological and Mechanical Properties of Multilayered TiVN/TiSiN Coatings Synthesized by Cathodic Arc Evaporation," *Surf. Coat. Technol.* **350**, 1071–1079 (2018). <https://doi.org/10.1016/j.surfcoat.2018.02.040>
- [11] M.S. Ahmed, Z.-F. Zhou, P. Munroe, L.K.Y. Li, and Z. Xie, "Control of the damage resistance of nanocomposite TiSiN coatings on steels: Roles of residual stress," *Thin Solid Films*. **519**(15), 5007-5012 (2011). <https://doi.org/10.1016/j.tsf.2011.01.070>
- [12] J. Bull, "Failure mode maps in the thin film scratch adhesion test," *Tribology International*, **30**(7), 491-498 (1997). [https://doi.org/10.1016/S0301-679X\(97\)00012-1](https://doi.org/10.1016/S0301-679X(97)00012-1)
- [13] I. Aksyonov, A.O. Andreev, V.A. Bilous, V.E. Strelnytskyi, and V.M. Khoroshikh, *Вакуумна дуга: джерела плазми, осадження покриттів, поверхневе модифікація*, [Vacuum arc: plasma sources, deposition of coatings, surface modification], (Naukova Dumka, Kyiv, 2012). (in Ukrainian)
- [14] K Holmberg, *Matthews Coatings tribology: properties, mechanisms, techniques and applications in surface engineering, Tribology and interface engineering series*, vol. 56, (Elsevier, 2009).
- [15] Q. Wan, B. Yang, H.D. Liu, J. Chen, and J. Zhang, "Microstructure and adhesion of MeN/TiSiN (Me = Ti, Cr, Zr, Mo, Nb_xAl_{1-x}) multilayered coatings deposited by cathodic arc ion plating," *Applied Surface Science*, **497**(15), 143602 (2019). <https://doi.org/10.1016/j.apsusc.2019.143602>
- [16] S.-M. Yang, Y.-Y. Chang, D.-Y. Lin, D.-Y. Wang, and W. Wu, "Mechanical and tribological properties of multilayered TiSiN/CrN coatings synthesized by a cathodic arc deposition process," *Surf. Coat. Technol.* **202**(10), 2176–2181 (2008). <https://doi.org/10.1016/j.surfcoat.2007.09.004>
- [17] C.L. Chang, W.C. Chen, P.C. Tsai, W.Y. Ho, and D.Y. Wang, "Characteristics and performance of TiSiN/TiAlN multilayers coating synthesized by cathodic arc plasma evaporation," *Surf. Coatings Technol.* **202**, 987-992 (2007). <https://doi.org/10.1016/j.surfcoat.2007.06.024>
- [18] Y.X. Xu, L. Chen, F. Pei, Y. Du, "Structure and thermal properties of TiAlN/CrN multilayered coatings with various modulation ratios," *Surface and Coatings Technology*. **304**, 512-518 (2016). <https://doi.org/10.1016/j.surfcoat.2016.07.055>
- [19] A.S. Çam, T.O. Ergüder, G. Kaya, and F. Yıldız, "Improvement of structural/tribological properties and milling performances of tungsten carbide cutting tools by bilayer TiAlN/TiSiN and monolayer AlCrSiN ceramic films," *Ceramics International*, **48**(18), 26342-26350 (2022). <https://doi.org/10.1016/j.ceramint.2022.05.318>
- [20] R. Pu, Z. Yu, X. Hao, J. Yan, Z. Han, J. Tan, L. Lu, *et al.*, "Effect of Si content on microstructure, mechanical properties, and cutting performance of TiSiN/AlTiN dual-layer coating," *J. Manuf. Process*, **88**, 134 (2023). <https://doi.org/10.1016/j.jmapro.2023.01.022>
- [21] O. Maksakova, V. Beresnev, S. Lytovchenko, and D. Kaynts, "A Comparative Study of Microstructure and Properties of TiZrN/NbN and TiSiN/NbN Nanolaminate Coatings," in: *Nanocomposite and Nanocrystalline Materials and Coatings. Advanced Structured Materials*, edited by A.D. Pogrebnjak, Y. Bing, and M. Sahul, vol. 214. (Springer, Singapore, 2024). pp. 163-180. https://doi.org/10.1007/978-981-97-2667-7_6
- [22] D.V. Horokh, O.V. Maksakova, S.A. Klimenko, S.V. Lytovchenko, V.M. Beresnev, and O.V. Glukhov, "The Influence of the bias potential answorking gas pressure on the properties of the ion-plasma multilayer coating TiSiN/NbN," *Journal of Superhard Materials*, **44**(6), 413–420 (2022). <https://doi.org/10.3103/S1063457622060041>
- [23] V.M. Beresnev, S.V. Lytovchenko, O.V. Maksakova, A.D. Pogrebnjak, D.V. Horokh, and U.S. Shvets, "Microstructure and High-hardness Effect in TiSiN/NbN Nanomultilayers: Experimental Research," in: *2021 IEEE 11th International Conference Nanomaterials: Applications & Properties (NAP)*, (Odessa, Ukraine, 2021), pp. 1-4, <https://doi.org/10.1109/NAP51885.2021.9568502>
- [24] V.M. Beresnev, O.V. Maksakova, S.V. Lytovchenko, S.A. Klymenko, D.V. Horokh, A.S. Manohin, B.O. Mazilin, *et al.*, "Correlating Deposition Parameters with Structure and Properties of Nanoscale Multilayer (TiSi)N/CrN Coatings," *East European Journal of Physics*, (2), 112-117 (2022). <https://doi.org/10.26565/2312-4334-2022-2-14>
- [25] D.V. Horokh, O.V. Maksakova, V.M. Beresnev, S.V. Lytovchenko, S.A. Klimenko, V.V. Grudnitsky, I.V. Doshchechkina, *et al.*, "Influence of annealing on the physical and mechanical properties of (TiSi)N/CrN multilayer coatings produced by cathodic arc physical vapour deposition," *High Temperature Material Processes*, **27**(4), 1-14 (2023). <https://doi.org/10.1615/HighTempMatProc.2022046618>
- [26] M. Beresnev, S.V. Lytovchenko, O.V. Maksakova, A.D. Pogrebnjak, V.A. Stolbovoy, S.A. Klymenko, and L.G. Khomenko, "Microstructure and high-hardness effect in WN-based coatings modified with TiN and (TiSi)N nanolayers before and after heat treatment: experimental investigation," *High Temperature Material Processes*, **25**(4), 61–72 (2021). <https://doi.org/10.1615/HighTempMatProc.2021041565>
- [27] M. Sahul, B. Bočáková, K. Smyrnova, M. Haršáni, M. Sahul, M. Truchly, M. Kusý, *et al.*, "The Influence Of Multilayer Architecture On The Structure And Mechanical Properties Of WN_x/TiSiN Coatings In Comparison With WN_x and TiSiN Single Layers," *Journal of Physics Conference Series*, **2413**(1), 012013 (2022). <https://doi.org/10.1088/1742-6596/2413/1/012013>
- [28] L. Rogström, N. Ghafoor, J. Schroeder, N. Schell, J. Birch, M. Ahlgren, and M. Odén, "Thermal Stability of Wurtzite Zr_{1-x}Al_xN Coatings Studied by In Situ High-Energy X-Ray Diffraction during Annealing," *J. App. Phys.* **118**, 035309 (2015). <https://doi.org/10.1063/1.4927156>
- [29] V.M. Beresnev, S.V. Lytovchenko, D.V. Horokh, B.O. Mazilin, V.A. Stolbovoy, I.N. Kolodiy, D.A. Kolesnikov, *et al.*, "Tribotechnical properties of (TiZr)N/(TiSi)N multilayer coatings with nanometer thickness," *Journal of Nano- and Electronic Physics*, **11**(5), 05037 (2019). [https://doi.org/10.21272/jnep.11\(5\).05037](https://doi.org/10.21272/jnep.11(5).05037)
- [30] V.M. Beresnev, S.V. Lytovchenko, B.O. Mazilin, D.V. Horokh, V.A. Stolbovoy, D.A. Kolesnikov, I.V. Kolodiy, *et al.*, "Adhesion strength of TiZrN/TiSiN nanocomposite coatings on a steel substrate with transition layer," *Journal of Nano- and Electronic Physics*, **12**(4), 04030 (2020). [https://doi.org/10.21272/jnep.12\(4\).04030](https://doi.org/10.21272/jnep.12(4).04030)
- [31] O.V. Maksakova, S. Zhanyssov, S.V. Plotnikov, P. Konarski, P. Budzynski, A.D. Pogrebnjak, V.M. Beresnev, *et al.*, "Microstructure and tribomechanical properties of multilayer TiZrN/TiSiN composite coatings with nanoscale architecture by cathodic-arc evaporation," *J. Matirial. Sci.* **56**, 5067–5081 (2021). <https://doi.org/10.1007/s10853-020-05606-2>

- [32] V.M. Beresnev, O.V. Sobol, A.A. Meylekhov, A.A. Postelnik, V.Yu. Novikov, Y.S. Kolesnikov, V.A. Stolbovoy, *et al.*, “Effect of Pressure of Nitrogen Atmosphere During the Vacuum Arc Deposition of Multiperiod Coatings (Ti, Si)N/MoN on their Structure and Properties,” *J. Nano- Electron. Phys.* **8**(4), 04023 (2016). [https://doi.org/10.21272/jnep.8\(4\(1\)\).04023](https://doi.org/10.21272/jnep.8(4(1)).04023)
- [33] V.M. Beresnev, U.S. Nyemchenko, P.O. Srebniuk, S.V. Lytovchenko, and O.V. Sobol’, “Study of influence physical and technological parameters of deposition on the structure, physical and mechanical properties of vacuum-arc coatings (Mo + Ti6%Si)N,” in: *Proceedings of 6-th International Conference Nanomaterials: Applications and Properties*, **5**(1), 01FNC08 (2016). <https://doi.org/10.1109/NAP.2016.7757226>
- [34] O.V. Sobol, A.A. Meylekhov, A.A. Postelnik, S.V. Litovchenko, P.A. Srebniuk, U.S. Nyemchenko, and V.M. Beresnev, “Effect of Deposition Process Parameters and High-temperature annealing on the structure and properties of (TiSi)MoN vacuum-arc coatings,” in: *Proceedings of 2017 IEEE 7-th International Conference Nanomaterials: Applications and Properties (NAP-2017)*, (Zatoka, 2017). <https://doi.org/10.1109/NAP.2017.8190211>
- [35] V.M. Beresnev, S.A. Klimenko, O.V. Sobol, S.V. Litovchenko, A.D. Pogrebnyak, P.A. Srebnyuk, D.A. Kolesnikov, *et al.*, “Influence of the High-temperature annealing on the structure and mechanical properties of vacuum-arc coatings from (Mo/Ti, 6 wt.% Si)N,” *J. Superhard Materials*, **39**(3), 172-177 (2017). <https://doi.org/10.3103/S1063457617030042>
- [36] S. Carvalho, L. Rebouta, E. Ribeiro, F. Vaz, C.J. Tavares, E. Alves, N.P. Barradas, *et al.*, “Structural evolution of Ti–Al–Si–N nanocomposite coatings,” *Vacuum*, **83**(10), 1206–1212 (2009). <https://doi.org/10.1016/j.vacuum.2009.03.009>
- [37] V.M. Beresnev, S.A. Klimenko, I.N. Toryanik, A.D. Pogrebnyak, O.V. Sobol, P.V. Turbin, and S.S. Grankin, “Superhard coatings of the (Zr–Ti–Si)N and (Ti–Hf–Si)N systems produced by vacuum–arc deposition from a separated flow,” *J. Superhard Mater.* **36**(1), 29–34 (2014). <https://doi.org/10.3103/S1063457614010055>

ОГЛЯД ВАКУУМНО-ДУГОВИХ БАГАТОШАРОВИХ ПОКРИТТІВ З ВИСОКИМИ ХАРАКТЕРИСТИКАМИ МІЦНОСТІ ТА АДГЕЗІЙНИМИ ВЛАСТИВОСТЯМИ

О.В. Максакова^{a,b}, С.В. Литовченко^a, В.М. Береснев^a, С.А. Клименко^c, Д.В. Горох^a, Б.О. Мазілін^a, М.Ю. Копейкіна^c, С.Ан. Клименко^c, В.В. Грудницький^d, О.В. Глухов^e, Р.С. Галушков^a

^aХарківський національний університет імені В.Н. Каразіна, майдан Свободи 4, 61022, м. Харків, Україна

^bІнститут матеріалознавства, Словацький технологічний університет у Братиславі,
25, вул. Яна Ботту, 917 24, Трнава, Словаччина

^cІнститут надтвердих матеріалів імені В.Н. Бакуля НАН України, вул. Автозаводська, 2, м. Київ, Україна

^dНаціональний науковий центр «Харківський фізико-технічний інститут»,
вул. Академічна, 1, 61108, м. Харків, Україна

^eХарківський національний університет радіоелектроніки, пр. Науки, 14, 61166, м. Харків, Україна

На прикладі системи покриттів TiSiN/MeN (Me = Cr, Nb, W, Mo, TiZr) проаналізовано результати створення багатошарових покриттів з наночастинами різного функціонального призначення, які потребують системного підходу до розуміння ролі обраних матеріалів, умов росту, мікроструктури та необхідних властивостей. Нанорозмірні межі зерен, когерентні міжшарові границі та зміни стовпчастої морфології на мікрорівні суттєво змінюють фізико-механічні властивості покриттів. Для всіх покриттів спостерігається покращення механічних характеристик (твердість, модуль пружності) за рахунок утворення нанорозмірної фази (яка додатково перешкоджає руху дислокацій разом з наноконструктом TiSiN). Крім того, зафіксована невідповідність кристалічних ґраток окремих шарів ефективно сприяє зміцненню внаслідок утворення змінних полів напружень і пружних деформацій. Дослідженнями визначено оптимальні умови формування покриттів у широкому діапазоні тиску реакційного газу (азоту) та потенціалу зміщення, що також дозволило встановити фактори структурних змін та експлуатаційні характеристики, які будуть оптимальними для їх промислового використання.

Ключові слова: вакуумно-дугове осадження; багатошарові покриття; TiSiN; потенціал зміщення; твердість; фазовий стан; відпал

EVOLUTION OF SOLITARY WAVE IN A COLLISIONLESS QUANTIZED MAGNETO-PLASMA WITH ION PRESSURE ANISOTROPY

 **Deepsikha Mahanta**^a,  **Jnanjyoti Sarma**^b

^a*Department of Mathematics, Gauhati University, Guwahati 781014, India*

^b*Department of Mathematics, Radha Govinda Baruah College, Guwahati 781025, India*

*Corresponding Author e-mail: mahanta2017@gmail.com

Received September 2, 2024; revised October 4, 2024; in final form October 13, 2024; accepted October 19, 2024

This paper presents a comprehensive study in a collisionless plasma composed of charged state of heavy positive ion and light positive as well as negative ion. By deriving the Korteweg-de Vries (KdV) equation and by using its standard solution we analyze the characteristics of the solitary profile under varying parameters. We found that the solution gives both rarefactive and compressive soliton. The compressive structures are formed for the slow mode, while rarefactive solitary structures are formed for the fast mode. Furthermore, with the application of planar dynamical systems bifurcation theory, the phase portraits have been analyzed. This dynamical system analysis allowed us to extract important information on the stability of these structures as represented by the KdV equation.

Keywords: *KdV Equation; Solitary Wave; Quantum Plasma; Dynamical System; Reductive perturbation method; Pressure Anisotropy*

PACS: 02.30.Jr, 03.75.Lm, 52.30-q, 45.30.+s, 52.27Lw

1. INTRODUCTION

Two key properties of plasma are nonlinearity and dispersion; nonlinearity causes the wave to steepen, while dispersion aims to make the wave broader. A wave that propagates in the plasma without losing its identity even after interacting with other waves is referred to as a solitary wave when the nonlinearity and dispersion are balanced. A confined nonlinear wave with a steady-state shape is a soliton [1]. Washimi and Taniuti made the first theoretical prediction of the presence of ion-acoustic solitary waves of modest but finite amplitudes in plasma in 1966 [2]. The fundamental characteristics of the ion-acoustic wave would be considerably altered in the linear [3–5] and nonlinear regimes [6, 7] in the presence of a second ion species in a plasma. They discovered that two ion acoustic modes, known as the fast and slow ion modes, are supported by their model. These two ion wave modes are confirmed to exist by the experimental studies [4, 5].

The physics of positive and negative-ion quantum plasmas, and in particular multi-ion plasmas, have attracted a lot of attention lately because of their presence in plasma environments ranging from laboratory to astrophysical. [8–11]. The constituents of the degenerate quantum plasma includes electrons, heavy ions with positive charges, and light ions [12]. It is commonly known that negative ions exist in the Halley’s comet [13] and the Earth’s ionosphere [14]. Positive-negative ion plasmas have also been discovered to exist in a variety of settings, including neutral beam sources [15], low-temperature laboratory studies [16], reactors for plasma processing [17], etc. Numerous authors [11, 18–21] used positively charged heavy and light ions in quantum plasmas to study nonlinear waves.

In the presence of elevated magnetic fields, the plasma ion pressure exhibits anisotropic behavior, and the plasma behaves differently in parallel and perpendicular directions relative to the external magnetic field [22]. So, to consider the effect of ionic pressure anisotropy pressure i.e., the parallel ion pressure (P_{\parallel}) and perpendicular ion pressure (P_{\perp}) become very important. Numerous studies have been reported on the impact of pressure anisotropy on the propagation of solitary and shock waves in different plasma regimes [23, 24]. For example, Almas et al. [25] investigated the properties of ion-acoustic solitary waves composed of anisotropic pressure of electron-positron-ion(e-p-i) plasma and found that the characteristics of such waves are more sensitive to parallel ion pressure than perpendicular ion pressure. Khalid et al. [26] also studied the propagation of ion-acoustic electrostatic waves in a magnetized electron-ion plasma with pressure anisotropy. Mahmood et al. [27] studied the properties of non-linear electrostatic structure in anisotropic pressure plasma and found that only the width of the soliton depends on the perpendicular pressure (P_{\perp}), however, an increase in the parallel pressure (P_{\parallel}) decreases both the amplitude as well as the width of the soliton. Manesh et al. [28] studied the properties of solitary waves in an anisotropic plasma with lighter and heavier ions and found that the light ion’s pressure anisotropy determines the polarity of solitary waves, and it is rarefactive for anisotropic lighter ion whereas compressive for the isotropic lighter ion. Khan et al. [29] studied the properties of soliton and cnoidal wave in an anisotropic superthermal electron-positron-ion plasma and found that the wavelength of the cnoidal wave structure is reduced on increasing the parallel and perpendicular anisotropy of ion. Khalid and Rahman [30] studied the ion pressure anisotropy of the ion acoustic non-linear periodic waves in a magnetized plasma. They reported that the increase of parallel pressure of ions

decreases the amplitude and width of the ion-acoustic periodic waves and the ion-acoustic waves behave differently than ion-acoustic periodic (cnoidal) waves in anisotropic plasmas.

Apart from classical plasmas, the effect of pressure anisotropy has been widely investigated in dense quantum magnetized plasmas. For example, Bordbar and Karami [31] studied the structural properties of an anisotropic dense neutron star and analyzed the compactness, redshift, etc. of such a dense matter as a function strong magnetic field of the order of 10^{17} Gauss which creates the anisotropy. Patidar and Sharma [32] explored the magneto hydrodynamic (MHD) wave modes in anisotropic relativistic degenerate plasma and found fast and slow wave modes propagating under the combined influence of various forces such as pressure anisotropy, exchange potential, Bohm force, and magnetic field. Irfan et al. [33] observed a strong modification of amplitude and width of weakly nonlinear ion-acoustic waves considering the pressure anisotropy of positive ions and electron trapping effects in a dense quantum magneto-plasma. Moreover, in the non-relativistic and ultra-relativistic regimes, the anisotropic ion pressure also affects the stability of solitary waves.

Phase plane analysis is a useful graphical method for analyzing second-order systems with respect to their initial condition, and it is a useful tool for investigating the qualitative behavior of dynamical systems. Geometrically, a curve or point represents the trajectory of a dynamical system for a particular initial state in a phase plane. Furthermore, we may learn more about the system's stability and the presence of solutions using this technique [34]. The significance of phase plane analysis in understanding the qualitative solutions of plasma systems is commonly acknowledged and used by researchers [35–38]. Recently, in various plasma systems, researchers have examined the bifurcation features of small-amplitude nonlinear waves within the framework of equations such as the Burgers equation [39], ZK equation [40], etc. [41, 42]

The objective of the present paper is to study the solitary wave propagation in collisionless quantum magneto-plasma considering the ionic pressure anisotropy. The Korteweg-de Vries (KdV) equation is derived using the reductive perturbation technique(RPT) to study the solitary wave nature in such plasma. These plasmas are believed to exist in white dwarfs and neutron stars. The results obtained here may be useful for laboratory as well as space astrophysical plasma environments wherein such plasma environments are prevalent.

2. THEORETICAL FORMULATION

We consider a collisionless plasma composed of charged state of heavy positive ion and light positive as well as negative ion. The normalized set of governing equations is given by [43]:

$$\frac{\partial N_{ln,lp}}{\partial T} + \frac{\partial(N_{ln,lp}V_{ln,lp_x})}{\partial x} + \frac{\partial(N_{ln,lp}V_{ln,lp_y})}{\partial y} + \frac{\partial(N_{ln,lp}V_{ln,lp_z})}{\partial z} = 0 \quad (1)$$

$$\frac{\partial V_{ln_x}}{\partial T} + \left(V_{ln_x} \frac{\partial}{\partial x} + V_{ln_y} \frac{\partial}{\partial y} + V_{ln_z} \frac{\partial}{\partial z} \right) V_{ln_x} = \vartheta \frac{\partial \Phi}{\partial x} - P_{ln\parallel} N_{ln} \frac{\partial N_{ln}}{\partial x} \quad (2)$$

$$\frac{\partial V_{ln_y}}{\partial T} + \left(V_{ln_x} \frac{\partial}{\partial x} + V_{ln_y} \frac{\partial}{\partial y} + V_{ln_z} \frac{\partial}{\partial z} \right) V_{ln_y} = \vartheta \frac{\partial \Phi}{\partial y} + V_{ln_z} \Omega_{ln} - P_{ln\perp} \frac{1}{N_{ln}} \frac{\partial N_{ln}}{\partial y} \quad (3)$$

$$\frac{\partial V_{ln_z}}{\partial T} + \left(V_{ln_x} \frac{\partial}{\partial x} + V_{ln_y} \frac{\partial}{\partial y} + V_{ln_z} \frac{\partial}{\partial z} \right) V_{ln_z} = \vartheta \frac{\partial \Phi}{\partial z} + V_{ln_y} \Omega_{ln} - P_{ln\perp} \frac{1}{N_{ln}} \frac{\partial N_{ln}}{\partial z} \quad (4)$$

$$\frac{\partial V_{lp_x}}{\partial T} + \left(V_{lp_x} \frac{\partial}{\partial x} + V_{lp_y} \frac{\partial}{\partial y} + V_{lp_z} \frac{\partial}{\partial z} \right) V_{lp_x} = -\frac{\partial \Phi}{\partial x} - P_{lp\parallel} N_{lp} \frac{\partial N_{lp}}{\partial x} \quad (5)$$

$$\frac{\partial V_{lp_y}}{\partial T} + \left(V_{lp_x} \frac{\partial}{\partial x} + V_{lp_y} \frac{\partial}{\partial y} + V_{lp_z} \frac{\partial}{\partial z} \right) V_{lp_y} = -\frac{\partial \Phi}{\partial y} + V_{lp_z} \Omega_{lp} - P_{lp\perp} \frac{1}{N_{lp}} \frac{\partial N_{lp}}{\partial y} \quad (6)$$

$$\frac{\partial V_{lp_z}}{\partial T} + \left(V_{lp_x} \frac{\partial}{\partial x} + V_{lp_y} \frac{\partial}{\partial y} + V_{lp_z} \frac{\partial}{\partial z} \right) V_{lp_z} = -\frac{\partial \Phi}{\partial z} + V_{lp_y} \Omega_{lp} - P_{lp\perp} \frac{1}{N_{lp}} \frac{\partial N_{lp}}{\partial z} \quad (7)$$

$$\frac{\partial^2 \phi}{\partial x^2} + \frac{\partial^2 \phi}{\partial y^2} + \frac{\partial^2 \phi}{\partial z^2} = N_e [1 + Z_{hp} \mu_{hp} + \alpha_p - \mu_{ln}] + N_{ln} \mu_{ln} - Z_{hp} \mu_{hp} - N_{lp} - N_p [\alpha_e + \mu_{ln} - 1 - Z_{hp} \mu_{hp}] \quad (8)$$

Here $\alpha_p = \alpha_e + \mu_{ln} - 1 - Z_{hp} \mu_{hp}$, $\mu_{hp} = \frac{n_{h10}}{Z_{lp} n_{lp0}}$, $\alpha_e = 1 + Z_{hp} \mu_{hp} + \alpha_p - \mu_{ln}$, $\mu_{ln} = \frac{Z_{ln}}{Z_{lp} n_{lp0}}$, $\Omega_{lp,ln} = \omega_{clp,ln} / \omega_{ph}$, $\vartheta = \frac{m_{lp} Z_{ln}}{Z_{lp} m_{ln}}$, $\ln \Lambda$ is the logarithm of Coulomb parameter, $A_{ln(lp)}$ is the atomic weight of heavy positive ion, Z_{hp} is the charged state of heavy positive ions, $Z_{lp(ln)}$ is the charged state of light positive (negative) ions, $N_{lp(ln)}$ is the normalized plasma light positive (negative) ion density, ϕ is the normalized electrostatic potential. $P_{lp(ln)\parallel}$ and $P_{lp(ln)\perp}$ are the parallel and perpendicular pressure of light positive (negative) ion. The pressure equations for the anisotropic and adiabatic system are given by Chew–Goldberger–Law popularly known as (CGL) or double adiabatic theory [44–46], according to which $\frac{d}{dt} (P_{i\parallel} B^2 / n_i^3) = 0$ and $\frac{d}{dt} (P_{i\perp} / n_i B) = 0$. In the case of electrostatic waves in a magnetized plasma, the ambient magnetic

field $B = B_0$ is constant with time, i.e. $\frac{d}{dt}(B) = 0$ where B_0 is the magnetic field at equilibrium. Moreover, the normalized parallel and perpendicular ion pressures obtained from the CGL theory are given as $P_{i\parallel} = 3P_{i\parallel 0}/n_{i0}\epsilon_{Fe}$ and $P_{i\perp} = P_{i\perp 0}/n_{i0}\epsilon_{Fe}$ where $P_{i\parallel 0} = n_{i0}T_{i\parallel}$ and $P_{i\perp 0} = n_{i0}T_{i\perp}$ are the equilibrium values of parallel and perpendicular pressure functions respectively, and n_{i0} is the unperturbed ion density. [22, 45, 47] The variations in the ambient magnetic field alter the ionic temperatures in parallel and perpendicular directions to the magnetic field, i.e., $T_{i\parallel} \propto B_0$ and $T_{i\perp} \propto \left(\frac{n_{i0}}{B_0}\right)^2$ respectively [47, 48].

The other plasma parameters are normalized as follows:

$\Phi = \frac{\epsilon_{Fe}}{e}$, $t = T\omega_p^{-1}$, $x = X \times \lambda_{Fe}$, $N_j = \frac{n_j}{n_{j0}}$, $\lambda_{Fe} = \frac{C_s}{\omega_s}$, $\epsilon_{Fe} = \left(\frac{\hbar}{2m_e}\right) \left(\frac{3\pi^2}{n_{e0}}\right)^{\frac{2}{3}}$ Where, λ_{Fe} is the Thomas-Fermi length, C_s is the Fermi ion sound velocity, ω_{ph} is the plasma frequency, $m_{lp(ln)}$ is the mass of light negative (light positive) ions

3. DERIVATION OF KDV EQUATION

To derive the evolution equation we employed the reductive perturbation technique. The stretched coordinates [22] used here are given by:

$$\xi = \epsilon^{1/2} (I_x x + I_y y + I_z z - MT), \tau = \epsilon^{3/2} T, \tag{9}$$

$$\eta_{ln(lp)\parallel} = \epsilon^{1/2} \eta_{ln(lp)\parallel 0}, \eta_{ln(lp)\perp} = \epsilon^{1/2} \eta_{ln(lp)\perp 0}$$

Where M is the phase velocity (Mach number) and ϵ is a small nonzero constant measuring the strength of dispersion. In terms of the expansion parameter ϵ , the physical variables in equations are expanded in a power series as

$$\left. \begin{aligned} N_j &= 1 + \epsilon N_j^{(1)} + \epsilon^2 N_j^{(2)} + \epsilon^3 N_j^{(3)} + \dots \\ V_{ix} &= \epsilon V_{ix}^{(1)} + \epsilon^2 V_{ix}^{(2)} + \epsilon^3 V_{ix}^{(3)} + \dots \\ V_{jy,z} &= \epsilon^{\frac{3}{2}} V_{jy,z}^{(1)} + \epsilon^2 V_{jy,z}^{(2)} + \epsilon^{\frac{5}{2}} V_{jy,z}^{(3)} + \dots \\ \phi &= \epsilon \phi^{(1)} + \epsilon^2 \phi^{(2)} + \epsilon^3 \phi^{(3)} + \dots \end{aligned} \right\} \tag{10}$$

Substituting the above stretched coordinates from Eq.(9) and the respective expansions from Eq. (10) in the Eqs.(1)-(8), and then collecting the terms appearing in the lowest order of ϵ gives the following relations which gives the phase velocity as

$$M = \pm \sqrt{\frac{b \pm \sqrt{b^2 - 4ac}}{2a}} \tag{11}$$

$$a = (\mu_e \alpha_1 - \mu_p \Upsilon_1)$$

Where $b = I_x^2 (\mu_e \alpha_1 (P_{ln\parallel} + P_{lp\parallel}) - (1 - \vartheta \mu_{ln}) + \mu_p \Upsilon_1 (P_{ln\parallel} + P_{lp\parallel}))$

$$c = I_x^4 (\mu_e \alpha_1 P_{ln\parallel} P_{lp\parallel} + P_{ln\parallel} - \vartheta \mu_{ln} P_{lp\parallel} - \mu_p \Upsilon_1 P_{ln\parallel} P_{lp\parallel})$$

The second-order perturbation terms were also obtained by equating the coefficient of the next higher order of ϵ . Then using standard procedure we obtain the KdV equation as

$$\frac{\partial \phi^{(1)}}{\partial \tau} + A \phi^{(1)} \frac{\partial \phi^{(1)}}{\partial \xi} + B \frac{\partial^3 \phi^{(1)}}{\partial \xi^3} = 0 \tag{12}$$

Where

$$A = \frac{q}{p}, \quad B = \frac{r}{p}$$

$$p = \left(\frac{\mu_{ln} 2 \vartheta M I_x^2}{(M^2 - P_{ln\parallel} I_x^2)^2} + \frac{2 M I_x^2}{(M^2 - P_{lp\parallel} I_x^2)^2} \right)$$

$$q = \left(2 \mu_p \Upsilon_2 - 2 \mu_e \alpha_2 - \frac{\mu_{ln} \vartheta^2 M^2 I_x^2 \left(3 I_x^2 + P_{ln\parallel} \frac{I_x^4}{M^2} \right)}{(M^2 - P_{ln\parallel} I_x^2)^3} + \frac{M^2 I_x^2 \left(3 I_x^2 + P_{lp\parallel} \frac{I_x^4}{M^2} \right)}{(M^2 - P_{lp\parallel} I_x^2)^3} \right)$$

$$r = \left(1 - \left(I_x^2 P_{ln\perp} + 1 \right) \frac{(1 - I_x^2) \mu_{ln} \vartheta M^2}{(M^2 - P_{ln\parallel} I_x^2)^2 \Omega_{ln}^2} + \left(I_x^2 P_{lp\perp} + 1 \right) \frac{(1 - I_x^2) M^2}{(M^2 - P_{lp\parallel} I_x^2)^2 \Omega_{ln}^2} \right)$$

To obtain the solution of Eq. (12), the authors consider the new variable $\chi = \xi - U\tau$ where χ is the transformed coordinate with respect to a frame moving with velocity U. By taking $\phi^{(1)} = \phi$, Eq.(12) becomes

$$-\frac{U}{A} \frac{d\phi}{d\chi} + \phi \frac{d\phi}{d\chi} + D \frac{d^3 \phi}{d\chi^3} = 0 \tag{13}$$

Where $D = \frac{B}{A}$

Now, employing the method used in [49] results the solution of equation(13) as

$$\phi = \phi_m \operatorname{sech}^2 \left(\frac{X}{W} \right) \tag{14}$$

Where $\phi_m = \frac{3U}{A}$, $W = 2\sqrt{\frac{B}{U}}$ are the amplitude and width of solitary wave respectively.

4. RESULTS AND DISCUSSION

The authors examine the properties and nature and solitary wave propagation under various physical scenarios through the analysis of the exact solution provided by Eq. (14). The data range employed in the current paper is widely established across diverse plasma environments. Specifically, the authors consider plasma density on the order of $10^{26} - 10^{30}$ and a magnetic field on the order of $10^{10} - 10^{12}$ with $Te \sim 1$ keV. This set of parameters corresponds to well-known plasma environments found in various astrophysical contexts.

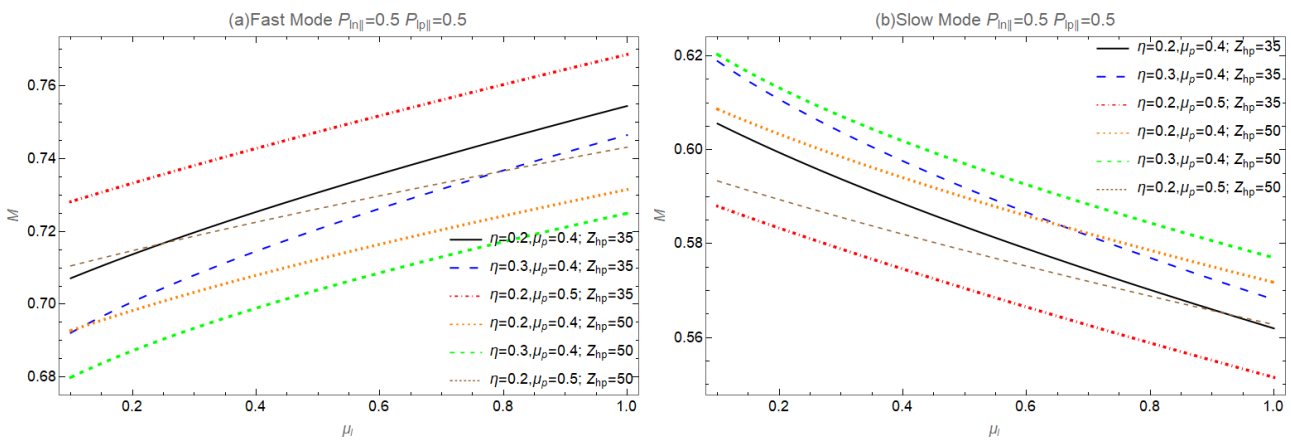


Figure 1. Variations in mach number for different combination of magnetic quantization, positron density and heavy positive ion

The normalized phase velocity, also known as the Mach number, is shown in Figure 1(a) for different combinations of the heavy positive ion, positron density, and magnetic quantization parameter for the fast mode. Figure shows that the velocity is in the subsonic region and that it rises as the density of lighter positive ions increases. The slow mode is plotted for the same set of parameters in Fig. 1(b). While in slow mode, the velocity is subsonic, but it decreases as the density of lighter positive ions increases. By comparing Figs. 1(a) and 1(b), we can observe that the velocity is maximum in the fast mode and lowest in the slow mode for $\eta = 0.2, \mu_p = 0.5, Z_{hp} = 35$, and $\eta = 0.3, \mu_p = 0.4, Z_{hp} = 50$, respectively.

Depending on the sign of the nonlinearity coefficient A, the soliton solution given by Eq. (29) may yield either a positive (compressive) or a negative (rarefactive) profile. Fig2 displays solitary profiles for variation of Z_{hp} for fast mode. It is clear that when Z_{hp} increases, the amplitude of the solitary profile decreases. Figures 2(a), (b), and (c) show that when light positive ions are isotropic and light negative ions are anisotropic, the width is at its maximum. For fast mode, the solitary profile is rarefactive. The slow mode is depicted in Fig. 3 for the same combination as in Fig. 2. The solitary profile in this instance is compressive. The fast and slow modes are always precisely opposite to one another. This is

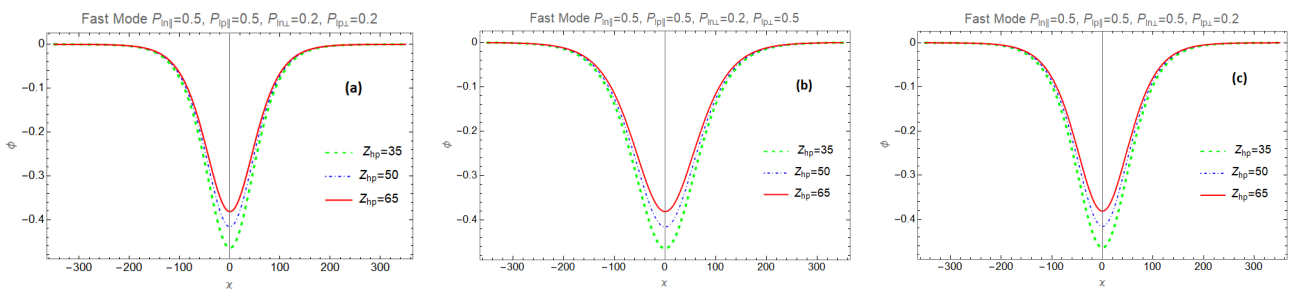


Figure 2. Solitary profile of fast mode with variation of heavy positive ion

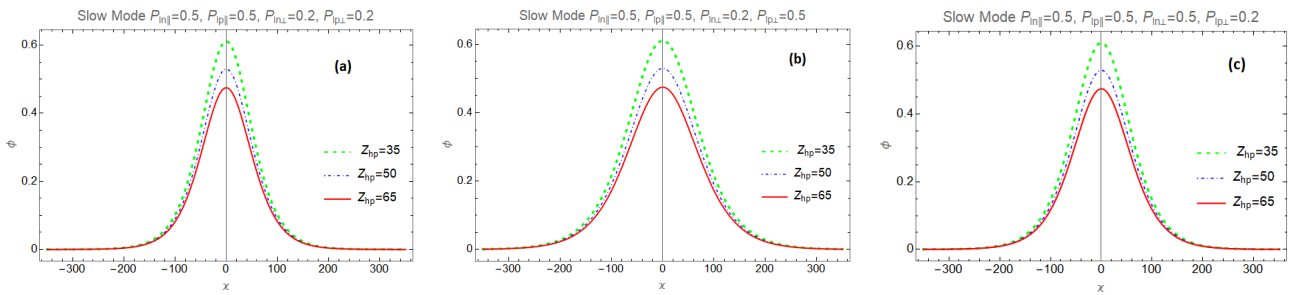


Figure 3. Solitary profile of slow mode with variation of heavy positive ion

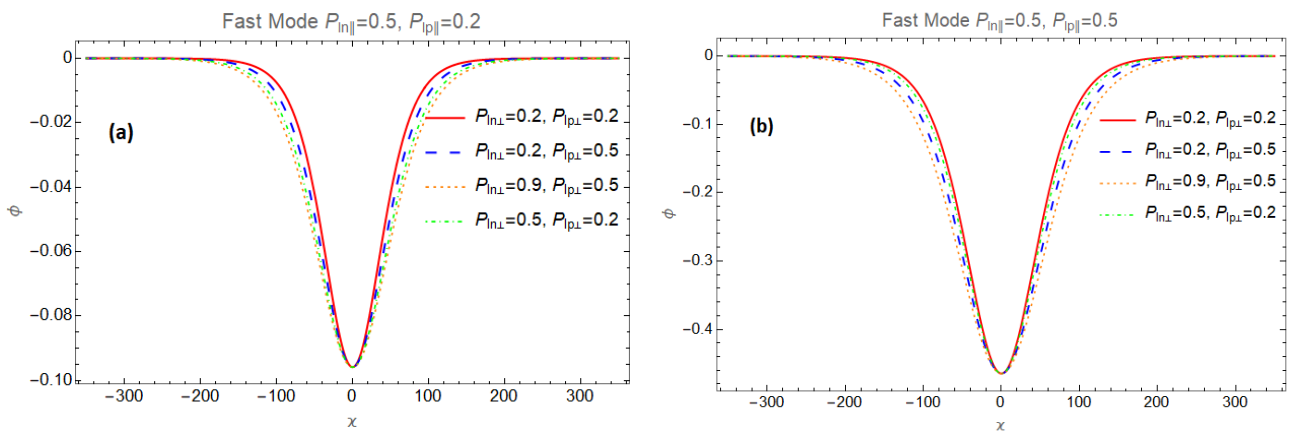


Figure 4. Solitary profile of fast mode with different combination of perpendicular pressure of light positive ion and light negative ion.

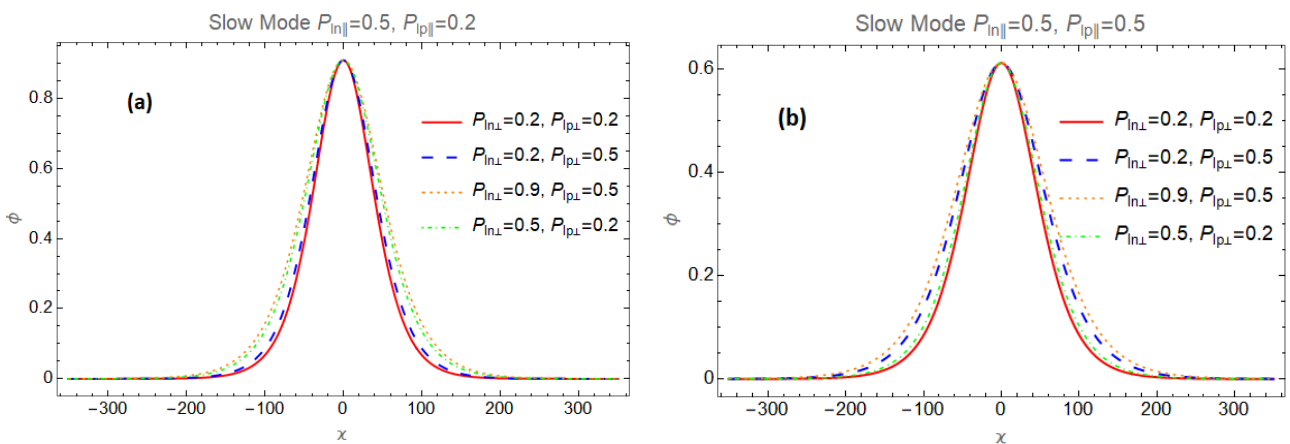


Figure 5. Solitary profile of slow mode with different combination of perpendicular pressure of light positive ion and light negative ion.

an intrinsic property of the plasma that has been investigated both theoretically and experimentally. If the fast mode is compressive (rarefactive), the slow mode is rarefactive (compressive).

Figures 4 and 5 depict the changes in the solitary profile for different combinations of perpendicular pressure. Perpendicular pressure to the wave affects its width, but its amplitude stays constant. The width reaches its greatest when both light negative ion and light positive ions are anisotropic for $P_{ln\parallel} > P_{lp\parallel}$ (figs. 4a and 5a), but it is at its highest when light negative ion is anisotropic but light positive ion is isotropic for $P_{ln\parallel} = P_{lp\parallel}$ (figs. 4b and 5b)

5. DYNAMICAL SYSTEM ANALYSIS

Phase plane analysis is a useful tool that is widely used in fusion research to understand the dynamics and stability of plasma systems. A phase plane in plasma physics generally shows the development of two relevant factors, including temperature and plasma density. Achieving controlled and persistent fusion reactions requires maintaining the stability of plasma systems.

Regarding our research and phase plane analysis, we would like to state that the reason for this section of the manuscript is that the phase plane technique entails visually identifying whether limit cycles are present in a differential equation's solutions. Scientists examine plasma state trajectories and equilibrium point locations using phase plane analysis. The way that small deviations from these equilibrium points change over time is how stability is determined. The solutions are interpreted as a family of functions that are graphically depicted as a two-dimensional vector field in the phase plane. At typical points, arrows denoting the derivatives of points with respect to a parameter are drawn. The system's behavior throughout the examined plane regions can be seen by constructing these vectors, which makes limit cycle identification easier. Phase portrait refers to the overall visual representation, and phase path refers to a particular trajectory along a flow line (a path tangent to the vectors).

In order to obtain the dynamical system equation we apply the transformation of the space and variable as $\chi = \xi - U\tau$ and finally obtain the transformed equation as

$$\begin{aligned} \frac{d\phi}{d\chi} &= z \\ \frac{dz}{d\chi} &= \frac{U}{DA}\phi - \frac{1}{2D}\phi^2 \end{aligned} \tag{15}$$

The Hamiltonian of the system (15) is

$$H = \frac{1}{2}z^2 - \frac{U}{2DA}\phi^2 - \frac{1}{6D}\phi^3 \tag{16}$$

The dynamical system described by (15) involves the equilibrium points $P = (0, 0)$ and $Q = (0, \frac{2U}{A})$.

To derive the eigenvalues, it is essential to have the Jacobian matrix (JM) of the dynamical system. It is evident that system (15) can be expressed as

$$\begin{pmatrix} \phi \\ z \end{pmatrix} = \begin{pmatrix} 0 & 1 \\ \frac{U}{DA} - \frac{1}{2D}\phi & 0 \end{pmatrix} \begin{pmatrix} \phi \\ z \end{pmatrix} \tag{17}$$

The expression for the JM is

$$J = \begin{pmatrix} 0 & 1 \\ \frac{U}{DA} - \frac{1}{2D}\phi & 0 \end{pmatrix} \tag{18}$$

The eigenvalues can be found by using the relation $|J - \lambda I| = 0$. Where I indicates the identity matrix. The eigenvalues are provided by $\lambda_{a,b} = \pm\sqrt{\frac{U}{DA} - \frac{1}{2D}\phi}$. At $P = (0, 0)$ as the first equilibrium point, the eigenvalues are $\pm\sqrt{\frac{U}{DA}}$ and at the second equilibrium point $Q = (0, \frac{2U}{A})$, the eigenvalues are $\pm\sqrt{-\frac{U}{DA}}$. Utilizing the concept of dynamical systems [] we can see that the first equilibrium point is saddle and the second equilibrium point is centre if $\frac{U}{DA} > 0$. If $\frac{U}{DA} < 0$ the nature of the points will reverse. Note that $P = (0, 0)$ must be a saddle point always in order for the results to be physically plausible. The condition for Q to be a saddle point is when the phase speed is negative, which contradicts physically. But Q can be positioned on either the positive or negative axis for centers, which means Q can either be $(0, \frac{2U}{A})$ or $(0, -\frac{2U}{A})$

It is self-explanatory to see the phase portraits themselves. They display how various parameters affect the structure of orbits and how equilibrium points shift. In figures the limit cycles are seen to travel along the z axis. Figure 6 is plotted for the fast mode with variation Z_{hp} . We see that the centre Q is in the negative z-axis as the nonlinear coefficient A is negative. We can see in figure 8, A is positive in slow mode then Q is positioned in the positive z-axis. The centre Q moves towards to saddle point P with increasing charge of heavy positive ion (Z_{hp}) (figure 6 and 7). Referring to figures 8 and 9 we observe that the centre moves closest to saddle point when the light positive ion is anisotropic and light negative ion is isotropic and when both are anisotropic, the centre moves away from the saddle point.

6. CONCLUSIONS

In this paper we have studied the effect of pressure anisotropy in a collisionless plasma composed of charged state of heavy positive ion and light positive as well as negative ion. Using reductive perturbation technique Kdv equation is

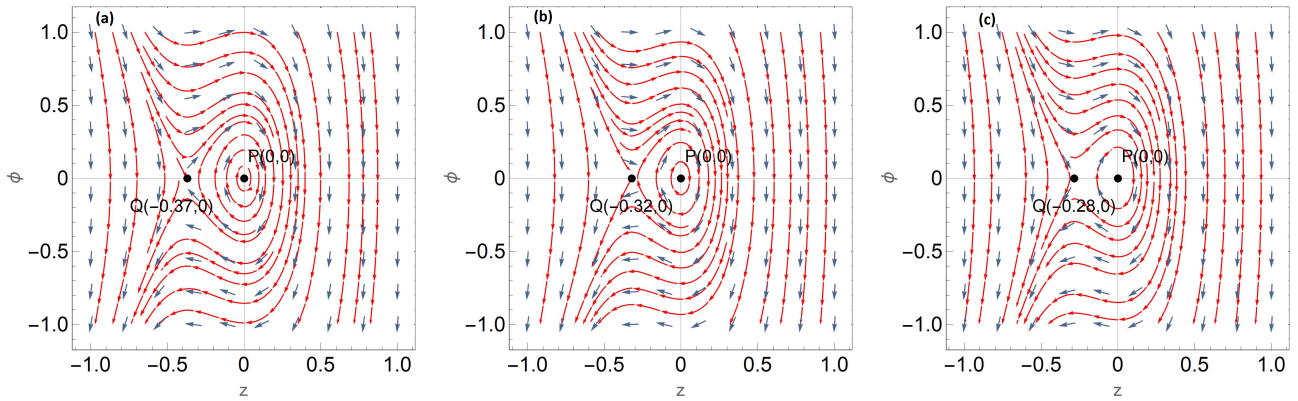


Figure 6. Phase portrait of the system (15) for fast mode when $P_{ln\parallel} = 0.5, P_{lp\parallel} = 0.5, P_{ln\perp} = 0.2, P_{lp\perp} = 0.2$ (i) $Z_{hp} = 35$, (ii) $Z_{hp} = 50$, (iii) $Z_{hp} = 65$

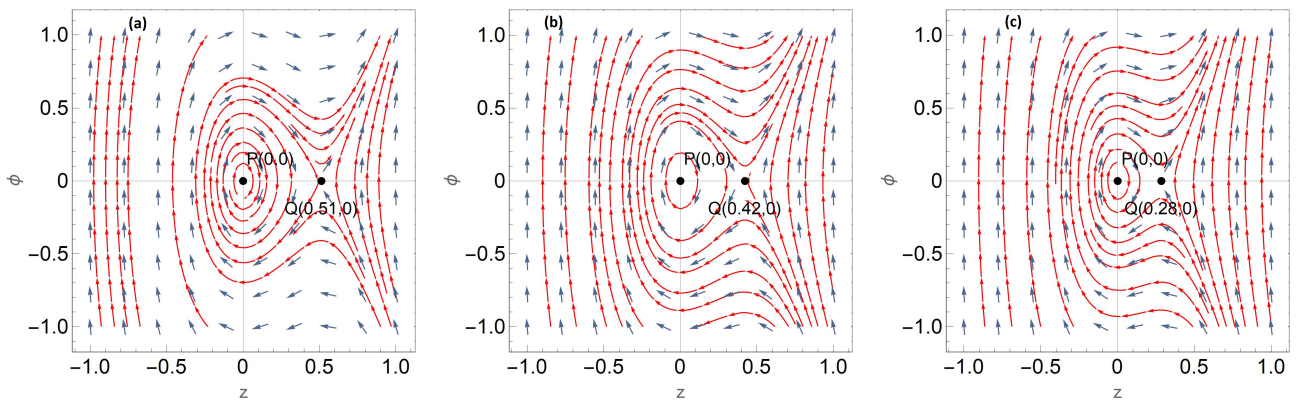


Figure 7. Phase portrait of the system (15) for slow mode when $P_{ln\parallel} = 0.5, P_{lp\parallel} = 0.5, P_{ln\perp} = 0.2, P_{lp\perp} = 0.2$ (i) $Z_{hp} = 35$, (ii) $Z_{hp} = 50$, (iii) $Z_{hp} = 65$

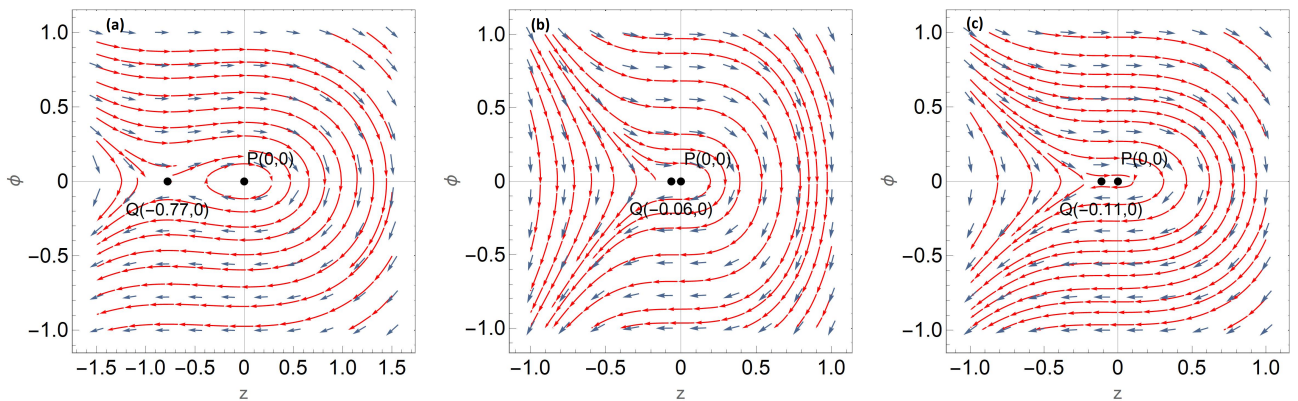


Figure 8. Phase portrait of the system (15) for fast mode when $Z_{hp} = 35, P_{ln\parallel} = 0.5, P_{lp\parallel} = 0.5, P_{lp\perp} = 0.2$ (i) $P_{ln\perp} = 0.5$, (ii) $P_{ln\perp} = 0.2$, (iii) $P_{ln\perp} = 0.9$

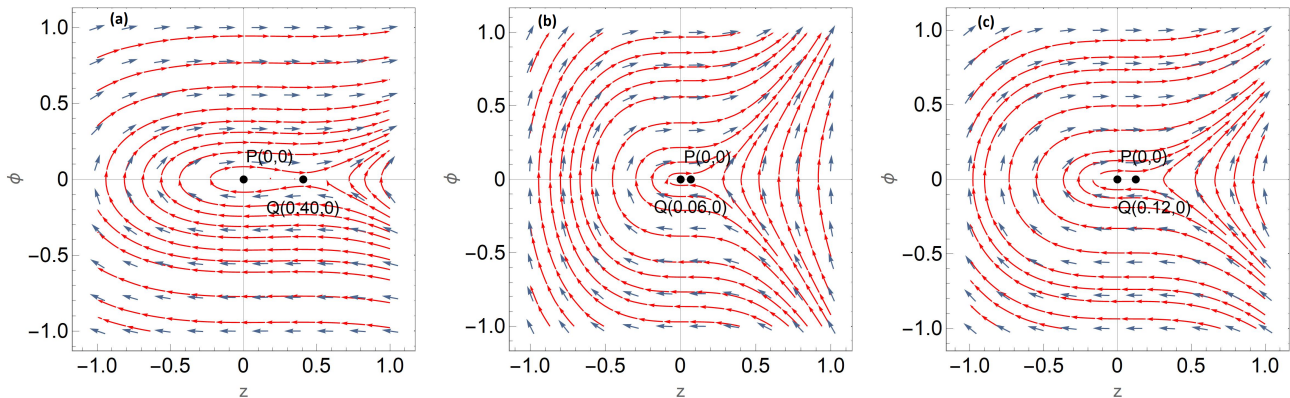


Figure 9. Phase portrait of the system (15) for slow mode when $Z_{hp} = 35$, $P_{In||} = 0.5$, $P_{Ip||} = 0.5$, $P_{Ip\perp} = 0.2$ (i) $P_{In\perp} = 0.5$, (ii) $P_{In\perp} = 0.2$, (iii) $P_{In\perp} = 0.9$

derived and found the analytic solution. For the system under investigation, a biquadratic dispersion relation has been derived, yielding the fast and slow modes. We observed that the phase velocity is within subsonic range in both fast mode and slow mode. We found that compressive structures are formed for the slow mode, while rarefactive solitary structures are formed for the fast mode. It was found that the soliton width is influenced by the perpendicular pressure but the amplitude remains the same. However that the amplitude of the solitary profile is influenced by the charge state of heavy positive ion. We then convert our evolutionary equation into a system of two ordinary differential equations (ODEs) in order to do a phase plane analysis. We extract significant information about the stability of stationary structures given by the KdV equation via dynamical system analysis. We have introduced the center and saddle points and graphically displayed the phase portrait of the stated plasma system for various values.

Acknowledgement

Deepsikha Mahanta would like to thank Govt. of Assam for providing the Ph.D. Research Scholarship under the Director of Higher Education, Assam, Kahilipara, Guwahati-19.

ORCID

Deepsikha Mahanta, <https://orcid.org/0009-0000-5855-2279>; Jnanjyoti Sarma, <https://orcid.org/0000-0002-0793-5680>

REFERENCES

- [1] T. Mohsenpoura, H. Ehsanib, and M. Behzadipourc, "Ion-acoustic solitons in negative ion plasma with relativistic degenerate electrons and positrons," *Waves in Random and Complex Media*, **34**, 845-857 (2024). <https://doi.org/10.1080/17455030.2021.1919338>
- [2] H. Washimi, and T. Taniuti, "Propagation of ion-acoustic solitary waves of small amplitude," *Physical Review Letters*, **17**, 996 (1966). <https://doi.org/10.1103/PhysRevLett.17.996>
- [3] B.D. Fried, R.B. White, and T.K. Samec, "Ion acoustic waves in a multi-ion plasma," *Physics of Fluids*, **14**, 2388 (1971). <https://doi.org/10.1063/1.1693346>
- [4] N. Nakamura, M. Nakamura, and T. Itoh, "Observation of two ion-acoustic waves in an argon-helium plasma," *Physical Review Letters*, **37**, 209-212 (1976). <https://doi.org/10.1103/PHYSREVLETT.37.209>
- [5] M.Q. Tran, and S. Coquerand, "Propagation of argon- and helium-ion acoustic modes in an argon helium plasma," *Physical Review A*, **14**, 2301-2306 (1976). <https://doi.org/10.1103/PhysRevA.14.2301>
- [6] M.Q. Tran, "Ion acoustic solitons in a plasma: a review of their experimental properties and related theories," *Physica Scripta*, **20**, 317-327 (1979). <https://doi.org/10.1088/0031-8949/20/3-4/004>
- [7] R.B. White, B.D. Fried, and F.V. Coroniti, "Structure of ion acoustic solitons and shock waves in a two component plasma," *Physics of Fluids*, **15**, 1484-1490 (1972). <https://doi.org/10.1063/1.1694112>
- [8] S. Chandrasekhar, "The density of white dwarf stars," *Philosophical magazine letters*, **11**, 592-596 (1982). <https://doi.org/10.1080/14786443109461710>
- [9] S. Chandrasekhar, "The Maximum Mass of Ideal White Dwarfs," *The Astrophysical Journal*, **74**, 81 (1931). <https://doi.org/10.1086/143324>
- [10] H.M. Van Horn, "Dense Astrophysical Plasmas," *Science*, **252**, 384-389 (1991). <https://doi.org/10.1126/science.252.5004.384>
- [11] S. Jahan, E. Booshrat, Sharmin., N.A. Chowdhury, A. Mannan, T.S. Roy, and A.A. Mamun, "Electrostatic Ion-Acoustic Shock Waves in a Magnetized Degenerate Quantum Plasma," *Plasma*, **4**, 426-434 (2021). <https://doi.org/10.3390/plasma4030031>

- [12] M.R. Hossen, and A.A. Mamun, "Nonplanar shock excitations in a four component degenerate quantum plasma: the effects of various charge states of heavy ions," *Plasma Science and Technology*, **17**, 177 (2015). <https://doi.org/10.1088/1009-0630/17/3/01>
- [13] P. Chaizy, H. Rème, J.A. Sauvaud, C. d'Uston, R.P. Lin, D.E. Larson, D.L. Mitchell, et al., "Negative ions in the coma of comet Halley," *Nature*, **349**, 393–396 (1991). <https://doi.org/10.1038/349393a0>
- [14] H. Massey, *Negative Ions*, 3rd edition, Cambridge University Press, Cambridge, 1976).
- [15] M. Bacal, and G.W. Hamilton, " H^- and D^- Production in Plasmas," *Physical Review Letters*, **42**, 1538 (1979). <https://doi.org/10.1103/PhysRevLett.42.1538>
- [16] J. Jacquinot, B.D. McVey, and J.E. Scharer, "Mode conversion of the fast magnetosonic wave in a deuterium-hydrogen tokamak plasma," *Physical Review Letters*, **39**, 88 (1977). <https://doi.org/10.1103/PhysRevLett.39.88>
- [17] R.A. Gottscho, and C.E. Gaebe, "Negative ion kinetics in RF glow discharges," *IEEE transactions on plasma science*, **14**, 92-102 (1986). <https://doi.org/10.1109/TPS.1986.4316511>
- [18] A.A. Mamun, "Degenerate pressure driven self-gravito-acoustic solitary waves in a self-gravitating degenerate quantum plasma system," *Physics of Plasmas*, **25**, 022307 (2018). <https://doi.org/10.1063/1.5013138>
- [19] A.A. Mamun, "Self-gravito-acoustic waves and their instabilities in a self-gravitating degenerate quantum plasma system," *Contributions to Plasma Physics*, **60**, e201900080 (2019). <https://doi.org/10.1002/ctpp.201900080>
- [20] S. Islam, S. Sultana, and A.A. Mamun, "Ultra-low frequency shock dynamics in degenerate relativistic plasmas," *Physics of Plasmas*, **24**, 092308 (2017). <https://doi.org/10.1063/1.4994196>
- [21] S. Islam, S. Sultana, and A.A. Mamun, "Envelope solitons in three-component degenerate relativistic quantum plasmas," *Physics of Plasmas*, **24**, 092115 (2017). <https://doi.org/10.1063/1.5001834>
- [22] M. Adnan, G. Williams, A. Qamar, S. Mahmood, and I. Kourakis, "Pressure anisotropy effects on nonlinear electrostatic excitations in magnetized electron-positron-ion plasmas," *The European Physical Journal D*, **68**, 1-15 (2014). <https://doi.org/10.1140/EPJD%2014-50384-Y>
- [23] M.K. Deka, D. Mahanta, A.N. Dev, J. Sarma, S.K. Mishra, and E. Saikia, "Propagation of ion beam modes in a spin degenerate quantum magneto plasma in presence of ionic pressure anisotropy," *AIP Conference Proceedings*, **2819**, 070004 (2023). <https://doi.org/10.1063/5.0137748>
- [24] M.K. Deka, D. Mahanta, A.N. Dev, J. Sarma, S.K. Mishra, and E. Saikia, "Features of shock wave in a quantized magneto plasma under the influence of ionic pressure anisotropy and anisotropic viscosity," *AIP Conference Proceedings*, **2819**, 070005 (2023). <https://doi.org/10.1063/5.0137746>
- [25] Almas, Ata-ur-Rahman, N. Faiz, D.M. Khan, W. Emam, and Y. Tashkandy, "Oblique Arbitrary Amplitude Dust Ion Acoustic Solitary Waves in Anisotropic Non-Maxwellian Plasmas with Kappa-Distributed Electrons," *Symmetry*, **15**, 1843 (2023). <https://doi.org/10.3390/sym15101843>
- [26] M. Khalid, A. Kabir, and L.S. Jan, "Qualitative analysis of nonlinear electrostatic excitations in magnetoplasma with pressure anisotropy," *Zeitschrift für Naturforschung A*, **78**, 339–345 (2023). <https://doi.org/10.1515/zna-2022-0312>
- [27] S. Mahmood, S. Hussain, W. Masood, and H. Saleem, "Nonlinear electrostatic waves in anisotropic ion pressure plasmas," *Physica Scripta*, **79**, 045501 (2009). <https://doi.org/10.1088/0031-8949/79/04/045501>
- [28] M. Manesh, S. Sijo, V. Anu, G. Sreekal, T.W. Neethu, D.E. Savithri, and C. Venugopal, "Effect of anisotropy of lighter and heavier ions on solitary waves in a multi-ion plasma," *Physics of Plasma*, **24**, 062905 (2017). <https://doi.org/10.1063/1.4986107>
- [29] S.U. Khan, M. Adnan, S. Mahmood, H. Ur-Rehman, and A. Qamar, "Effect of pressure anisotropy on nonlinear periodic waves in a magnetized superthermal electron-positron-ion plasma," *Brazilian Journal of Physics*, **49**, 379–390 (2019). <https://doi.org/10.1007/s13538-019-00653-w>
- [30] M. Khalid, and A. Rahman, "Ion acoustic cnoidal waves in a magnetized plasma in the presence of ion pressure anisotropy," *Astrophysics and Space Science*, **364**, 28 (2019). <https://doi.org/10.1007/s10509-019-3517-0>
- [31] G. Bordbar, and M. Karami, "Anisotropic magnetized neutron star," *The European Physical Journal C*, **82**, 74 (2022). <https://doi.org/10.1140/epjc/s10052-022-10038-0>
- [32] A. Patidar, and P. Sharma, "Magnetohydrodynamic wave modes in relativistic anisotropic quantum plasma," *Physics of Plasmas*, **27**, 042108 (2020). <https://doi.org/10.1063/1.5143764>
- [33] M. Ifran, S. Ali, and A.M. Mirza, "Solitary waves in a degenerate relativistic plasma with ionic pressure anisotropy and electron trapping effects," *Physics of plasmas*, **24**, 052108 (2017). <https://doi.org/10.1063/1.4981932>
- [34] B. Pradhan, A. Gowrisankar, A. Abdikian, S. Banerjee, and A. Saha, "Propagation of ion-acoustic wave and its fractal representations in spin polarized electron plasma," *Physica Scripta*, **98**, 6 (2023). <https://doi.org/10.1088/1402-4896/acd3bf>
- [35] E.F. El-Shamy, R.C. Al-Chouikh, A. El-Depsy, and N.S. Al-Wadie, "Nonlinear propagation of electrostatic travelling waves in degenerate dense magnetoplasmas," *Physics of Plasmas*, **23**, 122122 (2016). <https://doi.org/10.1063/1.4972817>
- [36] K. Singh, P. Sethi, and N.S. Saini, "Nonlinear excitations in a degenerate relativistic magneto-rotating quantum plasma," *Physics of Plasmas*, **26**, 092104 (2019). <https://doi.org/10.1063/1.5098138>
- [37] W.F. El-Taibany, E.E. Behery, S.K. El-Labany, and A.M. Abdelghany, "Gravitoelectrostatic excitations in an opposite polarity complex plasma," *Physics of Plasmas*, **26**, 063701 (2019). <https://doi.org/10.1063/1.5092514>

- [38] P.K. Prasad, and A. Saha, "Bifurcation analysis of ion-acoustic waves for Schrödinger equation in nonextensive Solar wind plasma," *Advances in Space Research*, **67**, 9-19 (2021). <https://doi.org/10.1016/j.asr.2020.07.031>
- [39] A. Saha, B. Pradhan, and S. Banerjee, "Bifurcation analysis of quantum ion-acoustic kink, anti-kink and periodic waves of the Burgers equation in a dense quantum plasma," *The European Physical Journal Plus*, **135**, 216 (2020). <https://doi.org/10.1140/epjps13360-020-00235-9>
- [40] M.M. Selim, A. El-Depsy, and E.F. El-Shamy, "Bifurcations of nonlinear ion-acoustic travelling waves in a multicomponent magnetoplasma with superthermal electrons," *Astrophysics and Space Science*, **360**, 66 (2015). <https://doi.org/10.1007/s10509-015-2574-2>
- [41] R.A. Shahein, and A.R. Seadawy, "Bifurcation analysis of KP and modified KP equations in an unmagnetized dust plasma with nonthermal distributed multi-temperatures ions," *Indian Journal of Physics*, **93**, 941-949 (2019). <https://doi.org/10.1007/s12648-018-1357-3>
- [42] Prasad P.K., and Saha A. "Dynamical behavior and multistability of ion-acoustic waves in a magnetized Auroral zone plasma," *Journal of Astrophysics and Astronomy*, **42**, 9 (2021). <https://doi.org/10.1007/s12036-021-09721-7>
- [43] M.K. Islam, S. Biswas, N.A. Chowdhury, A. Mannan, M. Salahuddin, and A.A. Mamun, "Obliquely propagating ion-acoustic shock waves in a degenerate quantum plasma," *Contributions to Plasma Physics*, **62**, e202100073 (2021). <https://doi.org/10.1002/ctpp.202100073>
- [44] N. Akhtar, and S. Mahmood, "Effect of Ion Temperature Anisotropy on Modulated Electrostatic Waves and Envelope Solitons in a Magnetized Plasma," *IEEE Transactions on Plasma Science*, **50**, 3760-3773 (2022). <https://doi.org/10.1109/TPS.2022.3200476>
- [45] J.A. Bittencourt, *Fundamentals of Plasma Physics*, 3rd ed. (Springer, New York, NY, USA, 2004).
- [46] G.F. Chew, M.L. Goldberger, and F.E. Low, "The Boltzmann equation and the one-fluid hydromagnetic equations in the absence of particle collisions," *Mathematical, Physical and Engineering Sciences*, **236**(1204), 112–118 (1956). <https://www.jstor.org/stable/99870>
- [47] M. Irfan, S. Ali, S.A. El-Tantawy, and S.M.E. Ismaeel, "Three dimensional ion-acoustic rogons in quantized anisotropic magnetoplasmas with trapped/untrapped electrons," *Chaos*, **29**, 103133 (2019). <https://doi.org/10.1063/1.5109157>
- [48] W. Baumjohann, and R.A. Treumann, *Basic Space Plasma Physics*, (Imperial College Press, London, 1996).
- [49] E.I. El-Awady, and M. Djebli, "Dust acoustic waves in a collisional strongly coupled dusty plasmas," *Astrophysics and Space Science*, **342**, 105–111 (2012). <http://dx.doi.org/10.1007/s10509-012-1159-6>

ЕВОЛЮЦІЯ ОДИНОЧНОЇ ХВИЛІ В КВАНТОВАНІЙ МАГНІТОПЛАЗМІ БЕЗ ЗІТКНЕНЬ З АНІЗОТРОПІЄЮ ІОННОГО ТИСКУ

Діпсіха Маханга^a, Джнандйоті Сарма^b

^aДепартамент математики, Університет Гаухаті, Гувахаті 781014, Індія

^bДепартамент математики, коледж Радха Говінда Баруа, Гувахаті 781025, Індія

Ця стаття представляє комплексне дослідження плазми без зіткнень, що складається із зарядженого стану важкого позитивного іона та легкого позитивного, а також негативного іона. Виводячи рівняння Кортевега-де Фріза (KdV) і використовуючи його стандартне рішення, ми аналізуємо характеристики ізольованого профілю за змінних параметрів. Ми виявили, що розчин дає як розріджений, так і стиснутий солітон. Для повільного режиму формуються стислі структури, а для швидкого – розріджені солітарні структури. Крім того, із застосуванням теорії біфуркацій планарних динамічних систем проаналізовано фазові портрети. Цей аналіз динамічної системи дозволив нам отримати важливу інформацію про стабільність цих структур, представлену рівнянням KdV.

Ключові слова: рівняння KdV; поодинокі хвилі; квантова плазма; анізотропія тиску; аналіз фазової площини; динамічна система

TAKING THE NULL-HYPERSURFACE LIMIT IN THE PARIKH-WILCZEK MEMBRANE APPROACH

 **A.M. Arslanaliev**^a,  **A.J. Nurmagambetov**^{a,b,c*}

^a*Akhiezer Institute for Theoretical Physics of NSC KIPT, 1 Akademichna St., Kharkiv, 61108, Ukraine*

^b*V.N. Karazin Kharkiv National University, 4, Svoboda Sq., Kharkiv, 61022, Ukraine*

^c*Usikov Institute of Radiophysics and Electronics, 12 Ak. Proskury, Kharkiv, 61085, Ukraine*

* *Corresponding Author e-mail: ajn@kipt.kharkov.ua*

Received August 7, 2024; revised October 8, 2024; accepted November 7, 2024

We consider subtleties of the horizon (null-hypersurface) limit in the Parikh-Wilczek Membrane Approach to Black Holes. Specifically, we refine the correspondence between the projected Einstein equations of gravity with matter and the Raychaudhuri-Damour-Navier-Stokes (RDNS) equations of relativistic hydrodynamics. For a general configuration of gravity with matter we obtain additional terms in the hydrodynamic equations, which include very specific combinations of the contracted logarithmic derivatives of a parameter (the regularization function) determining the proximity of a stretched membrane to the black hole horizon. Nevertheless, direct computations of the new terms for exact (Schwarzschild and Kerr) black hole solutions prompt the standard form of the RDNS equations, due to the non-expanding horizon property of these solutions. Therefore, the reduction of the extended RDNS equations to their classical form may be viewed as an additional consistency condition in the exact black hole solutions hydrodynamics, and may serve as a non-trivial test for various viable approximations of spacetime metrics. We compare in detail the Parikh-Wilczek Membrane Approach with theourgoulhon-Jaramillo method of a null-hypersurface description, as well as give the link of the obtained results to our previous work on the Kerr black holes.

Keywords: *Black holes; Membrane Paradigm; Relativistic hydrodynamics*

PACS: 04.70.-s, 04.20.Jb, 04.40.Nr

1. INTRODUCTION

The Membrane Paradigm [1] is one of the prominent ways to describe effective degrees of freedom on a Black Hole (BH) horizon. According to the Paradigm, a BH horizon is modeled by a stretched, penetrable and impacted by electromagnetic field membrane, dynamics of which is given by hydrodynamic-type equations for a viscous relativistic fluid [2–4]. In this way, the collective dynamics of fields near the event horizon is substituted by the dynamics of the dual fluid.

Interest in the hydrodynamic dual description of non-gravitational fields was increased after the AdS/CFT Duality foundation, and, as it was realized, some of the predictions of the Membrane Paradigm are directly related to outcomes of the AdS/CFT. Nevertheless, the Membrane Paradigm is in no way equated to the AdS/CFT correspondence [5,6]. Though a similarity between these approaches was mentioned since the early stages of the dual CFT hydrodynamics development [7,8], mainly due to the universal character of the transport coefficients of the dual fluid [7–10], the Membrane Paradigm can, at best, be treated as a leading AdS/CFT approximation, or as its low-energy limit (see [11,12] in this respect). Yet, further advances of the Membrane Paradigm may open new prospects in the AdS/CFT Duality progress.

In our previous work, Ref. [13], we extended the Membrane Paradigm to the case of rotating BHs. (Strictly speaking, in [13] we used the Membrane Paradigm in part, since we solely focused on the external part of the Kerr spacetime. We thank Prof. O.B. Zaslavskii for comments in this respect. Note, however, that this restriction is enough in solving for the problem how a black hole is viewed for an external observer as a “fluid”.) Operating with the Kerr solution in the Boyer-Lindquist coordinates, we came to the conclusion on the divergence of the momentum density of the dual fluid on the horizon. In General Relativity the divergence of a quantity on the horizon may be caused by the coordinates choice. So that one of the motivations for this paper is to re-derive the main characteristics of the dual fluid in the Eddington-Finkelstein parametrization of the Kerr metric, and to study their behavior in the vicinity of the horizon.

Accomplishing our goals requires the revision of main equations for the dual fluid, containing as the transport coefficients, as well as other basic characteristics – energy, pressure, expansion, the momentum vector and the shear tensor – of the medium. Previously, in [13], we derived the transport coefficients etc. of the effective dual medium by comparing the energy-momentum tensor (EMT) of the stretched membrane with the conventional EMT of a relativistic viscous fluid. Here, we will recover the characteristics of the fluid from hydrodynamic-type equations, to which the projected, onto a null hypersurface, Einstein equations with matter are reduced.

Specifically, 1+3 decomposition of time-like and space-like directions reduces the GR equations to external/internal geometry of a hypersurface, embedded into the target space. These equations are well-known as the Gauss and Codazzi-Mainardi equations (see, e.g., [14–17]).¹ Further division of spatial directions [4] makes it possible to present the projected, onto a 2D hypersurface, Gauss-Codazzi equations as the Raychaudhuri and the Navier-Stokes type equations [3, 4, 15, 16, 18–20]. The system of these equations² determines the transport coefficients and other mentioned characteristics of the dual to the stretched membrane effective substance. But there is a subtlety, related to the fact, that the Gauss-Codazzi equations become the hydrodynamic-type equations only in the null-hypersurface limit. Taking this limit is a non-trivial task, that should be performed with additional care.

Indeed, there is the apparent conceptual difference in the geometric description of space-like (a stretched membrane type) and null (a BH horizon type) hypersurfaces, embedded into 4D space-time of the Minkowski signature. For a space-like hypersurface one needs two orthogonal to the hypersurface time-like and space-like vectors. These vectors can be represented in terms of two linearly independent null vectors, which makes the description more universal. The case of a null-hypersurface, the intrinsic metric of which degenerates, requires coincidence of two linear-independent null-vectors. Therefore, in the null-hypersurface limit, when the stretched membrane becomes the event horizon, it comes to be important to obtain null-vectors from the originally time- and space-like ones, and to make them equal on the null-surface in the last step.

On the way to this end, we want to revise, first, the procedure of getting the Raychaudhuri and the Damour-Navier-Stokes (RDNS) equations [3, 4, 15, 16] from the projected Gauss-Codazzi equations in the Parikh-Wilczek Membrane Approach. The main revision concerns the way of taking the horizon (the null-hypersurface) limit, i.e., of transition to finite on the horizon quantities by the regularization. Details of this procedure can be found, e.g., in [4, 13].

Within the Membrane Approach of Ref. [4], the null-hypersurface limit is organized as setting the regularization factor (some coordinate function) to zero. The role of this function is to provide the finiteness of the divergent on the event horizon stress-energy tensor of a stretched membrane. On the other hand, this regularization factor can be viewed as a degree of proximity of the membrane to the true horizon. The outcome of taking the null-hypersurface limit in the Membrane Approach, without a reference to the specific type of space-time, consists in the extension of the RDNS-type equations by terms with the contracted logarithmic derivatives of the regularization factor. This result can be found in Section 2. In this section we also formulate two conditions on the regularization factor, called hereafter as the “consistency conditions”, the fulfillment of which reduces the extended RDNS equations to their classical version [3, 18].³

Second, we want to verify the validity of the obtained consistency conditions on two exact solutions to the Einstein equations. This part of our studies is presented in Section 3. Here we consider the Schwarzschild and the Kerr solutions in the Eddington-Finkelstein coordinates. The simplicity of the Schwarzschild metric does not allow us to fully evaluate possible limitations associated with the consistency conditions: they satisfy identically in the case. Performing the relevant computations for the Kerr solution is a less trivial task. However, our consistency conditions hold even in this case. Since the fulfillment of these conditions requires the tight coordination of different elements of a space-time metric, we can expect the same outcome for any exact BH solution to the Einstein equations, where such coordination takes place. The ground for such expectations is based on the ideology of the Membrane Approach to regularize the divergent on the horizon quantities, and to construct in this way the effective dynamical description of the horizon hypersurface in terms of the finite variables. Therefore, the established consistency conditions should hold for various viable approximations of spacetime metrics in the appropriate approximation order as well.⁴

Conclusions contain a summary of our findings, their applications and further developments. Appendix A includes details on the surface gravity, computation of which is another non-trivial check of the consistency of a BH-type solution. Since our research focuses on the description of null-hypersurfaces, we pay special attention to comparing the approach used here with the approach of [15, 16]. In Appendix B we demonstrate the equivalence of the generalized Damour-Navier-Stokes equation of Ref. [15] to the DNS-type equation from Section 2.1, obtained within the Membrane Approach [4]. Appendix C contains the overview of taking the null-hypersurface limit of the generalized DNS equation from Ref. [15], that again leads us to the consistency conditions from Section 2.2. Recall, nothing special to recover the standard form of the DNS equation was required in Ref. [15] upon taking the horizon limit. We briefly comment on the nature of discrepancies between two approaches in this respect.

We use the following notation throughout the paper. The 4D metric signature is chosen to be the mostly positive one. All indices (no matter what kind of, Latin or Greek) are supposed to be the indices of 4D target space. g_{ab} , h_{ab} and γ_{ab} are the 4D metric, 3D and 2D induced metric tensors, respectively. The induced metrics of low-dimensional spaces are used as projection operators. Then, ∇_a symbol denotes 4D covariant (w.r.t. g_{ab}) derivative; ${}^3\mathcal{D}_a$ and ${}^2\mathcal{D}_a$ are the

¹Following Misner, Thorne and Wheeler [14], we will refer to these equations as the Gauss-Codazzi equations.

²Since the expansion and the shear tensor are also characteristics of the fluid, we refer to the Raychaudhuri equation as to a hydrodynamic-type equation.

³Note that the generalization of the Damour-Navier-Stokes equation in the vicinity of the horizon has been obtained in Ref. [15]. In two added Appendices B and C we give the detailed comparison of the approach of [15] and the Membrane Approach we follow in the paper, as well as we outline the correspondence of the obtained by us consistency conditions to the null-hypersurface limit of [15].

⁴Then, the viability of an approximate solution for the space-time metric can be evaluated comparing the approximation orders of the solution and of the consistency conditions: the approximation order of the consistency conditions has to be the same, or higher than that of the solution.

covariant derivatives w.r.t. 3D and 2D induced metrics. The explicit form of ${}^3\mathcal{D}_a$ and ${}^2\mathcal{D}_a$ is given in the main text of the paper. In Appendices B and C we use the conventions of Refs. [15, 16] to simplify the comparison of different approaches to each other.

2. RELATIVISTIC HYDRODYNAMICS OF THE MEMBRANE APPROACH

2.1. From the Gauss-Codazzi to the Damour-Navier-Stokes and the Raychaudhuri equations

The starting point of our consideration (see [4] for details) is the Gauss-Codazzi equation in the 1 + 3 decomposition of metric:

$${}^3\mathcal{D}^b t_{ab} = -h_a^c T_{cd} n^d. \quad (1)$$

Here t_{ab} is the 3D stretched membrane energy-momentum tensor,

$$t_{ab} = \frac{1}{8\pi}(K h_{ab} - K_{ab}); \quad (2)$$

T_{ab} denotes the energy-momentum tensor (EMT) of matter fields. The space-like unit vector n^a ($n_a n^a = 1$) is orthogonal to the hypersurface of the stretched membrane, endowed with the induced metric $h_{ab} = g_{ab} - n_a n_b$. The extrinsic curvature tensor of the membrane hypersurface is determined by

$$K_{ab} = h_a^\alpha h_b^\beta \nabla_\beta n_\alpha; \quad (3)$$

$K = g^{ab} K_{ab}$ is its trace. The l.h.s. of eq. (1) also involves the 3D covariant derivative ${}^3\mathcal{D}_a$, whose action is specified by

$${}^3\mathcal{D}^c t_{ab} \equiv h^{c\gamma} h_a^\alpha h_b^\beta \nabla_\gamma t_{\alpha\beta}. \quad (4)$$

To bridge the Membrane Approach [4] to relativistic hydrodynamics, we have to introduce the time-like unit vector u^a ($u^a u_a = -1$) and to form the 2D (Euclidean) induced metric $\gamma_{ab} = h_{ab} + u_a u_b$. Then, by means of u_a and γ_{ab} , the membrane EMT t_{ab} is equivalently presented as

$$\hat{t}_{ab} \equiv 8\pi t_{ab} = \mathcal{E} u_a u_b + \mathcal{P} \gamma_{ab} + q_a u_b + q_b u_a + \tau_{ab}. \quad (5)$$

From the point of view of the original four-dimensional metric, eq. (5) requires the 1 + 1 + 2 metric decomposition

$$g_{ab} = -u_a u_b + n_a n_b + \gamma_{ab}, \quad (6)$$

where, by construction,

$$n^a h_{ab} = 0, \quad t_{ab} n^b = 0, \quad u^a n_a = 0, \quad \gamma_{ab} = h_{ab} + u_a u_b, \quad \gamma_{ab} n^b = \gamma_{ab} u^b = 0. \quad (7)$$

The physical meaning of quantities on the r.h.s. of eq. (5) is easy to derive from the Eckart approach to relativistic irreversible thermodynamics (see, e.g., Section 7.8 of [21] in this respect). The first two terms on the r.h.s. of (5) are treated as the energy density and the pressure; they form the EMT of an ideal fluid. A viscous fluid description requires adding the shear tensor τ_{ab} , responsible for anisotropic stresses, the heat flow vector q_a , as well as adding an extra contribution to the pressure due to the fluid viscosity. The heat flow vector and the shear tensor are characterized, in particular, by

$$q^b u_b = 0, \quad \tau_{ab} u^a = 0, \quad \tau_{ab} = \tau_{ba}, \quad \text{Tr} \tau_{ab} = 0.$$

However, it is convenient to consider the other set of common for the Membrane Approach variables

$$\hat{\theta} = -\mathcal{E}, \quad \hat{g} = \mathcal{P} - \frac{\hat{\theta}}{2}, \quad q_a = -\hat{\Omega}_a, \quad \tau_{ab} = -\hat{\sigma}_{ab}, \quad (8)$$

in terms of which \hat{t}_{ab} takes the following form:

$$\hat{t}_{ab} = -\hat{\theta} u_a u_b - \hat{\sigma}_{ab} + \left(\frac{\hat{\theta}}{2} + \hat{g} \right) \gamma_{ab} - \hat{\Omega}_a u_b - \hat{\Omega}_b u_a. \quad (9)$$

On account of the orthonormality/orthogonality conditions (7), for $\hat{\theta}$, $\hat{\Omega}_a$, \hat{g} and $\hat{\sigma}_{ab}$ we get

$$\begin{aligned} \hat{\theta} &= -\hat{t}_{ab} u^a u^b, \quad \hat{\Omega}_a = \hat{t}_{cb} u^b \gamma_a^c, \quad \hat{g} = \frac{1}{2} (\hat{t}_{ab} \gamma^{ab} + \hat{t}_{ab} u^a u^b), \\ \hat{\sigma}_{ab} &= - \left(\hat{t}_{cd} \gamma_a^c \gamma_b^d - \frac{1}{2} \gamma_{ab} (\hat{t}_{cd} \gamma^{cd}) \right). \end{aligned} \quad (10)$$

We now have everything we need to write eq. (1) as equations of a 2D viscous fluid. We project eq. (1) onto the transverse and the longitudinal with respect to u^a directions to this end:

$$\gamma_a^c \mathcal{D}^b \hat{t}_{cb} = -8\pi \gamma_a^c T_{cd} n^d, \quad u^a \mathcal{D}^b \hat{t}_{ab} = -8\pi T_{cd} u^c n^d. \tag{11}$$

Inserting the membrane EMT (9) into the orthogonal to u^a part of the Gauss-Codazzi equations, and taking into account the orthogonality of u^a and n^a to h_{ab} and γ_{ab} , the orthogonality of $\hat{\Omega}_a$ to u^a and n^a , and the definition of the Lie derivative along a vector field ξ^a , we arrive at

$$\begin{aligned} \gamma_a^b \partial_b \left(\frac{\hat{\theta}}{2} + \hat{g} \right) - {}^2\mathbf{D}^b \hat{\sigma}_{ab} + \left[\gamma_{ac} \left(\hat{g} - \frac{\hat{\theta}}{2} \right) - \hat{\sigma}_{ac} \right] u^b \nabla_b u^c + 8\pi \gamma_a^c T_{cd} n^d = \gamma_a^c \mathcal{L}_u \hat{\Omega}_c + \hat{\Omega}_a \mathcal{D}^b u_b \\ + \gamma_a^c \hat{\Omega}^b (\nabla_b u_c - \nabla_c u_b). \end{aligned} \tag{12}$$

Here ${}^2\mathbf{D}_a$ is the 2D (contracted) covariant derivative determined by

$${}^2\mathbf{D}^b \hat{\sigma}_{ab} = \gamma_a^\delta \gamma^{\beta\rho} \nabla_\beta \hat{\sigma}_{\delta\rho}. \tag{13}$$

For the part of eqs. (11) along the time-like direction, after some algebra we get

$$u^b \partial_b \hat{\theta} + \left(\frac{\hat{\theta}}{2} - \hat{g} \right) \mathcal{D}^b u_b + \hat{\sigma}_{ab} \mathcal{D}^b u^a + \mathcal{D}^b \hat{\Omega}_b + \hat{\Omega}_a u^b \nabla_b u^a + 8\pi u^a n^b T_{ab} = 0. \tag{14}$$

To outline the correspondence of eq. (14) to the Raychaudhuri equation, it is convenient to introduce a symmetric tensor

$$\hat{\Theta}_{ab} = \hat{\sigma}_{ab} + \frac{\hat{\theta}}{2} \gamma_{ab}, \tag{15}$$

and to take into account that $\mathcal{D}^b u_b = h_{ab} \mathcal{D}^b u^a = (\gamma_{ab} - u_a u_b) \mathcal{D}^b u^a = \gamma_{ab} \mathcal{D}^b u^a$. Then eq. (14) becomes

$$u^b \partial_b \hat{\theta} - \hat{g} \mathcal{D}^b u_b + \hat{\Theta}_{ab} \mathcal{D}^b u^a + \mathcal{D}^b \hat{\Omega}_b + \hat{\Omega}_a u^b \nabla_b u^a + 8\pi u^a n^b T_{ab} = 0. \tag{16}$$

The so obtained eqs. (12) and (16) turn out to be the Damour-Navier-Stokes and Raychaudhuri equations of 2D relativistic hydrodynamics in the null-hypersurface (horizon) limit. Let us see how it happens.

2.2. The Null-Hypersurface Limit

General analysis of the stretched membrane EMT (9) leads to the conclusion on its divergence on the horizon [4]. Geometrically, this fact is related to the degeneration of the stretched membrane hypersurface to null-hypersurface, that, in particular, means the divergence of time-like and space-like vectors u^a and n^a on the event horizon \mathcal{H} . The Membrane Approach [4] suggests introducing a regularization factor (a function of coordinates) α , which vanishes on the horizon, and whose role is to provide the finiteness of quantities in the null-hypersurface ($\alpha \rightarrow 0$) limit. The choice of this regularization factor is determined by the requirements

$$\lim_{\alpha \rightarrow 0} \alpha u^a = l^a, \quad \lim_{\alpha \rightarrow 0} \alpha n^a = l^a, \quad l^a l_a = 0, \tag{17}$$

where l^a is a null geodesic generator of \mathcal{H} . This null-vector obeys the equation

$$l^b \nabla_b l^a = g_{\mathcal{H}} l^a, \tag{18}$$

which can be treated as a definition of the surface gravity $g_{\mathcal{H}}$.⁵

Now we have to regularize the EMT (9), and to write down eqs. (12) and (16) in terms of the regularized (in the $\alpha \rightarrow 0$ limit) quantities on the horizon. The regularization comes as follows:⁶

$$\hat{\theta} = \alpha^{-1} \theta, \quad \hat{g} = \alpha^{-1} g, \quad \hat{\Theta}_{ab} = \alpha^{-1} \Theta_{ab}, \quad \hat{\sigma}_{ab} = \alpha^{-1} \sigma_{ab}, \quad \hat{\Omega}_a = \Omega_a. \tag{19}$$

Then, in terms of the regular on the horizon variables θ, g, Θ_{ab} and Ω_a , eq. (12) comes into

$$\begin{aligned} \alpha^{-1} \left(\gamma_a^b \partial_b \left(\frac{\theta}{2} + g \right) - {}^2\mathbf{D}^b \sigma_{ab} + \left[\gamma_{ac} \left(g - \frac{\theta}{2} \right) - \sigma_{ac} \right] u^b \nabla_b u^c - \left[\gamma_{ab} \left(\frac{\theta}{2} + g \right) - \sigma_{ab} \right] \partial^b \ln \alpha \right) \\ + 8\pi \gamma_a^c T_{cd} n^d = \gamma_a^c \mathcal{L}_u \Omega_c + \Omega_a \mathcal{D}^b u_b + \gamma_a^c \Omega^b (\nabla_b u_c - \nabla_c u_b). \end{aligned} \tag{20}$$

⁵More on computations of the surface gravity for the Kerr BH can be found in Appendix A.

⁶The scaling in α of different variables depends on their physical interpretation. The Hájíček field [22] $\hat{\Omega}_a$ is a measure of rotation, and it does not depend on a specific spacetime point, though it depends on the chosen frame.

Whereas eq. (16) becomes

$$\alpha^{-1} \left(u^b \partial_b \theta - \text{th } u^b \partial_b \ln \alpha - g^3 \mathcal{D}^b u_b + \Theta_{ab} {}^3 \mathcal{D}^b u^a \right) + {}^3 \mathcal{D}^b \Omega_b + \Omega_a u^b \nabla_b u^a + 8\pi u^a n^b T_{ab} = 0. \quad (21)$$

The next step in completing the task is to take the limit $\alpha \rightarrow 0$. Here we have to use both relations (17) with care, since two operations – taking the limit and acting by derivatives on u^a and n^a – do not commute. And final expressions will be simplified by use of various orthogonality relations.

Consider, for instance, two combinations with the 3D covariant derivative acting on u^a . The first combination, which occurs in both eqs. (20), (21), is ${}^3 \mathcal{D}^b u_b$. In the null-hypersurface limit we get

$$\begin{aligned} \lim_{\alpha \rightarrow 0} {}^3 \mathcal{D}^b u_b &= \lim_{\alpha \rightarrow 0} h^{ab} \nabla_a u_b = \lim_{\alpha \rightarrow 0} (\gamma^{ab} - u^a u^b) \nabla_a u_b = \lim_{\alpha \rightarrow 0} \gamma^{ab} \nabla_a u_b = - \lim_{\alpha \rightarrow 0} u_b \nabla_a \gamma^{ab} \\ &\simeq -\alpha^{-1} l_b \nabla_a \gamma^{ab} = \alpha^{-1} \gamma^{ab} \nabla_a l_b = \alpha^{-1} \theta, \end{aligned} \quad (22)$$

where we have used the orthogonality relations $\gamma^{ab} u_b = 0$ and $\gamma^{ab} l_b = 0$ to rearrange the action of the derivative and to take the limit directly. To arrive at the final answer, we have used the definition of the expansion θ on the horizon, i.e., on the hypersurface, where relations (17) hold: $\theta = \gamma^{ab} \nabla_a l_b$.

The second combination, ${}^3 \mathcal{D}^b u^a$, admits the following representation in the limit:

$$\begin{aligned} \lim_{\alpha \rightarrow 0} {}^3 \mathcal{D}^b u^a &= \lim_{\alpha \rightarrow 0} h^{b\beta} h^{a\alpha} \nabla_\beta u_\alpha = \lim_{\alpha \rightarrow 0} h^{b\beta} \gamma^{a\alpha} \nabla_\beta u_\alpha = - \lim_{\alpha \rightarrow 0} h^{b\beta} u_\alpha \nabla_\beta \gamma^{a\alpha} \\ &\simeq -\alpha^{-1} h^{b\beta} l_\alpha \nabla_\beta \gamma^{a\alpha} = \alpha^{-1} h^{b\beta} \gamma^{a\alpha} \nabla_\beta l_\alpha. \end{aligned} \quad (23)$$

It can be used to write down $\Theta_{ab} {}^3 \mathcal{D}^b u^a$ as $\alpha^{-1} \Theta_{ab} \Theta^{ba}$ on the horizon. Indeed,

$$\lim_{\alpha \rightarrow 0} \Theta_{ab} {}^3 \mathcal{D}^b u^a \simeq \alpha^{-1} \Theta_{ab} h^{b\beta} \gamma^{a\alpha} \nabla_\beta l_\alpha = \alpha^{-1} \Theta_{ab} \gamma^{b\beta} \gamma^{a\alpha} \nabla_\beta l_\alpha = \alpha^{-1} \Theta_{ab} \Theta^{ba}, \quad (24)$$

where we have applied the definition of Θ_{ab} on the horizon: $\Theta_{ab} = \gamma_a^\alpha \gamma_b^\beta \nabla_\alpha l_\beta$. Therefore, at this stage of our consideration, eq. (21) turns into

$$l^b \partial_b \theta - \theta l^b \partial_b \ln \alpha - g\theta + \Theta_{ab} \Theta^{ab} + 8\pi l^a l^b T_{ab} + \lim_{\alpha \rightarrow 0} \alpha^2 \Omega_a u^b \nabla_b u^a = 0. \quad (25)$$

And the non-triviality of the last term on the l.h.s. of (25) strongly depends on the scaling, with respect to the regularization factor α , properties of $\lim_{\alpha \rightarrow 0} u^b \nabla_b u^a$.

Let us consider this expression in more detail. Taking the $\alpha \rightarrow 0$ limit of $v_a \equiv \gamma_a^c u^b \nabla_b u_c$, we get:

$$\lim_{\alpha \rightarrow 0} v_a \equiv \lim_{\alpha \rightarrow 0} \gamma_a^c u^b \nabla_b u_c = - \lim_{\alpha \rightarrow 0} u^b u_c \nabla_b \gamma_a^c \simeq -\alpha^{-2} l^b l_c \nabla_b \gamma_a^c = \alpha^{-2} \gamma_a^c l^b \nabla_b l_c. \quad (26)$$

Were we use eq. (18) as is, the introduced vector v_a would be always equal to zero on the horizon, due to the orthogonality of the null-vector l^a to the induced metric γ_{ab} . However, in the vicinity of the horizon, eq. (18) can be generalized to

$$l^b \nabla_b l^c = g_{\mathcal{H}} l^c + \lambda^c, \quad (27)$$

where λ_c is a vector, which vanishes on the event horizon:

$$\lim_{\alpha \rightarrow 0} \lambda^a = 0. \quad (28)$$

If λ^a vanishes as α^2 (e.g., $\lambda^c = \alpha^2 \gamma^{cd} \xi_d$), then $\lim_{\alpha \rightarrow 0} v_a \neq 0$, so that v_a remains finite on the horizon.⁷ Nevertheless, even with such a generalization, the last term on the l.h.s. of (25) becomes equal to zero.

To take the null-hypersurface limit of eq. (20), one needs to write down the r.h.s. of this equation. Straightforward computations which take into account the orthogonality of Ω_a to l^a , symmetry of Θ_{ab} tensor, and the outcome of eq. (22), result in

$$\lim_{\alpha \rightarrow 0} \left[\gamma_a^c \mathcal{L}_u \Omega_c + \Omega_a {}^3 \mathcal{D}^b u_b + \gamma_a^c \Omega^b (\nabla_b u_c - \nabla_c u_b) \right] \simeq \alpha^{-1} (\mathcal{L}_l \Omega_a + \Omega_a \theta). \quad (29)$$

So that, the null-hypersurface limit of eq. (20) leads to

$$\begin{aligned} \gamma_a^b \partial_b \left(\frac{\theta}{2} + g \right) - {}^2 \mathbf{D}^b \sigma_{ab} + \left[\gamma_{ac} \left(g - \frac{\theta}{2} \right) - \sigma_{ac} \right] v^c - \left[\gamma_{ab} \left(\frac{\theta}{2} + g \right) - \sigma_{ab} \right] \partial^b \ln \alpha \\ + 8\pi \gamma_a^c T_{cd} l^d = \gamma_a^c \mathcal{L}_l \Omega_c + \Omega_a \theta. \end{aligned} \quad (30)$$

⁷In Section 3 we justify the finiteness of v_a in the horizon limit for the Kerr BH solution by direct computations.

Summing up, in the null-hypersurface limit the projected Gauss-Codazzi equations (12) and (16) are rearranged into

$$l^b \partial_b \theta - g\theta + \Theta_{ab} \Theta^{ab} + 8\pi l^a l^b T_{ab} = \theta l^b \partial_b \ln \alpha, \tag{31}$$

and

$$\begin{aligned} & \gamma_a^b \partial_b \left(\frac{\theta}{2} + g \right) - {}^2\mathbf{D}^b \sigma_{ab} + 8\pi \gamma_a^c T_{cd} l^d - \gamma_a^c \mathcal{L}_l \Omega_c - \Omega_a \theta \\ & = \left[\gamma_{ab} \left(\frac{\theta}{2} + g \right) - \sigma_{ab} \right] \partial^b \ln \alpha - \left[\gamma_{ac} \left(g - \frac{\theta}{2} \right) - \sigma_{ac} \right] v^c. \end{aligned} \tag{32}$$

These equations coincide (cf., e.g., Ref. [15, 16]) with the Raychaudhuri and the Damour-Navier-Stokes (RDNS) equations, if the following conditions are satisfied:

$$\left[\gamma_{ac} \left(g - \frac{\theta}{2} \right) - \sigma_{ac} \right] v^c = \left[\gamma_{ab} \left(\frac{\theta}{2} + g \right) - \sigma_{ab} \right] \partial^b \ln \alpha, \quad l^b \partial_b \ln \alpha = 0. \tag{33}$$

Since these conditions contain the potentially divergent on the horizon parts, while the proposed regularization procedure of [4] was oriented toward making the quantities finite on the horizon, we arrive at the apparent contradiction. Therefore, we have to verify the fulfillment of these consistency conditions on a specific spacetime geometry. We will use two exact solutions to the Einstein equations – the Schwarzschild and the Kerr black holes – to this end.

3. EXPLORING THE RDNS-TYPE EQUATIONS OF THE NULL-HYPERSURFACE LIMIT

3.1. The Schwarzschild solution

We get started with a warm-up exercise of the Schwarzschild solution, on the example of which we will establish/discuss: (i) the origin of different choices in the 1+1+2 metric decomposition within the Membrane Approach of [4]; (ii) triviality of the consistency conditions (33) for the Schwarzschild BH solution; (iii) the relation between the null-hypersurface limit of the Membrane Approach and the null-hypersurface description of [15, 16].

To achieve our goals, we will use the Eddington-Finkelstein coordinates (v, r, θ, φ) , which are related to the original coordinates of the standard Schwarzschild metric $(t_S, r, \theta, \varphi)$ as⁸

$$v = t_S + r^* = t_S + r + 2M \ln \left| \frac{r}{2M} - 1 \right|. \tag{34}$$

The “tortoise” coordinate r^* is the solution to the connection equation

$$dr^* = \frac{dr}{f(r)}, \quad f(r) = 1 - \frac{2M}{r}, \tag{35}$$

and the Schwarzschild metric in the Eddington-Finkelstein coordinates becomes

$$ds^2 = -f(r)dv^2 + 2dvdr + r^2(d\theta^2 + \sin^2 \theta d\varphi^2). \tag{36}$$

To proceed further, we introduce a new time-like coordinate $t = v - r$, in terms of which the interval (36) turns into

$$ds^2 = - \left(1 - \frac{2M}{r} \right) dt^2 + \frac{4M}{r} dt dr + \left(1 + \frac{2M}{r} \right) dr^2 + r^2(d\theta^2 + \sin^2 \theta d\varphi^2). \tag{37}$$

Now, let’s present the encoded in (37) metric as $g_{ab} = -u_a u_b + n_a n_b + \gamma_{ab}$. The structure of (37) suggests two possible alternatives to this end:

- First, we can choose

$$u_a = \left(-\sqrt{1 - \frac{2M}{r}}, \frac{2M}{r\sqrt{1 - \frac{2M}{r}}}, 0, 0 \right), \quad n_a = \left(0, \frac{1}{\sqrt{1 - \frac{2M}{r}}}, 0, 0 \right), \quad -u^a u_a = n^a n_a = 1, \tag{38}$$

$$\gamma_{ab} = \begin{pmatrix} 0 & 0 & 0 & 0 \\ 0 & 0 & 0 & 0 \\ 0 & 0 & r^2 & 0 \\ 0 & 0 & 0 & r^2 \sin^2 \theta \end{pmatrix}. \tag{39}$$

This choice corresponds to forming the perfect square from the 1st and the 2nd term on the r.h.s. of (37).

⁸We set $G = c = 1$.

- Second, we can present the metric as $g_{ab} = -\tilde{u}_a\tilde{u}_b dx^a dx^b + \tilde{n}_a\tilde{n}_b dx^a dx^b + \gamma_{ab} dx^a dx^b$ with vectors

$$\tilde{u}_a = \left(-\frac{1}{\sqrt{1 + \frac{2M}{r}}}, 0, 0, 0 \right), \quad \tilde{n}_a = \left(\frac{2M}{r} \frac{1}{\sqrt{1 + \frac{2M}{r}}}, \sqrt{1 + \frac{2M}{r}}, 0, 0 \right), \quad -\tilde{u}^a\tilde{u}_a = \tilde{n}^a\tilde{n}_a = 1, \quad (40)$$

and the same angle part γ_{ab} as before. This presentation of the metric follows from forming the perfect square out of the 2nd and the 3rd term on the r.h.s. of eq. (37).

These two representations of the same metric are not unrelated to each other since the vectors are related by Lorentz transformations in the plane transversal to the angular coordinates:

$$\tilde{u}_a = \Lambda_a^b u_b, \quad \tilde{n}_a = \Lambda_a^b n_b; \quad \Lambda\Lambda^T = 1. \quad (41)$$

Eqs. (17), crucial for the Membrane Approach, hold for the regularization factor⁹ $\alpha = \sqrt{f(r)}$, and time/space-like vectors (38):

$$\lim_{\alpha \rightarrow 0} \alpha u^a = l^a, \quad \lim_{\alpha \rightarrow 0} \alpha n^a = l^a, \quad l^a = (1, 0, 0, 0). \quad (42)$$

The vector l^a is a null-vector on the horizon (i.e., at $f(r) = 0$).¹⁰ As one can see, the regularization factor depends only on the radial coordinate. Therefore, the consistency conditions (33) are trivially satisfied, so that for the Schwarzschild geometry the RDNS-type equations (31), (32) coincide with that of originally derived in [3,4] and [18].

Now, let us briefly discuss the correspondence of the Membrane Approach to the null-hypersurface description of [15, 16]. To define a time-like hypersurface, one can specify two null-vectors transversal/longitudinal to it. These null-vectors are constructed out of linear combinations of \tilde{u}^a and \tilde{n}^a (see [16]),

$$l^a = N(\tilde{u}^a + \tilde{n}^a), \quad k^a = \frac{1}{2N}(\tilde{u}^a - \tilde{n}^a), \quad (43)$$

$$\tilde{u}^a = \left(\sqrt{1 + \frac{2M}{r}}, -\frac{2M}{r} \frac{1}{\sqrt{1 + \frac{2M}{r}}}, 0, 0 \right), \quad \tilde{n}^a = \left(0, \frac{1}{\sqrt{1 + \frac{2M}{r}}}, 0, 0 \right),$$

with a lapse function N . To equate l^a of (43) to $l^a = (1, 0, 0, 0)$ on the event horizon $r_{\mathcal{H}} = 2M$, one fixes $N = 1/\sqrt{1 + 2M/r}$. Then, after recovering the exact form of the second null-vector k^a , it is easy to verify that $l^2 = 0, k^2 = 0$ and $l^a k_a = -1$ everywhere.

Apparently, the same consideration is applicable to u^a and n^a vectors

$$u^a = \left(\frac{1}{\sqrt{1 - \frac{2M}{r}}}, 0, 0, 0 \right), \quad n^a = \left(\frac{2M}{r\sqrt{1 - \frac{2M}{r}}}, \sqrt{1 - \frac{2M}{r}}, 0, 0 \right), \quad (44)$$

which are the contravariant counterpart of (38). In this case, the lapse function N is given by $N = \sqrt{(1 - 2M/r)/(1 + 2M/r)}$. Therefore, following [15, 16], one may recover the corresponding null-vectors for any reasonable form of 1+1+2 metric decomposition. However, to describe a null-hypersurface the same conditions must be met as in eqs. (42).

To sum up, different rearrangements of the diagonal and non-diagonal terms in the non-angular part of metric (37) lead to different forms of its 1+1+2 decomposition. Just one of them falls into the criteria of the null-hypersurface description, and can be used in computing characteristics of the dual, to the stretched membrane near the BH horizon, fluid. There are various approaches to reach this goal, examples of which are that of [4] and [15, 16]. They are slightly different in details, but comparing them to each other¹¹ we draw the conclusion that they lead to the same outcomes.

Unfortunately, the Schwarzschild solution is plain to reveal all sides of the RDNS equations extension. It can be done in the analysis of a more complicated example, like the Kerr BH solution, to the consideration of which we now turn.

3.2. The Kerr Black Hole

The Kerr metric in the Eddington-Finkelstein coordinates (v, r, θ, φ) is given by

$$ds^2 = -\left(1 - \frac{2Mr}{\rho^2}\right) dv^2 + 2dvdr - 2a \sin^2 \theta d\varphi dr - \frac{4aMr}{\rho^2} \sin^2 \theta dv d\varphi + \rho^2 d\theta^2 + \left(r^2 + a^2 + \frac{2Mr}{\rho^2} a^2 \sin^2 \theta\right) \sin^2 \theta d\varphi^2, \quad \rho^2 = r^2 + a^2 \cos^2 \theta. \quad (45)$$

⁹More on the choice of α can be found, e.g., in [4, 13].

¹⁰Outside (in the vicinity of) the horizon, l^a becomes either a time-like vector, if it is associated with u^a , or a space-like one, if it is associated with n^a .

¹¹We refer the reader for two Appendices B and C, where we establish the equivalence between the generalized DNS equations near the event horizon of this paper and of Ref. [15], and re-derive the established here consistency conditions from the construction of [15, 16].

As in the Schwarzschild BH case, we introduce the time coordinate $t = v - r$, so that, in terms of (t, r, θ, φ) ,

$$ds^2 = -\left(1 - \frac{2Mr}{\rho^2}\right) dt^2 + \frac{4Mr}{\rho^2} dt dr - \frac{4aMr}{\rho^2} \sin^2 \theta dt d\varphi + \left(1 + \frac{2Mr}{\rho^2}\right) dr^2 - 2a \sin^2 \theta \left(1 + \frac{2Mr}{\rho^2}\right) dr d\varphi + \rho^2 d\theta^2 + \left(r^2 + a^2 + \frac{2Mr}{\rho^2} a^2 \sin^2 \theta\right) \sin^2 \theta d\varphi^2. \tag{46}$$

The metric (46) contains three cross-terms, that apparently complicates the 1 + 1 + 2 decomposition. Its inverse contains merely two cross-terms,

$$d\bar{s}^2 \equiv g^{ab} \partial_a \partial_b = -\left(1 + \frac{2Mr}{\rho^2}\right) \partial_t^2 + \frac{4Mr}{\rho^2} \partial_t \partial_r + \frac{\Delta}{\rho^2} \partial_r^2 + \frac{2a}{\rho^2} \partial_r \partial_\varphi + \frac{1}{\rho^2} \partial_\theta^2 + \frac{1}{\rho^2 \sin^2 \theta} \partial_\varphi^2, \tag{47}$$

that slightly simplifies the computations. In writing the inverse metric we have used the dual basis notation

$$dx^b \partial_a = \delta_a^b. \tag{48}$$

Δ is the standard for the Kerr solution function of the radial direction,

$$\Delta = r^2 + a^2 - 2Mr, \tag{49}$$

used for determining the radial locations $(r_{\mathcal{H}}^\pm)$ of the black hole horizons: $\Delta(r_{\mathcal{H}}^\pm) = 0$.

As in the case of the Schwarzschild spacetime, there are two possible rearrangements of the inverse Kerr metric (47) as $g^{ab} = -u^a u^b + n^a n^b + \gamma^{ab}$ suggested by its structure:

- i) The first option refers to forming the perfect square from the 1st and the 2nd terms on the r.h.s. of (47) at the first step, and going along this line further on.
- ii) The second option supposes combining the 2nd and the 3rd terms on the r.h.s. of (47) at the first stage, with developing this line after.¹²

However, within the Membrane Approach, we have to choose the way, along which we will be able to produce eqs. (17) with the appropriately chosen α . Thus, we have to determine the null-vector l^a for the Kerr geometry first.

According to the Kerr metric structure, there are two associated Killing vectors (in t and φ directions), that specifies non-trivial components of the null-vector l^a :

$$l^a = (l^t, 0, 0, l^\varphi) = (1, 0, 0, X). \tag{50}$$

The function X is fixed from the null-vector condition, $l^a l_a = 0$. For the metric (46), the null-vector condition leads to

$$X = \frac{2aMr}{A} \pm \frac{\rho \sin \theta}{A} \sqrt{(A - (2Mr)^2) - 2Mr\Delta}, \tag{51}$$

where we have introduced

$$A = \rho^2(r^2 + a^2) + 2a^2 Mr \sin^2 \theta = (\rho^2 + 2Mr)\Delta + (2Mr)^2. \tag{52}$$

On the horizon, where $\Delta = 0$ and $A = (2Mr_{\mathcal{H}})^2$, eq. (51) turns into $X = a/(2Mr_{\mathcal{H}})$; hence¹³

$$l^a = \left(1, 0, 0, \frac{a}{2Mr_{\mathcal{H}}}\right). \tag{53}$$

It is easy to check that the metric decomposition “i)” does not lead to $\lim_{\alpha \rightarrow 0} \alpha u^a = \lim_{\alpha \rightarrow 0} \alpha n^a = l^a$, required in the Membrane Approach, whatever the α factor would be. For this reason, we have to turn to the option “ii)”. Rearranging the metric (47) in this way, we arrive at

$$d\bar{s}^2 = \frac{1}{\rho^2} \left[-\left(\sqrt{\frac{A}{\Delta}} \partial_t + \frac{2Mra}{\sqrt{A\Delta}} \partial_\varphi\right)^2 + \left(\frac{2Mr}{\sqrt{\Delta}} \partial_t + \sqrt{\Delta} \partial_r + \frac{a}{\sqrt{\Delta}} \partial_\varphi\right)^2 + \partial_\theta^2 + \frac{\rho^4}{A \sin^2 \theta} \partial_\varphi^2 \right]. \tag{54}$$

Now, for getting $g^{ab} = -u^a u^b + n^a n^b + \gamma^{ab}$, with Δ of (49) and A of (52), we take

$$u^a = \Delta^{-1/2} \left(\frac{\sqrt{A}}{\rho}, 0, 0, \frac{2Mra}{\rho\sqrt{A}}\right), \quad n^a = \Delta^{-1/2} \left(\frac{2Mr}{\rho}, \frac{\Delta}{\rho}, 0, \frac{a}{\rho}\right), \tag{55}$$

¹²In the Schwarzschild (i.e., zero-rotation) limit, the option “i)” corresponds to \tilde{u}^a and \tilde{n}^a of (43), while the option “ii)” leads to (44).

¹³Note that here we consider the external part of the Kerr spacetime. Therefore, $r_{\mathcal{H}} = M + \sqrt{M^2 - a^2}$ is the outer horizon (the largest root of $\Delta(r) = 0$ algebraic equation).

$$\gamma^{ab} = \begin{pmatrix} 0 & 0 & 0 & 0 \\ 0 & 0 & 0 & 0 \\ 0 & 0 & \rho^{-2} & 0 \\ 0 & 0 & 0 & \frac{\rho^2}{A \sin^2 \theta} \end{pmatrix}. \tag{56}$$

And, to equate (53) and (55) in the null-hypersurface limit, the regularization function has to be

$$\alpha = \rho \sqrt{\frac{\Delta}{A}}. \tag{57}$$

Having fixed all the needed ingredients, we can compute the energy-momentum tensor \hat{t}^{ab} (cf. eqs. (2), (3), (5) and (9)):

$$\hat{t}^{ab} = \frac{1}{\Delta^{1/2} \rho^3(r, \theta)} \begin{pmatrix} -(r-M)a^2 \cos^2 \theta - a^2(M+r) - 2r^3 & 0 & 0 & -aM \\ 0 & 0 & 0 & 0 \\ 0 & 0 & r-M & 0 \\ -aM & 0 & 0 & \frac{r-M}{\sin^2 \theta} \end{pmatrix}. \tag{58}$$

After that, taking into account eqs. (55), (56), and (10), we get

$$\begin{aligned} \hat{\theta} &= \frac{\Delta^{1/2}}{A\rho} h(r, \theta), \quad h(r, \theta) = 2r^3 + a^2(r+M) + (r-M)a^2 \cos^2 \theta; \\ \hat{\Omega}^a &= \left(0, 0, 0, \frac{aM}{\rho^2 A^{3/2}} \omega(r, \theta) \right), \quad \omega(r, \theta) = a^2(a^2 - r^2) \cos^2 \theta - 3r^4 - a^2 r^2; \\ \hat{g} &= \frac{M}{\Delta^{1/2} \rho^3 A} \left((r^2 + a^2)^2 (r^2 - a^2 \cos^2 \theta) - 4a^2 M r^3 \sin^2 \theta \right); \\ \hat{\sigma}^{ab} &= \text{diag} \left(0, 0, \frac{\Delta^{1/2}}{\rho^3} \left(\frac{r}{\rho^2} - \frac{h(r, \theta)}{2A} \right), \frac{\Delta^{1/2} a^2}{2\rho A^2} \left(a^2(M-r) \cos^2 \theta - r^2(3M+r) \right) \right). \end{aligned} \tag{59}$$

Recall, Δ , A and ρ have been introduced in (45), (49) and (52). The tensor $\hat{\Theta}_{ab}$, introduced in (15), then becomes

$$\hat{\Theta}^{ab} = \text{diag} \left(0, 0, \frac{\Delta^{1/2} r}{\rho^5}, \frac{\Delta^{1/2}}{\rho \sin^2 \theta} \frac{\rho^2 h(r, \theta) - Ar}{A^2} \right). \tag{60}$$

A brief inspection of (59) and (60) leads to the conclusion that the only \hat{g} turns out to be singular on the horizon. After the regularization, $g = \alpha \hat{g}$ becomes

$$g = \frac{M}{\rho^2 A^{3/2}} \left((r^2 + a^2)^2 (r^2 - a^2 \cos^2 \theta) - 4a^2 M r^3 \sin^2 \theta \right), \tag{61}$$

and, in the null-hypersurface limit, it coincides with the surface gravity on the horizon:

$$\lim_{\alpha \rightarrow 0} g = g_{\mathcal{H}}, \quad g_{\mathcal{H}} = \frac{\sqrt{M^2 - a^2}}{2M(M + \sqrt{M^2 - a^2})}. \tag{62}$$

The other non-trivial quantity on the horizon is the vector field $\hat{\Omega}_a$, which, according to (19), does not need to be regularized: $\hat{\Omega}_a = \Omega_a$.

To figure out the form of the RDNS-type equations in the case, we have to verify the consistency conditions (33). For the null-vector l^a (see eq. (53)) and the regularization function α (see eq. (57)), the second condition of (33) is satisfied. Verifying the first condition of (33), one needs the exact form of the projected acceleration vector $v_a = \gamma_a^c u^b \nabla_b u_c$, a direct computation of which results in

$$v_a = \left(0, 0, -\frac{2a^2 M r (r^2 + a^2) \cos \theta \sin \theta}{\rho^2 A}, 0 \right). \tag{63}$$

According to (63), v_a is finite on the horizon, that has been assumed upon the derivation of the consistency conditions (33). Straightforward computations show that, with v_a from (63) and α from (57), the first of the conditions (33) is also satisfied.

Thus, as in the Schwarzschild case, the Kerr BH geometry keeps the standard form (cf., e.g., [16]) of the Raychaudhuri and the Damour equations of a (1+2) null-hypersurface. (I.e., eqs. (31) and (32) have trivial right hand sides in the case.)

We end up this section with recalling how the l.h.s. of the Damour equation (32) is related to the Navier-Stokes equation for a viscous fluid [3]. Let us introduce a force surface density $f_a = -\gamma_a^c T_{cd} l^d$, the momentum density π_a , the pressure p , the shear and bulk viscosities η and ζ of the fluid as

$$\pi_a = -\frac{1}{8\pi}\Omega_a, \quad p = \frac{g}{8\pi}, \quad \eta = \frac{1}{16\pi}, \quad \zeta = -\frac{1}{16\pi}. \quad (64)$$

Then, the l.h.s. of (32) can be presented in the form of the Navier-Stokes equation

$$\gamma_a^c \mathcal{L}_l \pi_c + \theta \pi_a = -{}^2\mathbf{D}_a p + 2\eta {}^2\mathbf{D}^b \sigma_{ba} + \zeta {}^2\mathbf{D}_a \theta + f_a. \quad (65)$$

The correspondence of the momentum density π^a to the Hájiček field $\Omega^a = \hat{\Omega}^a$ makes the former finite on the horizon. (Cf. eqs. (59)). Comparing this result with the early obtained divergence of π^a on the horizon of the Kerr BH in the Boyer-Lindquist coordinates [13], we conclude on the frame dependence of the momentum density: the correct choice of coordinates makes the quantity finite on the horizon.

4. CONCLUSIONS

Let us summarize our findings. At the first stage of our studies, following the Parikh-Wilczek Membrane Approach to black holes, we have presented the Gauss-Codazzi equations on the horizon as hydrodynamic-type equations. We expected to derive the standard Raychaudhuri and the Damour-Navier-Stokes (RDNS) equations of a viscous fluid in this way. However, our actual result looks slightly different: the final equations are extensions of the RDNS equations. Specifically, there appears new terms, containing derivatives of a function of the regularization parameter. Recall, this parameter is used for making the energy-momentum tensor of a stretched membrane finite on the horizon. The explicit form of this function – the logarithm in the case of the standard regularization within the Membrane Approach – depends on the way of regularization. Anyway, the established new terms can not be ignored in the null-hypersurface limit, upon building the bridge between geometry (the Gauss-Codazzi equations) and dynamics (the RDNS equations). Getting the “classical” RDNS equations back two non-trivial conditions must be met. And the fulfillment of these consistency conditions requires the tight coordination of different elements (metric, null-vectors, projected acceleration vector, regularization function) of the chosen space-time geometry.

To investigate this issue in more detail, we have examined two notable examples of exact solutions to the Einstein equations: the Schwarzschild and the Kerr black holes. The case of the Schwarzschild solution has been considered as a warm-up exercise, aimed at establishing the machinery, which could be further applied to the Kerr solution in the Eddington-Finkelstein parametrization. In view of simplicity of the Schwarzschild solution, the mentioned consistency conditions are trivially satisfied. The established consistency conditions have been verified, to the full extent, in the case of the Kerr metric in the Eddington-Finkelstein parametrization. The verification requires more technical efforts, due to a complicated structure of the metric tensor, but we arrive at the conclusion on the fulfillment of the consistency conditions in this case. Therefore, for the Schwarzschild and the Kerr solutions, the RDNS equations of the Membrane Approach do not change. We can expect the same effect for exact BH solutions to the Einstein equations with the required tight coordination of the spacetime geometry components which results in the non-expanding (isolated) horizon [23–26], and, consequently, in the classical form of the RDNS equations on the horizon. As we have mentioned in Introduction, the ground for such expectations is based on the ideology of the Membrane Approach to regularize the divergent on the horizon quantities, and to construct in this way the effective dynamical description of the horizon hypersurface in terms of the finite variables.

In the course of our studies we paid a special attention to the relation of the Membrane Approach [4] to theourgoulhon-Jaramillo [15, 16] method of a null-hypersurface description. Note that within the approach of [15, 16] it was obtained the generalization of the Damour-Navier-Stokes (DNS) equation in the vicinity of the event horizon of a BH-type solution to the Einstein equations. However, in the null-hypersurface limit, the authors of [15, 16] drew the conclusion that on the horizon the generalized DNS equation is reduced to its classical form. This fact motivates us to investigate the correspondence between the Membrane Approach used in the paper and the approach of [15, 16] in more detail. In two added Appendices we establish the equivalence of the DNS equation generalizations near the horizon in the approaches of [4] and [15, 16] for the specific metric parametrization used byourgoulhon and Jaramillo. (This parametrization supposes the trivial vorticity tensor of a geodesic congruence.) Also, the detailed consideration of the null-hypersurface limit within the approach of [15, 16] leads to the same set of the consistency conditions as in the Membrane Approach. It turns out that both consistency conditions follow from the generalized DNS equation without the need to consider an additional equation like the Raychaudhuri equation. This emphasizes the self-consistency of the Einstein equations, from which the RDNS equations follow. And again, the main condition to keep the classical form of the DNS equations on the horizon is the requirement of having the non-expanding horizon.

Since the non-expanding/isolated horizon is common for exact BH solutions [23–26], a more interesting situation arises for non-exact solutions of the BH type, like, for instance, slowly rotating BHs, metrics mimicking black holes, post-Newtonian corrected BHs etc., examples of which can be found in [27–33]. If these approximations of the spacetime metric are used in the construction of the relativistic hydrodynamics within the Membrane Approach, the established

consistency conditions should hold for them as well, to the same order of the approximation as for the Einstein equations. (Cf. footnote 5 in this respect.) So that, the established here consistency conditions can be served as an additional tool in verifying the viability of such approximations. It would be interesting to find examples of metrics where the consistency conditions fails, and to analyze reasons for that. We hope to report on this and other results of our studies in future publications.

Acknowledgments

AJN is thankful to Prof. O.B. Zaslavskii for correspondence and viable comments. The work of A.J.N. is supported in part within the Cambridge-NRFU 2022 initiative "Individual research (developments) grants for researchers in Ukraine (supported by the University of Cambridge, UK)", project №2022.02/0052.

Conflicts of interest

The authors declare no conflict of interest.

A. THE SURFACE GRAVITY FOR THE KERR SOLUTION

Let us consider the surface gravity calculation for a rotating BH in more detail.

There are several ways to compute the surface gravity. One may use, for instance, eq. (18). Another way is to take into account the fact that the null-vector l^a (53) is nothing but the Killing vector of the Kerr BH metric, $\xi^a = \partial_t + \Omega \partial_\varphi$, on the horizon. Ω is the angular velocity, defined by

$$\Omega \equiv \frac{d\varphi}{dt} = \frac{d\varphi/ds}{dt/ds} = \frac{u^\varphi}{u^t} = \frac{2Mr a}{A}, \quad (\text{A.1})$$

where we have used the components of u^a from (55). Note, preliminarily, that (A.1) points to the following details:

- i) the vector u^a is the velocity of the so-called *stationary* observer, which possesses arbitrary, but uniform, angular velocity Ω ;
- ii) this angular velocity coincides with the ZAMO (zero angular momentum observer) angular velocity, defined by $\hat{L} \equiv u_\varphi \xi^\varphi = 0$. For metric (46), the zero angular momentum is realized as $u_\varphi = u^t g_{t\varphi} + u^\varphi g_{\varphi\varphi} = 0$. Hence,

$$\omega \equiv \frac{u^\varphi}{u^t} = -\frac{g_{t\varphi}}{g_{\varphi\varphi}}. \quad (\text{A.2})$$

With metric (46),

$$\omega = \frac{2aMr}{A}, \quad (\text{A.3})$$

that is the same as Ω of (A.1). Therefore, the 4-velocity u^a from (55) is that of a ZAMO;

- iii) the angular velocity Ω coincides with the angular velocity of the black hole on the black hole horizon

$$\Omega_{\mathcal{H}} \equiv \omega(r_{\mathcal{H}}) = \frac{a}{2Mr_{\mathcal{H}}} \equiv \frac{a}{r_{\mathcal{H}}^2 + a^2}. \quad (\text{A.4})$$

By use of the Killing vector nature of ξ^a , one may easy verify the relation

$$\nabla_a (\xi^b \xi_b) = -2g_{\mathcal{H}} \xi_a, \quad \xi^a = \partial_t + \Omega_{\mathcal{H}} \partial_\varphi, \quad (\text{A.5})$$

which we will use in computations of the surface gravity $g_{\mathcal{H}}$.

The norm of ξ^a for the Kerr metric in the Eddington-Finkelstein coordinates is given by

$$\xi^a \xi_a = \frac{A \sin^2 \theta}{\rho^2} (\Omega_{\mathcal{H}} - \omega)^2 - \frac{\rho^2 \Delta}{A}. \quad (\text{A.6})$$

Then the covariant derivative of $\xi^a \xi_a$ on the horizon, where $\Omega_{\mathcal{H}} = \omega(r_{\mathcal{H}})$, is equal to

$$\nabla_a (\xi^b \xi_b) = -\frac{\rho^2}{A} \Big|_{\mathcal{H}} \partial_a \Delta. \quad (\text{A.7})$$

Or, with $\Delta = r^2 + a^2 - 2Mr$, eq. (A.7) becomes

$$\nabla_a (\xi^b \xi_b) = -\frac{2\rho^2}{A} (r - M) \Big|_{\mathcal{H}} \partial_a r. \quad (\text{A.8})$$

Now, we compare the r.h.s. of (A.8) with ξ_a , and take both quantities on the horizon. We get

$$\xi_a \Big|_{\mathcal{H}} = \lim_{\alpha \rightarrow 0} \alpha u_a \Big|_{\mathcal{H}} = \left(0, \frac{2Mr\rho^2}{A} \Big|_{\mathcal{H}}, 0, 0 \right), \tag{A.9}$$

so that, combining (A.5), (A.7) and (A.9), and taking all of these quantities on the horizon, we arrive at

$$\frac{2\rho^2}{A} (r - M) \Big|_{\mathcal{H}} = g_{\mathcal{H}} \frac{2Mr\rho^2}{A} \Big|_{\mathcal{H}}.$$

Therefore,

$$g_{\mathcal{H}} = \frac{r_{\mathcal{H}} - M}{2Mr_{\mathcal{H}}}. \tag{A.10}$$

Since $r_{\mathcal{H}} = M + \sqrt{M^2 - a^2}$, we recover eq. (62). Equivalently, the surface gravity can be presented as

$$g_{\mathcal{H}} = \frac{r_+ - r_-}{2(r_+^2 + a^2)}, \quad r_{\pm} = M \pm \sqrt{M^2 - a^2}. \tag{A.11}$$

B. ON THE GOURGOULHON'S GENERALIZATION OF THE DNS EQUATION

In this Appendix we provide the link between the RDNS equations (31), (32) and the generalization of the DNS equation in the vicinity of a BH horizon, derived in Ref. [15].

Let's start with an overview of basics in the construction of [15]. Suppose we are dealing with a hypersurface $\tilde{\mathcal{H}}$, which is foliated by a family of 2D space-like surfaces. The orthogonal to these 2d surfaces plane can be generated by basic vectors (\mathbf{h}, \mathbf{m}) , one of which (say, the vector \mathbf{h}) is inside of $\tilde{\mathcal{H}}$, and the other one is orthogonal to $\tilde{\mathcal{H}}$. We refer the reader to Ref. [15] for more details on the basic vectors (\mathbf{h}, \mathbf{m}) . For our purposes it would be enough to use the representation of these vectors in terms of null vectors (\mathbf{l}, \mathbf{k}) on the whole 4D space-time:

$$h^a = l^a - Ck^a, \quad m^a = l^a + Ck^a. \tag{B.1}$$

From the properties of (\mathbf{l}, \mathbf{k}) , $l^2 = 0$, $k^2 = 0$ and $l^a k_a = -1$ it follows that

$$C = \frac{1}{2} h^a h_a = -\frac{1}{2} m^a m_a. \tag{B.2}$$

Since we are interested in a time-like hypersurface $\tilde{\mathcal{H}}$, $C < 0$.

In [15] it was established the following generalization of the DNS equation on the hypersurface $\tilde{\mathcal{H}}$:

$$q_a^c \mathcal{L}_h \Omega_c^{(1)} + \theta^{(h)} \Omega_a^{(1)} = {}^2 D_a \langle \kappa^{(1)}, \mathbf{h} \rangle - {}^2 D^b \sigma_{ba}^{(m)} + \frac{1}{2} {}^2 D_a \theta^{(m)} - \theta^{(k)} {}^2 D_a C + 8\pi q_a^c T_{cd} m^d, \tag{B.3}$$

where q_{ab} is the 2D induced metric on the space-like foliation of $\tilde{\mathcal{H}}$. In (B.3) \mathcal{L}_h defines the Lie derivative along the vector h^a ; ${}^2 D_a$ is the covariant, w.r.t. the 2D induced metric q_{ab} , derivative; T_{ab} denotes the EMT of matter fields. For the rest of quantities and symbols entering eq. (B.3) we use the notation of [15]. For instance, the ‘‘surface gravity’’ 1-form is determined in [15] as

$$\kappa_a^{(1)} = - \left(\delta_a^b - q_a^b \right) k_c \nabla_b l^c. \tag{B.4}$$

The definitions of the remaining quantities and operations will be given as needed when comparing equation (B.3) with the obtained in the main text equation (32).

To restate eq. (B.3) as eq. (32), we will introduce the orthonormal basis, related to the vectors (\mathbf{h}, \mathbf{m}) :

$$h^a = \lambda \hat{u}^a, \quad m^a = \lambda \hat{n}^a, \quad \lambda^2 = -2C. \tag{B.5}$$

Apparently,

$$\hat{u}^a \hat{u}_a = -1, \quad \hat{n}^a \hat{n}_a = 1, \quad \hat{u}^a \hat{n}_a = 0. \tag{B.6}$$

Then, in terms of \hat{u}^a and \hat{n}^a , the null-vectors (\mathbf{l}, \mathbf{k}) become

$$l^a = \frac{\lambda}{2} (\hat{u}^a + \hat{n}^a), \quad k^a = \frac{1}{\lambda} (\hat{u}^a - \hat{n}^a), \tag{B.7}$$

so that

$$\hat{u}^a = \frac{1}{\lambda} l^a + \frac{\lambda}{2} k^a, \quad \hat{n}^a = \frac{1}{\lambda} l^a - \frac{\lambda}{2} k^a. \tag{B.8}$$

Now, we have to write down eq. (B.3) in the basis of (\mathbf{u}, \mathbf{n}) . For $\Omega_a^{(1)}$ (see eq. (3.21) in Ref. [15]) we get

$$\Omega_a^{(1)} \equiv \frac{1}{k^e l_e} q_a^b k_c \nabla_b l^c = q_a^b \lambda^{-1} \partial_b \lambda - \Omega_a^{(\hat{\mathbf{n}})}, \tag{B.9}$$

where $\Omega_a^{(\hat{\mathbf{n}})}$ has the same structure as $\Omega_a^{(1)}$ with $\mathbf{l} \rightarrow \hat{\mathbf{n}}$ replacement. Getting eq. (B.9), we have used the identities $\hat{u}_a \nabla_b \hat{u}^a = \hat{n}_a \nabla_b \hat{n}^a = 0$ and $\hat{u}_a \nabla_b \hat{n}^a = -\hat{n}_a \nabla_b \hat{u}^a$. The first on the r.h.s. of (B.9) term is equal, on the hypersurface \mathcal{H} , to $\hat{v}_a \equiv q_a^c \hat{u}^b \nabla_b \hat{u}_c$, so that $\Omega_a^{(1)} = \hat{v}_a - \Omega_a^{(\hat{\mathbf{n}})}$. (It directly follows from eq. (B.8), and eqs. (4.22), (4.24), (4.25), (4.28) and (4.29) of Ref. [15].) Therefore, with such an identification, the first term on the l.h.s. of (B.3) becomes

$$q_a^c \mathcal{L}_h \Omega_c^{(1)} = q_a^c \mathcal{L}_h (\hat{v}_c - \Omega_c^{(\hat{\mathbf{n}})}) = q_a^c \mathcal{L}_h \hat{v}_c - q_a^c \mathcal{L}_h \Omega_c^{(\hat{\mathbf{n}})} = \lambda \left[q_a^c \mathcal{L}_{\hat{\mathbf{u}}} \hat{v}_c - q_a^c \mathcal{L}_{\hat{\mathbf{u}}} \Omega_c^{(\hat{\mathbf{n}})} \right]. \tag{B.10}$$

The second term on the l.h.s. of (B.3) is

$$\theta^{(\mathbf{h})} \Omega_a^{(1)} \equiv q^{ab} \nabla_a h_b (\hat{v}_a - \Omega_a^{(\hat{\mathbf{n}})}) = \left| h_b = \lambda \hat{u}_b \right| = \lambda \theta^{(\hat{\mathbf{u}})} (\hat{v}_a - \Omega_a^{(\hat{\mathbf{n}})}). \tag{B.11}$$

Here we have used $q^{ab} \hat{u}_b = 0$ and the following definition for $\theta^{(\mathbf{h})} = q^{ab} \nabla_a h_b$ and $\theta^{(\hat{\mathbf{u}})} \equiv \theta^{(\mathbf{h} \rightarrow \hat{\mathbf{u}})}$.

Let's turn to the r.h.s. of eq. (B.3). In the first term on the r.h.s. we meet the scalar product of vectors $\kappa_a^{(1)}$ and h^a :

$$\langle \kappa^{(1)}, \mathbf{h} \rangle \equiv h^a \kappa_a = -\lambda \hat{u}^b k_a \nabla_b l^a = \hat{u}^a \nabla_a \lambda - \lambda \hat{u}^b \hat{u}^a \nabla_b \hat{n}_a, \tag{B.12}$$

where we have used the definition of the ‘‘surface gravity’’ one-form (B.4), eqs. (B.5), (B.7), and the identity $\hat{u}_a \nabla_b \hat{n}^a = -\hat{n}_a \nabla_b \hat{u}^a$. Hence, the action of the 2D covariant derivative on $\langle \kappa^{(1)}, \mathbf{h} \rangle$ turns into

$${}^2 D_a \langle \kappa^{(1)}, \mathbf{h} \rangle = {}^2 D_a (\hat{u}^b \partial_b \lambda) - (\hat{u}^b \hat{u}^c \nabla_b \hat{n}_c) [{}^2 D_a \lambda] - \lambda [{}^2 D_a (\hat{u}^b \hat{u}^c \nabla_b \hat{n}_c)]. \tag{B.13}$$

The second term on the r.h.s. of (B.3) contains

$$\sigma_{ba}^{(\mathbf{m})} = \Theta_{ba}^{(\mathbf{m})} - \frac{q_{ba}}{2} \theta^{(\mathbf{m})} = \Theta_{ba}^{(\hat{\mathbf{n}})} - \frac{q_{ba}}{2} \theta^{(\hat{\mathbf{n}})} = \sigma_{ba}^{(\hat{\mathbf{n}})}. \tag{B.14}$$

Here we have used the definitions $\Theta_{ab}^{(\mathbf{m})} = q_a^c q_b^d \nabla_c m_d$, $\theta^{(\mathbf{m})} = \text{Tr} \Theta_{ab}^{(\mathbf{m})}$, and the corresponding relation from (B.5). Then, the action of ${}^2 D_a$ on $\sigma_{ab}^{(\mathbf{m})}$ results in

$${}^2 D^b \sigma_{ba}^{(\mathbf{m})} = \lambda (\sigma_{ba}^{(\hat{\mathbf{n}})} \hat{v}^b + {}^2 D^b \sigma_{ba}^{(\hat{\mathbf{n}})}). \tag{B.15}$$

Next, for $\theta^{(\mathbf{m})}$ and ${}^2 D_a \theta^{(\mathbf{m})}$ we have

$$\theta^{(\mathbf{m})} = \lambda \theta^{(\hat{\mathbf{n}})}, \quad {}^2 D_a \theta^{(\mathbf{m})} = \lambda (\theta^{(\hat{\mathbf{n}})} \hat{v}_a + {}^2 D_a \theta^{(\hat{\mathbf{n}})}). \tag{B.16}$$

For the fourth term on the r.h.s. of (B.3), on account of $C = -\lambda^2/2$ and the definition of $\theta^{(\mathbf{k})}$, we get

$$\theta^{(\mathbf{k})} {}^2 D_a C = -\frac{1}{2} q^{ab} \nabla_b k_a {}^2 D_a \lambda^2 = q_a^c \partial_c \lambda (\theta^{(\hat{\mathbf{n}})} - \theta^{(\hat{\mathbf{u}})}) = \lambda (\theta^{(\hat{\mathbf{n}})} - \theta^{(\hat{\mathbf{u}})}) \hat{v}_a. \tag{B.17}$$

Finally, taking into account (B.5) in the last term of (B.3), and dividing both sides on , we arrive at

$$\begin{aligned} q_a^c \mathcal{L}_{\hat{\mathbf{u}}} (-\Omega_c^{(\hat{\mathbf{n}})}) + \theta^{(\hat{\mathbf{u}})} (-\Omega_a^{(\hat{\mathbf{n}})}) &= q_a^b \partial_b \left(\frac{\theta^{(\hat{\mathbf{n}})}}{2} - \hat{u}^c \hat{u}^d \nabla_c \hat{n}_d \right) - {}^2 D^b \sigma_{ba}^{(\hat{\mathbf{n}})} + 8\pi q_a^c T_{cd} \hat{n}^d \\ &- \left(q_{ba} \hat{u}^c \hat{u}^d \nabla_c \hat{n}_d + \frac{\theta^{(\hat{\mathbf{n}})}}{2} q_{ba} + \sigma_{ba}^{(\hat{\mathbf{n}})} \right) \hat{v}^b - q_a^c \mathcal{L}_{\hat{\mathbf{u}}} \hat{v}_c + \lambda^{-1} q_a^c \partial_c (\hat{u}^b \partial_b \lambda). \end{aligned} \tag{B.18}$$

It is straightforward to verify that $\lambda^{-1} q_a^c \partial_c (\hat{u}^b \partial_b \lambda) = q_a^c \mathcal{L}_{\hat{\mathbf{u}}} \hat{v}_c$, so that two last terms on the r.h.s. of (B.18) cancel each other. Therefore, under the following replacements in eq. (B.18),

$$-\Omega_c^{(\hat{\mathbf{n}})} \rightsquigarrow \hat{\Omega}_a, \quad \theta^{(\hat{\mathbf{n}})} \rightsquigarrow \hat{\theta}, \quad -\hat{u}^b \hat{u}^a \nabla_b \hat{n}_a \rightsquigarrow \hat{g}, \quad \sigma_{ba}^{(\hat{\mathbf{n}})} \rightsquigarrow \hat{\sigma}_{ba}, \quad q_{ab} \rightsquigarrow \gamma_{ab}, \tag{B.19}$$

with omitting hats over the basic vectors $(\hat{\mathbf{u}}, \hat{\mathbf{n}})$, we get the following equation outside of the horizon:

$$\gamma_a^b \partial_b \left(\frac{\hat{\theta}}{2} + \hat{g} \right) - {}^2 D^b \hat{\sigma}_{ba} + \left(\gamma_{ac} \left(\hat{g} - \frac{\hat{\theta}}{2} \right) - \hat{\sigma}_{ac} \right) \hat{v}^c + 8\pi \gamma_a^c T_{cd} n^d = \gamma_a^c \mathcal{L}_{\hat{\mathbf{u}}} \hat{\Omega}_c + \hat{\Omega}_a \hat{\theta}. \tag{B.20}$$

Comparing this equation to eq. (12), we note that, modulo terms $\gamma_a^c \hat{\Omega}^b (\nabla_b u_c - \nabla_c u_b)$, two equations coincide. However, in the particular representation for u_a and n_a used in [15, 16],

$$u_a = -U h_a^b \nabla_b \tau, \quad n_a = N \nabla_a \rho, \tag{B.21}$$

with scalar functions U, τ, N and ρ , it is easy to verify $\gamma_a^c \hat{\Omega}^b (\nabla_b u_c - \nabla_c u_b) = 0$.

To sum up, we have proved the equivalence of the generalized DNS equation of Ref. [15] (eq. (B.3)) to the generalization of the DNS equation (eq. (12)) obtained within the Membrane Approach of [4].

C. THE NULL-HYPERSURFACE LIMIT OF THE GOURGOULHON'S GENERALIZATION OF THE DNS EQUATION

It was claimed in Ref. [15] that in the null-hypersurface limit eq. (B.3) turns into the standard version of the DNS equation. In this Appendix we will take this limit for the equivalent to (B.3) equation,

$$\gamma_a^c \mathcal{L}_u \hat{\Omega}_c + \theta^{(u)} \hat{\Omega}_a = \gamma_a^b \partial_b \left(\frac{\theta^{(n)}}{2} + \hat{g} \right) - {}^2 \mathbf{D}^b \sigma_{ba}^{(n)} + 8\pi \gamma_a^c T_{cd} n^d + \left(\gamma_{ba} \left(\hat{g} - \frac{\theta^{(n)}}{2} \right) - \sigma_{ba}^{(n)} \right) v^b. \tag{C.1}$$

The null-hypersurface limit is realized by eqs. (17) and (18), that are

$$\lim_{\alpha \rightarrow 0} \alpha u^a = l^a, \quad \lim_{\alpha \rightarrow 0} \alpha n^a = l^a, \quad l^b \nabla_b l^a = g_{\mathcal{H}} l^a.$$

In this limit, geometric quantities become divergent (if so) as inverse degrees of α . We will regularize them by turning to finite on the horizon variables, which are

$$\theta^{(u)} = \alpha^{-1} \bar{\theta}, \quad \theta^{(n)} = \alpha^{-1} \bar{\theta}, \quad \hat{g} = \alpha^{-1} \bar{g}, \quad \sigma_{ab}^{(n)} = \alpha^{-1} \bar{\sigma}_{ab}, \quad \Omega_a = \bar{\Omega}_a. \tag{C.2}$$

The bar over quantities means their regularity (finiteness) in the $\alpha \rightarrow 0$ limit.

Near the event horizon (on the stretched horizon, where α is small but not equal to zero) the vectors u^a and n^a admit the form

$$u^a = \alpha^{-1} l^a + \alpha \delta^a, \quad n^a = \alpha^{-1} l^a + \alpha \beta^a. \tag{C.3}$$

By use of the orthonormality relations between u^a and n^a , similar to eqs. (B.6), up to the 2nd order in α , we get

$$l^a \delta_a = -\frac{1}{2} + \mathcal{O}(\alpha^2), \quad l^a \beta_a = \frac{1}{2} + \mathcal{O}(\alpha^2), \tag{C.4}$$

from which it follows $l^a \delta_a = -l^a \beta_a$. Also, due to the orthogonality of u^a and n^a to the 2D induced metric γ_{ab} , the same property is translated onto the vectors δ^a and β^a . The representation (C.3) allows one to recover the regularized on the horizon $\theta^{(u)}, \theta^{(n)}, \sigma_{ab}^{(n)}$, and \hat{g} . For instance,

$$\theta^{(u)} \equiv \gamma^{ab} \nabla_b u_a = \alpha^{-1} \theta^{(1)} + \mathcal{O}(\alpha), \tag{C.5}$$

$$\theta^{(n)} \equiv \gamma^{ab} \nabla_b n_a = \alpha^{-1} \theta^{(1)} + \mathcal{O}(\alpha), \tag{C.6}$$

where we have used the orthogonality of δ^a and β^a to γ_{ab} , and the definition of $\theta^{(1)} \equiv \gamma^{ab} \nabla_b l_a$. Comparing the obtained results to (C.2), we conclude that

$$\bar{\theta} = \theta^{(1)} + \mathcal{O}(\alpha^2). \tag{C.7}$$

Next, for $\sigma_{ab}^{(n)}$, we arrive at

$$\sigma_{ab}^{(n)} = \alpha^{-1} \sigma_{ab}^{(1)} + \mathcal{O}(\alpha) \quad \rightsquigarrow \quad \bar{\sigma}_{ab} = \sigma_{ab}^{(1)} + \mathcal{O}(\alpha^2). \tag{C.8}$$

Computations of \hat{g} are more involved. Here we have

$$\begin{aligned} \hat{g} &= -u^a u^b \nabla_b n_a = -(\alpha^{-1} l^a + \alpha \delta^a)(\alpha^{-1} l^b + \alpha \delta^b) \nabla_b n_a \\ &= -(\alpha^{-2} l^a l^b \nabla_b n_a + l^a \delta^b \nabla_b n_a + l^b \delta^a \nabla_b n_a + \alpha^2 \delta^a \delta^b \nabla_b n_a), \end{aligned} \tag{C.9}$$

after that we have to use eqs. (C.4), together with the relations $l^b \nabla_b l^a = g_{\mathcal{H}} l^a$, $l^a l_a = 0$ and $l^a \nabla \beta_a = -\beta^a \nabla l_a$. As a result, we arrive at

$$\hat{g} = \alpha^{-1} \left(g_{\mathcal{H}} - l^b \partial_b \ln \alpha + \mathcal{O}(\alpha^2) \right), \tag{C.10}$$

that gives

$$\bar{g} = g_{\mathcal{H}} - l^b \partial_b \ln \alpha + \mathcal{O}(\alpha), \quad (\text{C.11})$$

with the surface gravity $g_{\mathcal{H}}$. Also, one can see that $v_a = \gamma_a^c u^b \nabla_b u_c = v_a^{\text{finite}} + \mathcal{O}(\alpha^2)$.

Now, in terms of the regular on the horizon variables (up to the leading order in α), eq. (C.1) turns out to be

$$\begin{aligned} \gamma_a^c \mathcal{L}_l \Omega_c + \theta^{(1)} \Omega_c \cong & \gamma_a^b \partial_b \left(g_{\mathcal{H}} - l^b \partial_b \ln \alpha + \frac{\theta^{(1)}}{2} \right) - {}^2 \mathbf{D}^b \sigma_{ba}^{(1)} + 8\pi \gamma_a^c T_{cd} l^d \\ & + \left(\sigma_{ba}^{(1)} - \left(\frac{\theta^{(1)}}{2} + g_{\mathcal{H}} - l^b \partial_b \ln \alpha \right) \gamma_{ba} \right) \gamma^{bc} \partial_c \ln \alpha + \left(\left(g_{\mathcal{H}} - l^b \partial_b \ln \alpha - \frac{\theta^{(1)}}{2} \right) \gamma_{ba} - \sigma_{ba}^{(1)} \right) v^b. \end{aligned} \quad (\text{C.12})$$

Comparing the so obtained eq. (C.12) with the original DNS equation

$$\gamma_a^c \mathcal{L}_l \Omega_c + \theta^{(1)} \Omega_c = \gamma_a^b \partial_b \left(g_{\mathcal{H}} + \frac{\theta^{(1)}}{2} \right) - {}^2 \mathbf{D}^b \sigma_{ba}^{(1)} + 8\pi \gamma_a^c T_{cd} l^d, \quad (\text{C.13})$$

we derive the same conditions on the regularization function α as in the main text of the paper (cf. eqs. (33)):

$$\left(\left(g_{\mathcal{H}} - \frac{\theta^{(1)}}{2} \right) \gamma_{ab} - \sigma_{ab}^{(1)} \right) v^b \stackrel{\mathcal{H}}{=} \left(\left(\frac{\theta^{(1)}}{2} + g_{\mathcal{H}} \right) \gamma_{ab} - \sigma_{ab}^{(1)} \right) \gamma^{bc} \partial_c \ln \alpha, \quad l^b \partial_b \ln \alpha \stackrel{\mathcal{H}}{=} 0. \quad (\text{C.14})$$

Here the symbol “ $\stackrel{\mathcal{H}}{=}$ ” is reserved for computing quantities and their derivatives on the horizon.

Now, let's fix the particular choice of u^a and n^a vectors from Appendix B (eq. (B.8)):

$$\hat{u}^a = \frac{1}{\lambda} l^a + \frac{\lambda}{2} k^a, \quad \hat{n}^a = \frac{1}{\lambda} l^a - \frac{\lambda}{2} k^a, \quad (\text{C.15})$$

and let's assume that l^a is the event horizon null-generator, i.e., $l^b \nabla_b l^a = g_{\mathcal{H}} l^a$. Since the parameter λ in (C.15) is free, we can identify it with the regularization function α . Then, since as an outcome of Appendix B we have obtained $\hat{v}_a = \gamma_a^c \lambda^{-1} \partial_b \lambda$, we will have $v^b \stackrel{\mathcal{H}}{=} \gamma^{bc} \partial_c \ln \alpha$ on the horizon.

The second condition of (C.14) is always satisfied with the given choice of the regularization function. The rest of (C.14) is

$$\theta^{(1)} \gamma_b^c \partial_c \ln \alpha \stackrel{\mathcal{H}}{=} 0, \quad (\text{C.16})$$

which requires either space-time configurations with the trivial vector v_a , or, in the case of finite-valued v_a on the horizon, the trivial on the horizon expansion $\theta^{(1)} \stackrel{\mathcal{H}}{=} 0$. For example,

- for the Kerr BH, $l^b \partial_b \ln \hat{\alpha} = 0$, $\gamma_b^c \partial_c \ln \hat{\alpha} \stackrel{\mathcal{H}}{=} \text{finite} \neq 0$, and $\theta^{(1)} \stackrel{\mathcal{H}}{=} 0$,
- for the Schwarzschild BH, $l^b \partial_b \ln \hat{\alpha} = 0$, $\gamma_b^c \partial_c \ln \hat{\alpha} = 0$, and $\theta^{(1)} \stackrel{\mathcal{H}}{=} 0$.

Now, it becomes clear that the claim of [15] on the equivalence of eq. (B.3) to eq. (C.13) in the horizon (null-hypersurface) limit is based on the possibility, within the approach of [15, 16], to fix $C = 0$ and $h^a = m^a = l^a$ (see eq. (B.3)). Put it differently, in terms of the vector v_a and the regularization function α , in Ref. [15] it is silently supposed that we can always fix $v_a = 0$ in the $\alpha \rightarrow 0$ limit. However, as we have convinced on the example of the Kerr Black Hole, it is not always possible for a general Black Hole spacetime metric.

ORCID

 **A.M. Arslanaliev**, <https://orcid.org/0000-0002-8667-9688>;  **A.J. Nurmagambetov**, <https://orcid.org/0000-0001-5175-5997>

REFERENCES

- [1] K.S. Thorne, R.H. Price, and D.A. Macdonald, *Black Holes: The Membrane Paradigm*, (Yale Univ. Pr., New Haven, 1986).
- [2] T. Damour, Phys. Rev. D, **18**, 3598 (1978). <http://dx.doi.org/10.1103/PhysRevD.18.3598>
- [3] T. Damour, in: *Proceedings of the second Marcel Grossmann Meeting on general relativity*, edited by R. Ruffini (North-Holland, 1982), pp. 508-687.
- [4] M. Parikh, and F. Wilczek, Phys. Rev. D, **58**, 064011 (1998). <http://dx.doi.org/10.1103/PhysRevD.58.064011>
- [5] P.K. Kovtun, and A.O. Starinets, Phys. Rev. D, **72**, 086009 (2005). <http://dx.doi.org/10.1103/PhysRevD.72.086009>
- [6] J. de Boer, M.P. Heller, and N. Pinzani-Fokeeva, Phys. Rev. D, **91**, 026006 (2015). <http://dx.doi.org/10.1103/PhysRevD.91.026006>

- [7] P. Kovtun, D.T. Son, and A.O. Starinets, JHEP, **10**, 064 (2003). <http://dx.doi.org/10.1088/1126-6708/2003/10/064>
- [8] N. Iqbal, and H. Liu, Phys. Rev. D, **79**, 025023 (2009). <http://dx.doi.org/10.1103/PhysRevD.79.025023>
- [9] P. Kovtun, and A. Ritz, Phys. Rev. D, **78**, 066009 (2008). <http://dx.doi.org/10.1103/PhysRevD.78.066009>
- [10] A. Ritz, Int. J. Mod. Phys. A, **25**, 433 (2010). <http://dx.doi.org/10.1142/S0217751X10048731>
- [11] I. Bredberg, C. Keeler, V. Lysov, and A. Strominger, JHEP, **03**, 141 (2011). [http://dx.doi.org/10.1007/JHEP03\(2011\)141](http://dx.doi.org/10.1007/JHEP03(2011)141)
- [12] T. Faulkner, H. Liu, and M. Rangamani, JHEP, **08**, 051 (2011). [http://dx.doi.org/10.1007/JHEP08\(2011\)051](http://dx.doi.org/10.1007/JHEP08(2011)051)
- [13] A.J. Nurbagametov, and A.M. Arslanaliev, LHEP, **2022**, 328 (2022). <http://dx.doi.org/10.31526/lhep.2022.328>
- [14] C.W. Misner, K.S. Thorne, and J.A. Wheeler, *Gravitation*, (Freeman W.H. and Co., San Francisco. 1973).
- [15] E. Gourgoulhon, Phys. Rev. D, **72**, 104007 (2005). <http://dx.doi.org/10.1103/PhysRevD.72.104007>
- [16] E. Gourgoulhon, and J.L. Jaramillo, Phys. Rept., **423**, 159 (2006). <http://dx.doi.org/10.1016/j.physrep.2005.10.005>
- [17] N. Straumann, *General Relativity*, (Springer, 2013).
- [18] A. Raychaudhuri, Phys. Rev., **98**, 1123 (1955). <http://dx.doi.org/10.1103/PhysRev.98.1123>
- [19] T. Padmanabhan, Phys. Rev. D, **83**, 044048 (2011). <http://dx.doi.org/10.1103/PhysRevD.83.044048>
- [20] L. Li, and T. Wang, Preprint arXiv:1710.00744 [gr-qc], <http://dx.doi.org/10.48550/arXiv.1710.00744>
- [21] M. Alcubierre, *Introduction to 3+1 Numerical Relativity*, (Oxford, 2008).
- [22] P. Hájiček, Commun. Math. Phys., **36**, 305 (1974). <http://dx.doi.org/10.1007/BF01646202>
- [23] P. Hájiček, Commun. Math. Phys., **34**, 37 (1973). <http://dx.doi.org/10.1007/BF01646541>
- [24] P. Hájiček, J. Math. Phys., **15**, 1554 (1974). <http://dx.doi.org/10.1063/1.1666846>
- [25] P. Hájiček, J. Math. Phys., **16**, 518 (1975). <http://dx.doi.org/10.1063/1.522575>
- [26] A. Ashtekar, C. Beetle, and S. Fairhurst, Class. Quant. Grav., **16**, L1 (1999). <http://dx.doi.org/10.1088/0264-9381/16/2/027>
- [27] J.B. Hartle, and K.S. Thorne, Astrophys. J., **153**, 807 (1968). <http://dx.doi.org/10.1086/149707>
- [28] T. Johannsen, and D. Psaltis, Phys. Rev. D, **83**, 124015 (2011). <http://dx.doi.org/10.1103/PhysRevD.83.124015>
- [29] L. Rezzolla, and A. Zhidenko, Phys. Rev. D, **90**, 084009 (2014). <http://dx.doi.org/10.1103/PhysRevD.90.084009>
- [30] R. Konoplya, L. Rezzolla, and A. Zhidenko, Phys. Rev. D, **93**, 064015 (2016). <http://dx.doi.org/10.1103/PhysRevD.93.064015>
- [31] R.A. Konoplya, and A. Zhidenko, JCAP, **08**, 008 (2023). <http://dx.doi.org/10.1088/1475-7516/2023/08/008>
- [32] G.G.L. Nashed, and K. Bamba, Nucl. Phys. B, **994**, 116325 (2023). <http://dx.doi.org/10.1016/j.nuclphysb.2023.116325>
- [33] J. Hartong, E. Have, N.A. Obers, and I. Pikovski, SciPost Phys., **16**, 088 (2024). <http://dx.doi.org/10.21468/SciPostPhys.16.3.088>

ЛІМІТ НУЛЬОВОЇ ГІПЕРПОВЕРХНІ В МЕМБРАННОМУ ПІДХОДІ ПАРІХА-ВІЛЬЧЕКА

А.М. Арсланалієв^a, О.Ю. Нурмагамбетов^{a,b,c}

^aІнститут теоретичної фізики імені О.І. Ахієзера ННЦ ХФТІ, вул. Академічна, 1, Харків, 61108, Україна

^bХарківський національний університет імені В.Н. Каразіна, майдан Свободи, 4, Харків, 61022, Україна

^cІнститут радіофізики та електроніки імені О.Я. Усикова, вул. Ак. Проскури, 12, Харків, 61085, Україна

Ми розглядаємо тонкощі взяття ліміту нуль-гіперповерхні (горизонту подій) в мембранному підході Паріха-Вільчека до чорних дір. Зокрема, уточнено відповідність між спроектованими рівняннями гравітації Ейнштейна з речовиною та рівняннями релятивістської гідродинаміки Райчаудхурі-Дамура-Нав'є-Стокса (РДНС). Для загальної конфігурації гравітації з речовиною ми отримуємо додаткові члени в гідродинамічних рівняннях, які включають специфічні комбінації згорнутих логарифмічних похідних параметра (функції регуляризації), що визначає близькість розтягнутої мембрани до горизонту чорної діри. Проте прямі обчислення нових членів для точних (Шварцшильда і Керра) розв'язків чорних дір підказують стандартну форму рівнянь РДНС через властивість нерозширюваного горизонту цих розв'язків. Тому зведення розширених рівнянь РДНС до їхньої класичної форми можна розглядати як додаткову умову узгодженості в гідродинаміці точних розв'язків чорних дір, а також як нетривіальний тест для різних життєздатних наближень метрики простору-часу. Ми детально порівнюємо мембранний підхід Паріха-Вільчека з методом Гургулона-Харамільйо для опису нульової гіперповерхні, а також даємо зв'язок отриманих результатів з нашою попередньою роботою щодо керрівських чорних дір.

Ключові слова: чорні діри; мембранна парадігма; релятивістська гідродинаміка

FLAT FRIEDMANN-LEMAÎTRE-ROBERTSON-WALKER COSMOLOGICAL MODEL WITH TIME-DEPENDENT COSMOLOGICAL CONSTANT IN BRANS-DICKE THEORY OF GRAVITY

 Anindita Basumatary,  Chandra Rekha Mahanta

Department of Mathematics, Gauhati University, Guwahati -781014, India

**Corresponding Author e-mail: anibasus3@gmail.com*

Received September 1, 2024; revised October 24, 2024; in final form November 2, 2024; accepted November 7, 2024

Recently, there has been much interest in investigating outstanding problems of cosmology with modified theories of gravity. The Brans-Dicke theory of gravity is one such theory developed by Brans and Dicke absorbing Mach's principle into the General Theory of Relativity. In Brans-Dicke theory, gravity couples with a time-dependent scalar field ϕ through a coupling parameter ω . This theory reduces to the General Theory of Relativity if the scalar field ϕ is constant and the coupling parameter $\omega \rightarrow \infty$. In this paper, we consider a flat Friedmann-Lemaître-Robertson-Walker (FLRW) universe with a time-dependent cosmological constant in Brans-Dicke theory of gravity. Exact solutions of the field equations are obtained by using a power law relation between the scale factor and the Brans-Dicke scalar field ϕ and by taking the Hubble parameter H to be a hyperbolic function of the cosmic time t . We study the cosmological dynamics of our model by graphically representing some important cosmological parameters such as the deceleration parameter, energy density parameter, equation of state parameter, jerk parameter, snap parameter, lerk parameter etc. The statefinder diagnostic pair of the model is also obtained and the validity of the four energy conditions, viz. the Strong energy condition (SEC), Weak energy condition (WEC), Dominant energy condition (DEC) and Null energy condition (NEC), is examined. We find that the universe corresponding to our model is expanding throughout its evolution and exhibits late time cosmic acceleration, which is in agreement with the current observational data.

Keywords: *Brans-Dicke theory; Friedmann-Lemaître-Robertson-Walker universe; Cosmological constant; Hubble parameter; Deceleration parameter*

PACS: 04.20.Jb, 04.50.Kd, 98.80.-k, 98.80.Jk

1. INTRODUCTION

Recent cosmological and astrophysical observations such as SNIa, CMB (Cosmic Microwave Background), LSS (Large Scale Structure), WMAP (Wilkinson Microwave Anisotropy Probe), SDSS (Sloan Digital Sky Survey) etc. [1]-[10] strongly suggest that our universe is currently undergoing a phase of accelerated expansion. Within the framework of General Relativity, an exotic component with large negative pressure, dubbed dark energy, is considered to be responsible for this expansion. There is also no dearth of candidate for dark energy, the cosmological constant Λ being the simplest and the most natural one which fits the observations well. Another possibility in explaining the observed cosmic acceleration is that at large scales the gravity model of General Relativity breaks down and an action more general than the Einstein-Hilbert action describes the gravitational field.

In recent years, a number of modified gravity theories are considered in literature, and one such theory is the Brans-Dicke theory [11] in which gravity couples with a time-dependent scalar field ϕ through a dimensionless coupling constant ω . The scalar field ϕ plays the role of the inverse of Newton's gravitational constant G , and for a constant ϕ , the Brans-Dicke theory reduces to the General Theory of Relativity where G plays the role of coupling between the gravity of space-time and matter in it. The Brans-Dicke theory has passed solar system experimental tests [12], CMB data [13] and Planck data [14]. Many cosmological models are also constructed by several authors by utilizing this theory in different contexts. Very recently, Song *et al.* [15] have studied alternative dynamics in loop quantum Brans-Dicke cosmology, Tripathy *et al.* [16] have studied a bouncing scenario in the framework of generalised Brans-Dicke theory, Sharif and Majid [17] constructed anisotropic spherical solutions from some known isotropic solutions in the background of self-interacting Brans-Dicke theory and Hatkar *et al.* [18] have explored viscous holographic dark energy in the context of Brans-Dicke theory. Yadav [19] has investigated power-law variation of the scalar field ϕ with the scale factor a of FRW universe filled with dark matter and Tsallis type holographic dark energy. Yadav *et al.* [20] have investigated a Bianchi type-I transitioning universe with hybrid scalar field, Mishra and Dua [21] have examined the dynamics of flat FLRW model of universe with time varying cosmological constant $\Lambda(t)$ and Santhi *et al.* [22] have analyzed some Bianchi type viscous holographic dark energy models in Brans-Dicke theory of gravity. Various authors have also constructed hyperbolic cosmological models in different contexts.

Chand *et al.*, [23] investigated the flat, open and closed Friedmann-Robertson-Walker model within the framework of the Brans-Dicke theory of gravity. The authors have constructed cosmological models for a hyperbolic scale factor and a hybrid scale factor. They have obtained the negative pressure throughout the cosmic evolution for a closed universe in case of the hyperbolic scale factor model whereas in case of hybrid scale factor model, pressure is negative throughout the evolution for both flat and closed universe. Also a negative Λ is obtained throughout the cosmic evolution for an open universe in the hyperbolic scale factor model, and in case of the hybrid scale factor model negative Λ is obtained in the early phases of evolution for open, flat and closed universe. Also their model initially starts from Chaplygin gas region and approaches to Λ CDM model at late times. Esmaili [24] has constructed two cosmological models in $f(R, T)$ theory using the scale factor a in a hyperbolic form, and a power law form as a fraction of exponential function. Esmaili and Mishra [25] have constructed a Bianchi type VI_h cosmological model in the framework of $f(R, T)$ theory, using a hyperbolic scale factor. Mishra *et al.* [26] have presented a few cosmological models in the $f(R, T)$ theory. They have also studied two cosmological models: (i) a hyperbolic scale factor model and (ii) a model with specific form of the Hubble parameter. Mishra *et al.* [27] have also presented and analyzed a Bianchi type I cosmological model in the $f(R, T)$ gravity theory with an anisotropic variable parameter in the form of hyperbolic function. Esmaili [24], Esmaili and Mishra [25] and Mishra *et al.* [27] have found the SEC to violate throughout the cosmic evolution.

In this work we study the cosmological dynamics of a flat FLRW universe filled with a perfect fluid in Brans-Dicke theory of gravity with a time dependent cosmological constant by considering the Hubble parameter H to be a hyperbolic function of cosmic time t . This paper is organised as follows: In section 2, we derive the Brans-Dicke field equations with time-dependent cosmological constant Λ corresponding to a flat Friedmann-Lemaître-Robertson-Walker metric. In section 3, we obtain cosmological solutions of Brans-Dicke field equations by assuming the Hubble parameter to be a hyperbolic function of the cosmic time t , and by using a power law relation between the Brans-Dicke scalar field ϕ and the scale factor a . In section 4, we study the physical and kinematical properties of the model by graphically representing some parameters of cosmological importance. In section 5, we study the evolution of some cosmographic parameters. In section 6, the statefinder diagnostic pair is obtained. In section 7, we examine the validity of the energy conditions. We conclude the paper in section 8 with a brief discussion.

2. METRIC AND THE FIELD EQUATIONS

We consider the Brans-Dicke action in the form

$$S = \int [(R - 2\Lambda)\phi + 16\pi\mathcal{L} + \frac{\omega}{\phi}\phi_{,i}\phi^{,i}] \sqrt{-g} d^4x \tag{1}$$

where R is the Ricci scalar, Λ is the time-dependent cosmological constant, ϕ is a scalar field, \mathcal{L} is the matter-Lagrangian density, ω is the dimensionless Brans-Dicke coupling constant, g is the determinant of the metric tensor g_{ij} and coma (,) represents the ordinary derivative.

Taking variations of the action (1) with respect to g^{ij} and ϕ , the Brans-Dicke field equations are obtained as

$$R_{ij} - \frac{R}{2}g_{ij} + \Lambda g_{ij} = -\frac{8\pi T_{ij}}{\phi} - \frac{\omega}{\phi^2}(\phi_{,i}\phi_{,j} - \frac{1}{2}g_{ij}\phi_{,k}\phi^{,k}) - \frac{1}{\phi}(\phi_{,i;j} - g_{ij}\square\phi) \tag{2}$$

and

$$\square\phi = \frac{8\pi T + 2\Lambda\phi}{(3 + 2\omega)} \tag{3}$$

where R_{ij} is the Ricci tensor, T_{ij} is the energy-momentum tensor, \square is the D'Alembert operator, $T = g^{ij}T_{ij}$ is the trace of the energy-momentum tensor and semicolon (;) represents the covariant derivative.

We consider the universe to be filled with a perfect fluid of density ρ and pressure p . The energy-momentum tensor T_{ij} for a perfect cosmic fluid is given by

$$T_{ij} = (\rho + p)u_i u_j - p g_{ij} \tag{4}$$

where u_i is the four velocity.

The line-element for a flat Friedmann-Lemaître-Robertson-Walker (FLRW) universe is given by

$$ds^2 = dt^2 - a^2(dr^2 + r^2 d\theta^2 + r^2 \sin^2\theta d\phi^2) \tag{5}$$

where $a = a(t)$ is the scale factor.

For the line element (5), the Brans-Dicke field equations (2) and (3) give

$$2\frac{\ddot{a}}{a} + \frac{\dot{a}^2}{a^2} + \frac{\omega}{2}\frac{\dot{\phi}^2}{\phi^2} + 2\frac{\dot{a}}{a}\frac{\dot{\phi}}{\phi} + \frac{\ddot{\phi}}{\phi} - \Lambda = -\frac{8\pi\rho}{\phi} \tag{6}$$

$$3\frac{\dot{a}^2}{a^2} - \frac{\omega}{2}\frac{\dot{\phi}^2}{\phi^2} + 3\frac{\dot{a}}{a}\frac{\dot{\phi}}{\phi} - \Lambda = \frac{8\pi\rho}{\phi} \tag{7}$$

$$(3 + 2\omega) \left(\frac{\ddot{\phi}}{\phi} + 3 \frac{\dot{a}}{a} \frac{\dot{\phi}}{\phi} \right) - 2\Lambda = \frac{8\pi(\rho - 3p)}{\phi} \quad (8)$$

where \dot{a} is the derivative of the scale factor a with respect to cosmic time t .

3. COSMOLOGICAL SOLUTIONS OF THE BRANS-DICKE FIELD EQUATIONS

We have three field equations with five unknowns a , ϕ , Λ , p and ρ . In order to determine an exact solution of the field equations, we need two more equations relating the unknowns.

We consider a power law relation between the scalar field ϕ and the scale factor a as

$$\phi = \phi_0 a^m \quad (9)$$

where ϕ_0 is the proportionality constant and m is an arbitrary constant.

Also, we consider the Hubble parameter H to be a hyperbolic function of cosmic time t and take

$$H(t) = \alpha\beta \coth(2\alpha t) \quad (10)$$

where $\alpha > 0$, $\beta > 0$ are constants. The Hubble parameter H is defined as $H = \frac{\dot{a}}{a}$. Therefore, from (10), we obtain the scale factor a as

$$a(t) = a_0 \{ \sinh(2\alpha t) \}^{\frac{\beta}{2}} \quad (11)$$

where a_0 is the present value of the scale factor a .

Using relations (9) and (11) in (6)-(8), we obtain

$$\Lambda(t) = 2\alpha^2\beta(m\omega - 3) \{ \operatorname{cosech}(2\alpha t) \}^2 + \alpha^2\beta^2 \left(6 - \frac{m^2\omega}{2} - 3m\omega \right) \{ \coth(2\alpha t) \}^2 \quad (12)$$

$$\begin{aligned} p(t) = & \frac{\phi_0 a_0^m}{8\pi} \{ \sinh(2\alpha t) \}^{\frac{m\beta}{2}} \left[2\alpha^2\beta(m + m\omega - 1) \{ \operatorname{cosech}(2\alpha t) \}^2 \right] \\ & + \frac{\phi_0 a_0^m}{8\pi} \{ \sinh(2\alpha t) \}^{\frac{m\beta}{2}} \left[\alpha^2\beta^2(3 - 2m - 3m\omega - m^2 - m^2\omega) \{ \coth(2\alpha t) \}^2 \right] \end{aligned} \quad (13)$$

$$\begin{aligned} \rho(t) = & \frac{\phi_0 a_0^m}{8\pi} \{ \sinh(2\alpha t) \}^{\frac{m\beta}{2}} \left[2\alpha^2\beta(3 - m\omega) \{ \operatorname{cosech}(2\alpha t) \}^2 \right] \\ & + \frac{\phi_0 a_0^m}{8\pi} \{ \sinh(2\alpha t) \}^{\frac{m\beta}{2}} \left[3\alpha^2\beta^2(m + m\omega - 1) \{ \coth(2\alpha t) \}^2 \right] \end{aligned} \quad (14)$$

From (9), we obtain the expression for the scalar field ϕ as

$$\phi = \phi_0 [a_0 \{ \sinh(2\alpha t) \}]^{\frac{m\beta}{2}} \quad (15)$$

4. PHYSICAL AND KINEMATICAL PROPERTIES OF THE MODEL

The spatial volume parameter $V(t)$ of the model is obtained as

$$V(t) = \{a(t)\}^3 = a_0^3 \{ \sinh(2\alpha t) \}^{\frac{3\beta}{2}} \quad (16)$$

The deceleration parameter q , which indicates whether the cosmic expansion is uniform, decelerating or accelerating, is defined by $q(t) = -\frac{1}{aH^2} \frac{d^2a}{dt^2} = -1 - \frac{\dot{H}}{H^2}$.

For our model,

$$q(t) = \frac{2}{\beta} \{ \operatorname{sech}(2\alpha t) \}^2 - 1 \quad (17)$$

The expansion scalar $\theta(t)$, defined by $\theta = 3H$, is obtained as

$$\theta(t) = 3\alpha\beta \coth(2\alpha t) \quad (18)$$

Using the relations (13) and (14), we obtain the equation of state (EoS) parameter $\eta(t) = \frac{p(t)}{\rho(t)}$ as

$$\eta(t) = \frac{2\alpha^2\beta(m + m\omega - 1) \{ \operatorname{cosech}(2\alpha t) \}^2 + \alpha^2\beta^2(3 - 2m - 3m\omega - m^2 - m^2\omega) \{ \coth(2\alpha t) \}^2}{2\alpha^2\beta(3 - m\omega) \{ \operatorname{cosech}(2\alpha t) \}^2 + 3\alpha^2\beta^2(m + m\omega - 1) \{ \coth(2\alpha t) \}^2} \quad (19)$$

Now, in order to study the physical and kinematical properties of the constructed model, we represent the evolution of various parameters graphically by using the expressions obtained above in figure 1 to figure 10, which enables us to have a better understanding about the evolving universe corresponding to our model.

We plot the scale factor a , spatial volume V and scalar field ϕ against the cosmic time t for $\alpha = 0.107$, $\beta = 0.603$ in figures 1, 2 and 3 respectively. These figures show that the scale factor a , spatial volume V and scalar field ϕ relates to the cosmic time t with direct proportionality, thereby showing the increasing behaviour throughout the universe's evolution, hinting about the evolution of the observable universe at an accelerated rate at late times.

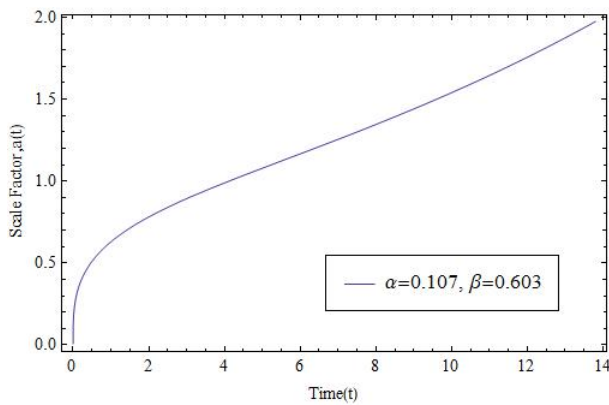


Figure 1. Evolution of the scale factor a vs cosmic time t for $\alpha = 0.107$, $\beta = 0.603$, $a_0 = 1$

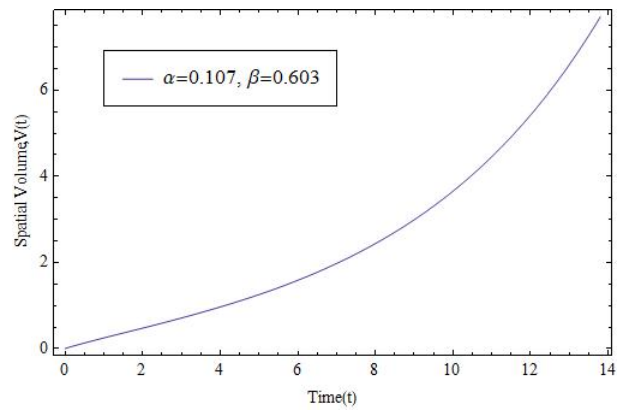


Figure 2. Evolution of the spatial volume V vs cosmic time t for $\alpha = 0.107$, $\beta = 0.603$, $a_0 = 1$

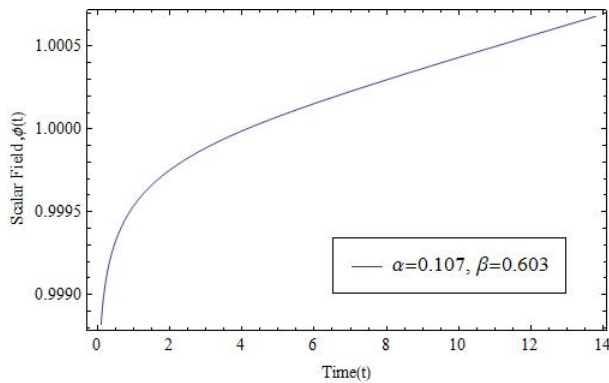


Figure 3. Evolution of the scalar field ϕ vs cosmic time t for $\alpha = 0.107$, $\beta = 0.603$, $a_0 = \phi_0 = 1$, $m = 0.001$

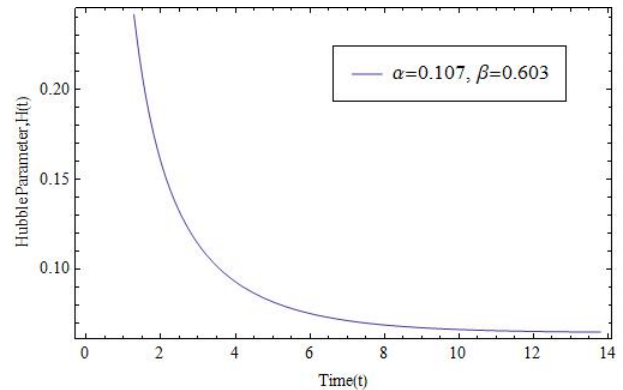


Figure 4. Evolution of the Hubble parameter H vs cosmic time t for $\alpha = 0.107$, $\beta = 0.603$

Figure 4 displays the variation of Hubble parameter H against the cosmic time t and figure 5 displays the expansion scalar plots against the cosmic time t . The Hubble parameter H and expansion scalar θ , which provides information regarding the expansion rate of the evolving universe, relates to the cosmic time t with an inverse proportionality like relation, which in turn results in the continuous decreasing nature and fading away of the Hubble parameter H and expansion scalar θ , signifying the late time phases of accelerated cosmic expansion.

Evolution of the deceleration parameter q against the cosmic time t is displayed in the figure 6. It undergoes a transition from an early phase with positive values to attain negative ones at a later phase ($t \sim 5.64$) of cosmic evolution. The transition is an evident hint of the decelerating phase of evolution of the universe turning into an accelerating one at a later phase. At late times, q tends to -1 , which indicates that the evolving universe undergoes the phase of accelerated expansion at late times.

Figure 7 displays the graphical representation of the cosmological constant Λ against the cosmic time t . It is seen that, Λ is negative in the early phases of cosmic evolution, which later attains the positive values.

Figure 8 shows the variation of the pressure of the cosmic fluid with the increasing cosmic time t . A decreasing behaviour of $p(t)$ is seen transitioning from positive values at early phases to negative values at a later phase of the cosmic

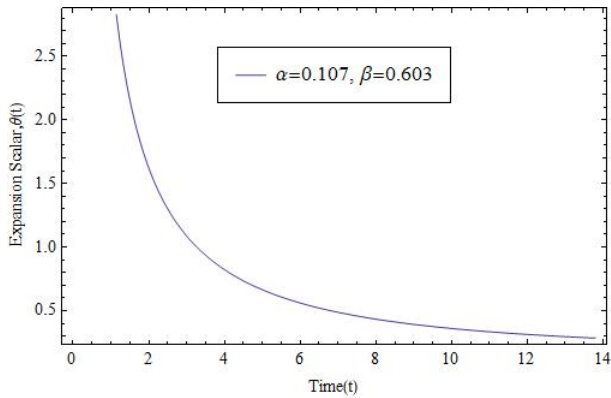


Figure 5. Evolution of the expansion scalar θ vs cosmic time t for $\alpha = 0.107$, $\beta = 0.603$

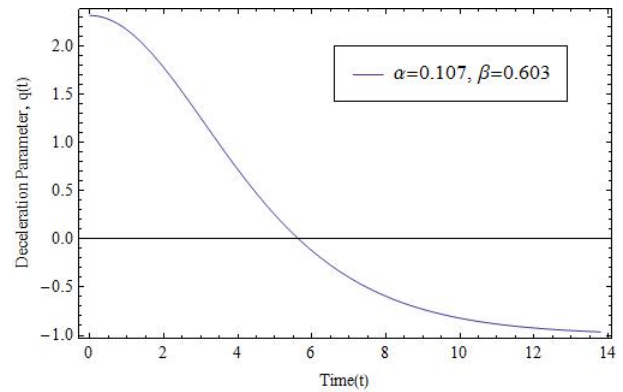


Figure 6. Evolution of the deceleration parameter q vs cosmic time t for $\alpha = 0.107$, $\beta = 0.603$

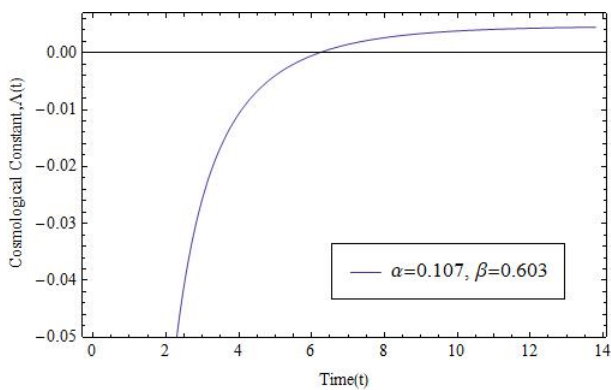


Figure 7. Evolution of the cosmological constant Λ vs cosmic time t for $\alpha = 0.107$, $\beta = 0.603$, $m = 0.001$, $\omega = 1628$

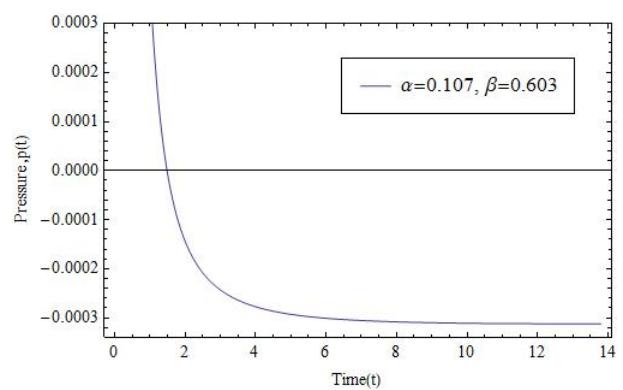


Figure 8. Evolution of the pressure p vs cosmic time t for $\alpha = 0.107$, $\beta = 0.603$, $a_0 = \phi_0 = 1$, $m = 0.001$, $\omega = 1628$

evolution. Thus the graph of $p(t)$ versus cosmic time t is indicating the early era of radiation domination transitioning to the era of dark energy domination at future phases of cosmic evolution, passing through the era of matter domination ($p = 0$ at $t \sim 1.49$). The negative pressure indicates the presence of some exotic component in the universe, dubbed dark energy, which could possibly be responsible for the late time cosmic acceleration.

In figure 9, it is seen that the energy density ρ is inversely proportional to the cosmic time t . $\rho(t)$ decreases gradually but remain positive throughout the evolution of the universe which eventually tends to zero at late times, hinting that the universe will keep expanding forever.

Figure 10 illustrates the evolution of the EoS parameter η which decreases as the universe evolves. It is positive in the early universe, signifying the radiation dominating era of the early universe, which later crosses the fixed point $\eta = 0$ at $t \sim 1.49$ signifying the matter dominating era, and attains the negative values signifying the dark energy dominating era. Upto a certain period of time, our model lies in the region of quintessence phase ($-1 < \eta < -\frac{1}{3}$), within $t \sim 5.22 - t \sim 24.55$, later $\eta(t)$ attains the value -1 at $t \sim 22.8$ till the future phases of evolution indicating the Λ CDM behaviour of the model at future phases of cosmic evolution. At the current epoch, $\eta \sim -0.96$ for $\alpha = 0.107$, $\beta = 0.603$.

5. EVOLUTION OF THE COSMOGRAPHIC PARAMETERS

The cosmographic parameters enable us in exploring the phenomena of cosmic evolution in a model independent manner. Hence we study the evolution of the cosmographic parameters viz., the jerk parameter $j(t)$, snap parameter $s(t)$ and lerk parameter $l(t)$ which are defined as [28]

$$j(t) = \frac{1}{aH^3} \frac{d^3 a}{dt^3}, \quad s(t) = \frac{1}{aH^4} \frac{d^4 a}{dt^4} \quad \text{and} \quad l(t) = \frac{1}{aH^5} \frac{d^5 a}{dt^5}.$$

These parameters obtained from the Taylor series expansion of the scale factor $a(t)$ containing the third, fourth and fifth order cosmic time derivative of the scale factor $a(t)$ are dimensionless and are useful in understanding the cosmic evolution in a better way.

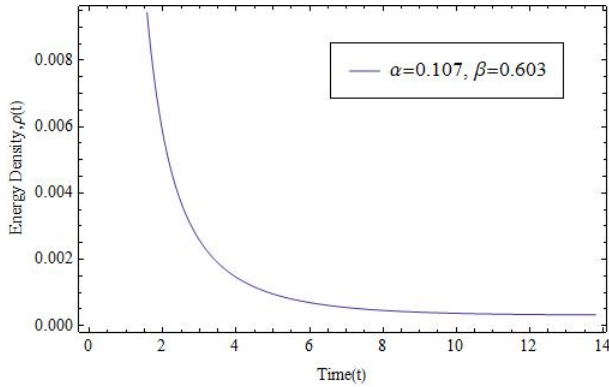


Figure 9. Evolution of the energy density ρ vs cosmic time t for $\alpha = 0.107, \beta = 0.603, a_0 = \phi_0 = 1, m = 0.001, \omega = 1628$

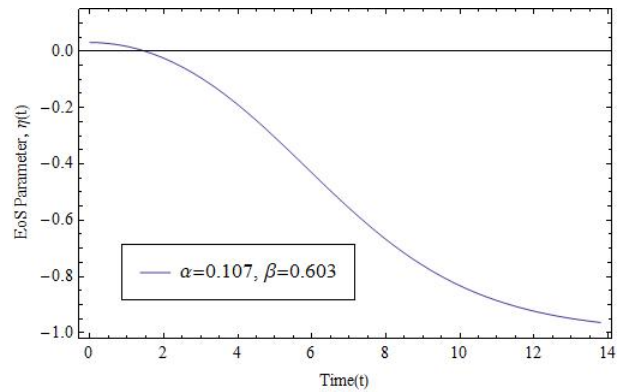


Figure 10. Evolution of the EoS parameter η vs cosmic time t for $\alpha = 0.107, \beta = 0.603, m = 0.001, \omega = 1628$

For our model, these parameters are obtained as

$$j(t) = \left(\frac{-6\beta + 8}{\beta^2} \right) \{ \text{sech}(2\alpha t) \}^2 + 1 \tag{20}$$

$$s(t) = \left(\frac{-12\beta^2 + 44\beta - 48}{\beta^3} \right) \{ \text{sech}(2\alpha t) \}^2 + \left(\frac{-12\beta + 16}{\beta^3} \right) \{ \text{sech}(2\alpha t) \}^2 \{ \tanh(2\alpha t) \}^2 + 1 \tag{21}$$

$$l(t) = \left(\frac{-20\beta^3 + 140\beta^2 - 400\beta + 384}{\beta^4} \right) \{ \text{sech}(2\alpha t) \}^2 + \left(\frac{-60\beta^2 + 240\beta - 256}{\beta^4} \right) \{ \text{sech}(2\alpha t) \}^2 \{ \tanh(2\alpha t) \}^2 + 1 \tag{22}$$

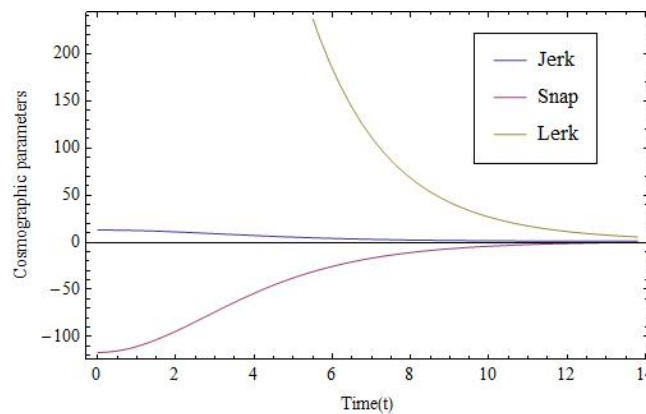


Figure 11. Evolution of the jerk (j), snap (s) and lerk (l) parameters vs cosmic time t for $\alpha = 0.107, \beta = 0.603$

From the graphical representation of the cosmographic parameters in figure 11, we observe that the universe corresponding to our model is expanding throughout its evolution and it exhibits the late time cosmic acceleration. The jerk, snap and lerk parameters tend to 1 at late times, agreeing with the current observational data.

6. STATEFINDER DIAGNOSTIC

The dimensionless geometric pair $\{r, s\}$, known as the statefinder pair [29], are defined as $r(t) = \frac{1}{aH^3} \frac{d^3 a}{dt^3}$ and $s(t) = \frac{2(1-r)}{3(1-2q)}$. These are useful in distinguishing various dark energy models including quintessence, Chaplygin gas, braneworld and other interacting models of dark energy successfully in a model independent manner. The pair helps in characterizing the dark energy properties. In particular, the Λ CDM and SCDM model behaviours of convergence or divergence can be found out with the help of the fixed position of the pair $\{r, s\}$. The fixed point $\{r = 1, s = 0\}$ resembles the Λ CDM behaviour of the model and the fixed point $\{r = 1, s = 1\}$ resembles the SCDM behaviour of the model, while the regions $\{r < 1, s > 0\}$ and $\{r > 1, s < 0\}$ respectively represents the phase of quintessence and Chaplygin gas like behaviour of

the model.

As our model indicates the presence of some exotic component in the universe with negative pressure, so it will be interesting to study the behaviour of this unknown component and its resemblance with various dark energy candidates proposed in the literature.

For the present model, the pair $\{r, s\}$ is obtained in terms of cosmic time t as

$$r(t) = \left(\frac{-6\beta + 8}{\beta^2} \right) \{\operatorname{sech}(2\alpha t)\}^2 + 1 \quad (23)$$

$$s(t) = \frac{4}{3} \frac{3\beta - 4}{3\beta^2 \{\cosh(2\alpha t)\}^2 - 4\beta} \quad (24)$$

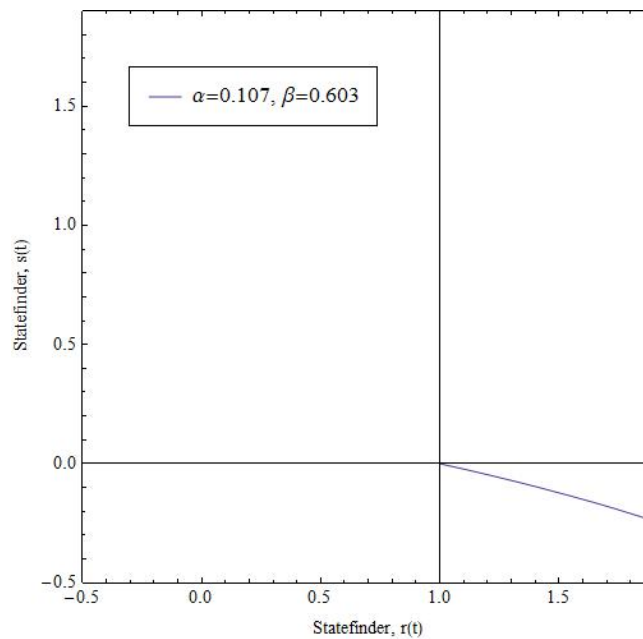


Figure 12. Plot of the statefinder pair $\{r, s\}$ vs cosmic time t for $\alpha = 0.107, \beta = 0.603$

Figure 12 shows the statefinder pair $\{r, s\}$ plot in the evolving universe. It shows that our model begins with Chaplygin gas behaviour $\{r > 1, s < 0\}$ and ends up with Λ CDM behaviour $\{r = 1, s = 0\}$.

7. ENERGY CONDITIONS:

The four energy conditions viz, the Strong Energy Condition (SEC), Weak Energy Condition (WEC), Dominant Energy Condition (DEC) and Null Energy Condition (NEC) are simply some constraints on some of the linear combinations of the energy density ρ and the pressure p . These four conditions are satisfied by all the normal matter in the universe, because of the positive energy density and the positive pressure of the normal matter. For that reason, violation of any of the energy conditions implies the presence of some non-normal matter in the universe [30]. The validity of SEC is the implication of decelerating universe, independent of whether the universe is open, flat, or closed. The validity of WEC is the implication of the ever positive and non-increasing nature of the energy density. The DEC provides an upper bound on the energy density and the rate of cosmic expansion. The validity of NEC is the implication of a weak upper bound on the Hubble parameter and inverse proportionality of the energy density and the size of the universe.

These energy conditions are given by:

$$\text{SEC} : \rho + 3p \geq 0, \rho + p \geq 0$$

$$\text{WEC} : \rho + p \geq 0, \rho \geq 0$$

$$\text{DEC} : \rho + p \geq 0, \rho - p \geq 0, \rho \geq 0$$

$$\text{NEC} : \rho + p \geq 0$$

For our model,

$$\begin{aligned}
 (\rho + 3p)(t) &= \frac{\phi_0 a_0^m}{8\pi} \{\sinh(2\alpha t)\}^{\frac{m\beta}{2}} [2\alpha^2 \beta (3m + 2m\omega) \{\operatorname{cosech}(2\alpha t)\}^2] \\
 &\quad + \frac{\phi_0 a_0^m}{8\pi} \{\sinh(2\alpha t)\}^{\frac{m\beta}{2}} [3\alpha^2 \beta^2 (2 - m - 2m\omega - m^2 - m^2\omega) \{\operatorname{coth}(2\alpha t)\}^2] \quad (25)
 \end{aligned}$$

$$\begin{aligned}
 (\rho + p)(t) &= \frac{\phi_0 a_0^m}{8\pi} \{\sinh(2\alpha t)\}^{\frac{m\beta}{2}} [2\alpha^2 \beta (2 + m) \{\operatorname{cosech}(2\alpha t)\}^2] \\
 &\quad + \frac{\phi_0 a_0^m}{8\pi} \{\sinh(2\alpha t)\}^{\frac{m\beta}{2}} [\alpha^2 \beta^2 (m - m^2 - m^2\omega) \{\operatorname{coth}(2\alpha t)\}^2] \quad (26)
 \end{aligned}$$

$$\begin{aligned}
 (\rho - p)(t) &= \frac{\phi_0 a_0^m}{8\pi} \{\sinh(2\alpha t)\}^{\frac{m\beta}{2}} [2\alpha^2 \beta (4 - m - 2m\omega) \{\operatorname{cosech}(2\alpha t)\}^2] \\
 &\quad + \frac{\phi_0 a_0^m}{8\pi} \{\sinh(2\alpha t)\}^{\frac{m\beta}{2}} [\alpha^2 \beta^2 (-6 + 5m + 6m\omega + m^2 + m^2\omega) \{\operatorname{coth}(2\alpha t)\}^2] \quad (27)
 \end{aligned}$$

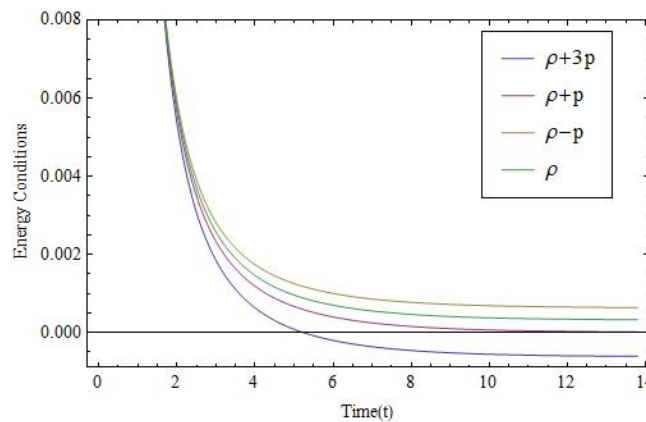


Figure 13. Evolution of the energy conditions vs cosmic time t for $\alpha = 0.107$, $\beta = 0.603$, $a_0 = \phi_0 = 1$, $m = 0.001$, $\omega = 1628$

Figure 13 illustrates the validity of the energy conditions. We observe that for $\alpha = 0.107$, $\beta = 0.603$, all of the four energy conditions are satisfied in the early universe. But in the long run ($t \sim 5.22$), SEC is violated. Violation of the SEC indicates the accelerating expansion of the universe.

8. CONCLUDING REMARKS

In this paper, we investigate a flat FLRW universe filled with a perfect fluid within the framework of Brans-Dicke theory of gravity with a time dependent cosmological constant. For the purpose of obtaining an exact solution of the field equations, so as to construct a cosmological model, the extra conditions taken into consideration are: (i) the scale factor a has a power law relation with the scalar field ϕ and (ii) the Hubble parameter H is a hyperbolic function of the cosmic time t . We examine the physical and kinematical properties of the constructed model by studying the evolution of some important parameters such as the scale factor a , scalar field ϕ , spatial volume parameter V , Hubble parameter H , expansion scalar θ , deceleration parameter q , cosmological constant Λ , pressure p , energy density ρ , EoS parameter η , jerk parameter j , snap parameter s , lerk parameter l , and by examining the statefinder pair $\{r, s\}$ and validity of the four energy conditions.

We observe that the universe corresponding to our model is expanding throughout its evolution and it exhibits the late time cosmic acceleration.

The Hubble parameter, the expansion scalar and the energy density decrease as the universe evolves but remain positive throughout the evolution of the universe.

The pressure is initially positive but attains negative values later in the evolving universe. The negative pressure indicates the presence of some exotic component in the universe which could be responsible for the late time cosmic acceleration and hence can be considered to be the so called dark energy.

The cosmological constant shows negative behaviour in the early universe which transits into positive one at a later phase of the cosmic evolution.

The EoS parameter attains the value -1 at late times, hinting that our model behaves like Λ CDM model in the late phases of the cosmic evolution.

Further, the jerk, snap and lerk parameters tend to 1 at late times which asserts the current observational data.

The statefinder pair $\{r, s\}$ identifies the constructed model's behaviour resembling the Λ CDM at late times.

Violation of the SEC indicates presence of some non-normal matter in the universe which could possibly be the reason for the accelerating expansion of the universe at late times.

ORCID

 **Anindita Basumatary**, <https://orcid.org/0009-0001-8747-0456>;  **Chandra Rekha Mahanta**, <https://orcid.org/0000-0002-8019-8824>

REFERENCES

- [1] S. Perlmutter, *et al.*, "Measurements of the cosmological parameters Ω and Λ from the first seven supernovae at $z \geq 0.35$," *The Astrophysical Journal*, **483**, 565-581 (1997). <https://doi.org/10.1086/304265>
- [2] S. Perlmutter, *et al.*, "Discovery of a supernova explosion at half the age of the Universe," *Nature*, **391**, 51-54 (1998). <https://doi.org/10.1038/34124>
- [3] A.G. Riess, *et al.*, "Observational evidence from supernovae for an accelerating universe and a cosmological constant," *The Astronomical Journal*, **116**, 1009-1038 (1998). <https://doi.org/10.1086/300499>
- [4] S. Perlmutter, *et al.*, "Measurements of Ω and Λ from 42 high- redshift supernovae," *The Astrophysical Journal*, **517**, 565-586 (1999). <https://doi.org/10.1086/307221>
- [5] A.D. Miller, *et al.*, "A Measurement of The Angular Power Spectrum of The Cosmic Microwave Background From $l = 100$ to 400," *The Astrophysical Journal*, **524**, L1-L4 (1999). October 10, <https://doi.org/10.1086/312293>
- [6] D.N. Spergel, *et al.*, "First- Year Wilkinson Microwave Anisotropy Probe (WMAP) Observations: Determination of Cosmological Parameters," *The Astrophysical Journal Supplement Series*, **148**, 175-194 (2003). <https://doi.org/10.1086/377226>
- [7] C.L. Bennett, *et al.*, "First-Year Wilkinson Microwave Anisotropy Probe (WMAP) Observations: Preliminary Maps and Basic Results," *The Astrophysical Journal Supplement Series*, **148**, 1-27 (2003). <https://doi.org/10.1086/377253>
- [8] K. Abazajian, *et al.*, "The Second Data Release of The Sloan Digital Sky Survey," *The Astronomical Journal*, **128**, 502-512 (2004). <https://doi.org/10.1086/421365>
- [9] M. Tegmark, *et al.*, "The Three-Dimensional Power Spectrum of Galaxies from The Sloan Digital Sky Survey," *The Astrophysical Journal*, **606**, 702-740 (2004). <https://doi.org/10.1086/382125>
- [10] D.N. Spergel, *et al.*, "Three-Year Wilkinson Microwave Anisotropy Probe (WMAP) Observations: Implications for Cosmology," *The Astrophysical Journal Supplement Series*, **170**, 377-408 (2007). <https://doi.org/10.1086/513700>
- [11] C. Brans and R.H. Dicke, "Mach's Principle and a Relativistic Theory of Gravitation," *Physical Review*, **124**(3), (1961). <https://doi.org/10.1103/PhysRev.124.925>
- [12] B. Bertotti, L. Iess, and P. Tortora, "A test of general relativity using radio links with the Cassini spacecraft," *Nature*, **425**, 374-376 (2003). <https://doi.org/10.1038/nature01997>
- [13] F.Q. Wu, and X. Chen, "Cosmic microwave background with Brans-Dicke gravity. II. Constraints with the WMAP and SDSS data," *Physical Review D*, **82**, 083003 (2010). <https://doi.org/10.1103/PhysRevD.82.083003>
- [14] Y.C. Li, F.Q. Wu, and X. Chen, "Constraints on the Brans-Dicke gravity theory with the Planck data," *Physical Review D*, **88**, 084053 (2013). <https://doi.org/10.1103/PhysRevD.88.084053>
- [15] S. Song, *et al.*, "Alternative dynamics in loop quantum Brans-Dicke cosmology," *Physical Review D*, **102**, 024024 (2020). <https://doi.org/10.1103/PhysRevD.102.024024>
- [16] S.K. Tripathy, "Bouncing scenario in Brans-Dicke theory," *International Journal of Geometric Methods in Modern Physics*, **17**, 2050056 (2020). <https://doi.org/10.1142/S0219887820500565>
- [17] M. Sharif, and A. Majid, "Extended gravitational decoupled solutions in self-interacting Brans-Dicke theory," *Physics of the Dark Universe*, **30**, 100610 (2020). <https://doi.org/10.1016/j.dark.2020.100610>
- [18] S.P. Hatkar, C.D. Wadale, and S.D. Katore, "Viscous holographic dark energy in Brans-Dicke theory of gravitation," *Astrophysics and Space Science*, **365**, 7 (2020). <https://doi.org/10.1007/s10509-020-3723-9>
- [19] A.K. Yadav, "Note on Tsallis holographic dark energy in Brans-Dicke cosmology," *The European Physical Journal C*, **81**, 8 (2021). <https://doi.org/10.1140/epjc/s10052-020-08812-z>
- [20] A.K. Yadav, *et al.*, "Transitioning universe with hybrid scalar field in Bianchi I space-time," *Physics of the Dark Universe*, **31**, 100738 (2021). <https://doi.org/10.1016/j.dark.2020.100738>
- [21] R.K. Mishra, and H. Dua, "Evolution of FLRW universe in Brans-Dicke gravity theory," *Astrophysics and Space Sci*, **366**, 6 (2021). <https://doi.org/10.1007/s10509-020-03908-0>
- [22] M.V. Santhi, T. Chinnappalanaidu, S.S. Madhu, and D.M. Gusu, "Some Bianchi Type Viscous Holographic Dark Energy Cosmological Models in the Brans-Dicke Theory," *Hindawi, Advances in Astronomy*, **2022**, 5364541 (2022). <https://doi.org/10.1155/2022/5364541>
- [23] A. Chand, R.K. Mishra, and A. Pradhan, "FRW cosmological models in Brans-Dicke theory of gravity with variable q and dynamical Λ -term," *Astrophysics and Space Science*, **361**, 81 (2016). <https://doi.org/10.1007/s10509-015-2579-x>

- [24] F.M. Esmaceli, "Anisotropic Behavior of Cosmological Models with Exponential and Hyperbolic Scale Factors," Journal of High Energy Physics, Gravitation and Cosmology, **04**(02), 83154 (2018). <https://doi.org/10.4236/jhepgc.2018.42017>
- [25] F.M. Esmaceli, and B. Mishra, "Behaviour of physical parameters in extended gravity with hyperbolic function," Journal of Astrophysics and Astronomy, **39**, 59 (2018). <https://doi.org/10.1007/s12036-018-9553-2>
- [26] B. Mishra, S.K. Tripathy, and S. Ray, "Cosmological models with squared trace in modified gravity," International Journal of Modern Physics D, **29**(15), 2050100 (2020). <https://doi.org/10.1142/S021827182050100X>
- [27] B. Mishra, F.M. Esmaceli, and S. Ray, "Cosmological models with variable anisotropic parameter in $f(R, T)$ gravity," Indian Journal of Physics, **95**, 2245–2254 (2021). <https://doi.org/10.1007/s12648-020-01877-2>
- [28] M. Visser, "Jerk, snap and cosmological equation of state," Classical and Quantum Gravity, **21**, 2603-2615 (2004). <https://doi.org/10.1088/0264-9381/21/11/006>
- [29] V. Sahni, T.D. Saini, A.A. Starobinsky, and U. Alam, "Statefinder- A New Geometrical Diagnostic of Dark Energy," JETP Letters, **775**, 201-206 (2003). <https://doi.org/10.1134/1.1574831>
- [30] M. Visser, "General Relativistic Energy Conditions: The Hubble expansion in the epoch of galaxy formation," Physical Review D, **56**(12), 7578 (1997). <https://doi.org/10.1103/PhysRevD.56.7578>

**ПЛОСКА КОСМОЛОГІЧНА МОДЕЛЬ ФРІДМАНА-ЛЕМЕТРА-РОБЕРТСОНА-УОКЕРА
ІЗ ЗАЛЕЖНОЮ ВІД ЧАСУ КОСМОЛОГІЧНОЮ КОНСТАНТОЮ
В ТЕОРІЇ ГРАВІТАЦІЇ БРАНСА-ДІККЕ**

Аніндіта Басуматарі, Чандра Рекха Маханта

Факультет математики, Університет Гаухаті, Гувахаті -781014, Індія

Останнім часом виник великий інтерес до дослідження видатних проблем космології за допомогою модифікованих теорій гравітації. Теорія гравітації Бранса-Дікке є однією з таких теорій, розроблених Брансом і Дікке, які ввібрали принцип Маха в Загальну теорію відносності. У теорії Бранса-Дікке гравітація пов'язана з залежним від часу скалярним полем ϕ через параметр зв'язку ω . Ця теорія зводиться до загальної теорії відносності, якщо скалярне поле ϕ є постійним, а параметр зв'язку $\omega \rightarrow \infty$. У цій статті ми розглядаємо плоский Всесвіт Фрідмана-Леметра-Робертсона-Уокера (FLRW) із залежною від часу космологічною константою в теорії гравітації Бранса-Дікке. Точні розв'язки рівнянь поля отримані за допомогою степеневого співвідношення між масштабним фактором і скалярним полем Бранса-Дікке ϕ і за допомогою параметра Хаббла H як гіперболічної функції космічного часу t . Ми вивчаємо космологічну динаміку нашої моделі шляхом графічного представлення деяких важливих космологічних параметрів, таких як параметр уповільнення, параметр щільності енергії, параметр рівняння стану, параметр ривка, параметр миттєвого примикання, параметр jerk тощо. Також отримано діагностичну пару моделі вимірювача стану і справедливості чотирьох енергетичних умов, а саме. Досліджується сильний енергетичний стан (SEC), слабкий енергетичний стан (WEC), домінуючий енергетичний стан (DEC) і нульовий енергетичний стан (NEC). Ми виявили, що Всесвіт, який відповідає нашій моделі, розширюється протягом своєї еволюції та демонструє пізні космічне прискорення, що узгоджується з поточними даними спостережень.

Ключові слова: теорія Бранса-Дікке; Всесвіт Фрідмана-Леметра-Робертсона-Уокера; космологічна стала; параметр Хаббла; параметр уповільнення